Earth's magnetic field over the last 1000 years

Robin Senftleben

Declaration of authorship

I declare that I completed this thesis on my own and that information which has been directly or indirectly taken from other sources has been noted as such. Neither this nor a similar work has been presented to an examination committee.

Potsdam, July 2020   . . . .

UNIVERSITÄT POTSDAM

Abstract

Mathematisch-Naturwissenschaftlichen Fakultät

Institut für Erd- und Umweltwissenschaften

Earth's magnetic field over the last 1000 years

by Robin SENFTLEBEN

To investigate the reliability and stability of spherical harmonic models based on archeo/-paleomagnetic data, 2000 Geomagnetic models were calculated. All models are based on the same data set but with randomized uncertainties. Comparison of these models to the geomagnetic field model gufm1 showed that large scale magnetic field structures up to spherical harmonic degree 4 are stable throughout all models. Through a ranking of all models by comparing the dipole coefficients to gufm1 more realistic uncertainty estimates were derived than the authors of the data provide.

The derived uncertainty estimates were used in further modelling, which combines archeo/-paleomagnetic and historical data. The huge difference in data count, accuracy and coverage of these two very different data sources made it necessary to introduce a time dependent spatial damping, which was constructed to constrain the spatial complexity of the model. Finally 501 models were calculated by considering that each data point is a Gaussian random variable, whose mean is the original value and whose standard deviation is its uncertainty. The final model arhimag1k is calculated by taking the mean of the 501 sets of Gauss coefficients. arhimag1k fits different dependent and independent data sets well. It shows an early reverse flux patch at the core-mantle boundary between 1000 AD and 1200 AD at the location of the South Atlantic Anomaly today. Another interesting feature is a high latitude flux patch over Greenland between 1200 and 1400 AD. The dipole moment shows a constant behaviour between 1600 and 1840 AD.

In the second part of the thesis 4 new paleointensities from 4 different flows of the island Fogo, which is part of Cape Verde, are presented. The data is fitted well by arhimag1k with the exception of the value at 1663 of $28.3 \pm 2.3 \mu T$, which is approximately $10 \mu T$ lower than the model suggest.

Das Erdmagnetfeld der letzten 1000 Jahre

Um die Stabilität und Zuverlässigkeit von sphärisch harmonischen Erdmagnetfeldmodellen, die auf paleomagnetischen und archeomagnetischen Daten basieren zu untersuchen wurden 2000 Erdmagnetfeldmodelle berechnet. Jedes dieser Modelle berechnet sich aus Daten, die mit zufälligen Unsicherheiten in die Inversion eingehen. Ein Vergleich dieser Modelle zum historischen Erdmagnetfeldmodell gufm1 zeigt, dass großflächige magnetische Strukturen bis zum sphärischen harmonischen Grad 4 stabil in allen Modellen sind. Ein Ranking der 2000 Modelle wurde verwendet, um realistischere Fehlerabschätzungen der Daten zu bekommen, als die, die von den Autoren angebeben werden.

Diese Fehlerabschätzungen werden für die weitere Modellierung benutzt, welche historische und paleo-/archeomagnetiche Daten kombiniert. Der große Unterschied in der Anzahl der Daten und der räumlichen Verteilung dieser sehr verschiedenen Datenquellen machte es notwendig, eine zeitabhängige räumliche Dämpfung einzuführen. Diese ist so konstruiert, dass die räumlich Komplexität des Modelles in einem bestimmten Zeitintervall festgelegt wird. 501 Modelle wurde berechnet, indem jeder Datenpunkt als gaußsche Zufallsvariable gesehen wird mit dem Originalwert als Mittelwert und die Fehlerabschätzung als Standardabweichung. Das finale Modell arhimag1k berechnet sich aus dem Mittelwert der Gaußkoeffizienten aller 501 Modelle. arhimag1k fittet verschiedene abhängige und unabhängige Datensätze gut. Es zeigt eine frühe Anomaly an der Kern-Mantel Grenze zwischen 1000 und 1200 AD an der Lokation, wo auch die heutige Südatlantische Anomaly liegt. Eine andere interessante Auffälligkeit ist eine starke radiale Magnetfeldkomponente an der Kern-Mantel Grenze zwischen 1200 und 1400 AD über Grönland. Das Dipolmoment zeigt ein konstantes Verhalten von 1600 bis 1840 AD.

Im zweiten Teil der Arbeit werden 4 neue Paleointensitäten der Insel Fogo, welches Teil von Kap Verde ist, presentiert. Diese neuen Daten werden gut von dem Modell arhimag1k gefittet, außer der Wert von 1663 AD mit $28.3 \pm 2.3 \mu T$, welcher etwa $10 \mu T$ niedriger ist, als das Modell zeigt.

Acknowledgements

It was long road, which never seemed to end. A lot of time went by and I often felt like giving up. I'm proud of myself for pulling through and have to thank so many people for giving me motivation to keep going. Without these people this work would have never been printed in a "finalized state".

I want to thank the brilliant and nice scientists in section 2.3/2.8 from the GeoForschungsZentrum Potsdam. I normally tend to solve all my problems alone and avoided communicating with other people. But being in this amazing community of funny, inspiring, creative and bighearted people made me enjoy and appreciate to communicate and interact with others. This is far more worth to me than any finished dissertation in this world.

Firstly I want to thank my supervisor Monika, who always was there and made time for me to discuss ideas or results from my work. She made it very easy for me to continue my work even when my contract with the GFZ was already finished. Further I want to thank Foteini, who shared an office with me for 3 years. On average we probably spend 10 hours in the office every work day and had many funny, interesting and also awkward conversations with each other. She always made time to help me and correct my horrible English writing. I want to thank Tarique who started his PhD at around the same time as me but finished much earlier because he is brilliant and a really hard worker, who also inspired me to try harder than I usually do. I am thanking Leonie, who has been my fellow sufferer doing the PhD. I have never met a person, who has a bigger inner motivation to do the best and be the best possible. She is a big inspiration and a good friend for me.

The life of a scientist seems very similar to a life of a nomad. After one contract finishes and a good opportunity arises at another institute or university the scientist moves far away. They are people that helped me being a better version of myself and have taken a place in my heart, Reyko, Ingo, Maxwell, Seiki, Jaeheung and Boris to name just a few.

Contents

List of Figures

List of Tables

Chapter 1

Understanding Earth's magnetic field

Earth's magnetic field is very important for our daily human life. It is shielding us against radiation from the sun and other external sources. This radiation is especially harmful to satellites, power grid lines, communication or navigation systems. In areas where the magnetic field is weak one can, for example, observe increased failures of satellite instruments. In times of a magnetic storm, which can result from ejected solar material towards Earth, big fluctuations in the power grid lines or even total power outages can occur.

Another reason to look into the magnetic field is that it is one of the few signals originating in the deep interior of the Earth that can be measured at the Earth surface. It is generated in the fluid outer core, which consists mainly of iron and nickel. Therefore, looking at the changes of the magnetic field at the Earth's surface helps to constrain the fluid flow inside the outer core. Governing the fluid motion helps to better understand the physical processes inside the outer core.

The awareness that Earth possesses a magnetic field and that this can be used for navigation by the means of magnetic compasses dates back to the first century. However it was not until the early 17th century that it was accepted Earth's magnetic field is actually varying with time. This was first found in 1635 AD by Henry Gellibrand who published his work "A Discourse Mathematical on the Variation of the Magneticall Needle" (Gustav Hellmann [2017],Gellibrand [1635]). It resulted from comparisons of declination measurements in London at different times,

which showed that the angle between geographic north and magnetic north had changed around 7 degrees in 54 years.

These changes in the magnetic field are only well known for the last 200 years and it has to be further explored how exactly the magnetic field changed before that.

1.1 Short introduction to some basics

1.1.1 Different contributions to Earth's magnetic field

Earth's magnetic field can be separated into different parts, which are either of internal or external origin. There is the main or core field which is generated in the liquid outer core. It is called the main field because it is the biggest contribution of the magnetic field with more than 95% of the total field strength at ground level, which is between 30000 and 60000 nT. The liquid outer core is separated from the mantle by the core-mantle boundary (CMB) which is located at a depth of 2900km. The second biggest contribution at the Earth surface is the crustal field contributing a few hundred nanoteslas on average. The main and the crustal field are considered as the internal field. The external field originates in the ionosphere and magnetosphere and is generated by electrical currents and contributes generally a few percent. Smaller contributions originate from induced electric currents in the Earth's crust and mantle due to time varying external fields. Another small contribution is generated through the movement of electrically conducting sea water, which is few nanoteslas at Earth's surface.

1.1.2 Coordinate system of Earth's magnetic field

Earth's magnetic field elements of a field vector $\vec{B}$ are the X or North component, the Y or East component and the Z or Nadir component(figure 1.1). These main component can be used to derive additional magnetic elements. The angle between geographic north and the direction in the horizontal plane is defined as declination $D = \arctan{(Y/X)}$, the angle between horizontal plane and the field vector defined as inclination $I = \arctan{(Z/H)}$, the horizontal component $H = \sqrt{X^2 + Z^2}$ and the total intensity $F = \sqrt{X^2 + Z^2 + Z^2}$.
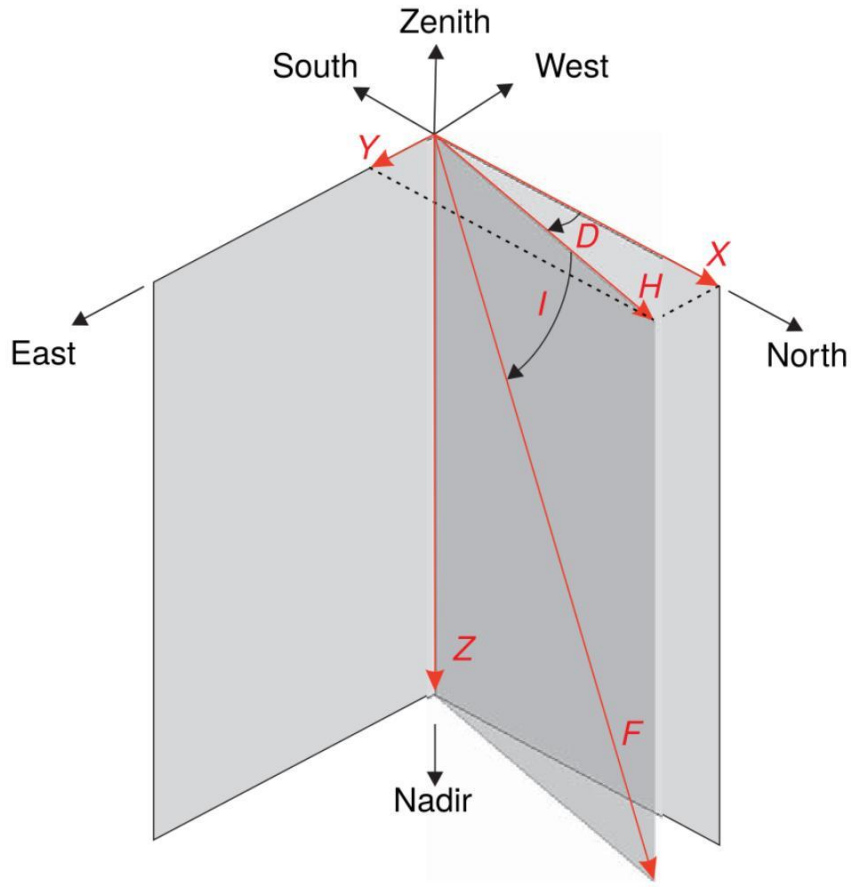
FIGURE 1.1: Magnetic field components (figure from [Schubert, 2007])

1.1.3 Spherical harmonic representation of Earth's magnetic field

It can be shown that the magnetic field can be expressed as the gradient of a scalar potential, which satisfies the Laplace equation.

$$\vec{B} = -gradV \tag{1.1}$$

$$\nabla^2 V = \Delta V = 0 \tag{1.2}$$

With Earth's spherical geometry that geomagnetic potential V can be written as

$$V(r, \theta, \phi, t) = a \sum_{l=1}^{L} \sum_{m=0}^{l} \left(\frac{a}{r}\right)^{l+1} \left[g_l^m(t)\cos(m\phi) + h_l^m(t)\sin(m\phi)\right] P_l^m(\cos(\theta)) \tag{1.3}$$

where $g_l^m(t)$ and $h_l^m(t)$ are expansion coefficients known as the Gaussian coefficients, P_l^m are the Schmidt quasi-normalized associated Legendre functions and a is the average radius of the Earth. This expression is the basis of spherical harmonic analysis (SHA) for the geomagnetic field.

The SHA is used in magnetic field modelling for example the gufm1 model, the Arch3k.1 model or the CALS models, which are described in detail in chapter 3. The time dependent Gaussian coefficients allow to estimate the change of the magnetic field with time, which is also be called secular variation throughout this work.

1.1.4 Downward continuation

Knowing the coefficients $g_l^m(t)$ and $h_l^m(t)$ makes is possible to calculate the magnetic field at any radius r down to the core-mantle boundary (CMB), which is called downward continuation. The magnetic field at the CMB allows for estimation of the fluid flow in the outer core, which is the source of the main magnetic field.

The main indicator is the radial component of the magnetic field at the CMB, which is the component pointing in the opposite direction as Z, i.e. away from the center of Earth. Locations at the CMB where a strong radial magnetic field is detected are associated with circular fluid flows at these locations and are called flux patches. Here we have to distinguish between normal and reverse flux patches. Normal flux patches create a magnetic field which is pointing in the direction of the current magnetic main field direction. Reverse flux patches create an opposite magnetic field and weaken the current magnetic field at their locations.

1.1.5 Dipole moment of Earths magnetic field

The present Earth magnetic field can in first order be approximated by magnetic dipole situated at the center of the Earth and is aligned with the rotation axis. In the current configuration of Earth magnetic field this dipole points from geographic north to south. The angle between the dipole axis and the rotation axis of Earth is called the tilt angle.

The absolute value of the dipole moment $\vec{D_m}$ can be calculated in terms of the degree l=1 Gaussian coefficients.
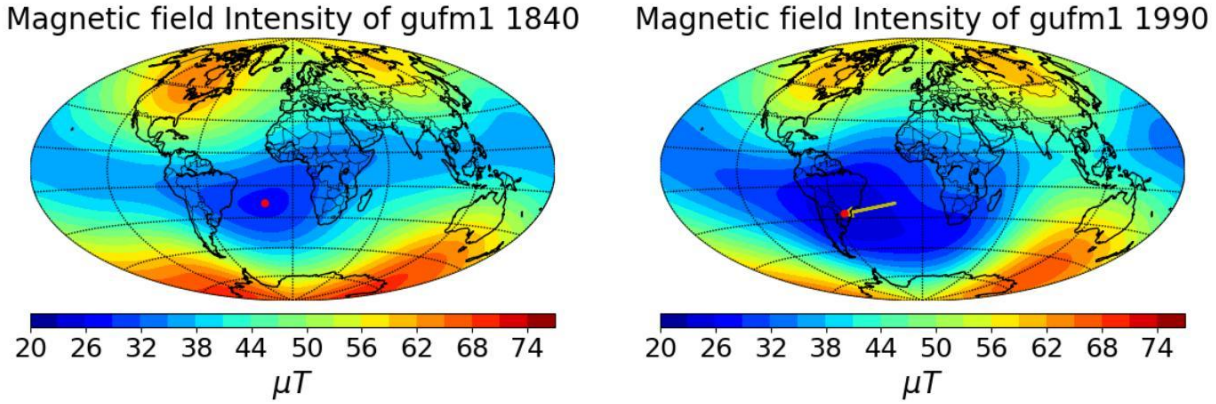
FIGURE 1.2: Intensity of magnetic field model gufm1 at the Earth surface in 1840 AD (left) and in 1990 AD (right). The red dot denotes the lowest intensity and the yellow arrow marks the movement of this point over 150 years.

$$|\vec{D_m}(t)| = \frac{4\pi a^3}{\mu_0}\sqrt{(g_1^0(t))^2 + (g_1^1(t))^2 + (h_1^1(t))^2} \tag{1.4}$$

Here μ_0 is the magnetic constant. The Gaussian coefficient g_1^0 is also called the axial dipole coefficient and describes the dipole strength along the rotation axis of Earth. If g_1^1 and h_1^1 are zero the dipole would be fully aligned with the rotation axis leading to a tilt angle of zero degrees.

1.2 Current knowledge of the characteristics and global changes of Earth's magnetic field

The current magnetic field is especially weak over an area in the South Atlantic Ocean known as the South Atlantic Anomaly (SAA). This magnetic anomaly is located between South Africa and South America and the magnetic field strength lies between 20 μT and 30 μT at Earth's surface while at other comparable latitudes it lies between 40 μT and 50 μT. It is known that this magnetic field feature drifted south-westwards and intensified over the past 100 years (Figure 1.2). The magnetic field model gufm1 [Jackson et al., 2000] shows that this weak field at Earth's surface is related to reverse flux at the core mantle boundary. Reverse flux creates a magnetic field component in the opposite direction than the normal dipole field.

The dipole moment of the Earth has weakened by 9 percent over the last 150 years. Different studies have tried to find explanations for this decay. It was shown that the observed decay of the dipole can't be explained by ohmic-free decay (decay due to electrical resistance alone)

because the rate of decay is 11 to 16 times higher than it would be theoretically expected if ohmic-free decay would be responsible for the dipole moment decay [Olson and Amit, 2006]. Hulot et al. [2002] showed that almost all the decrease in the dipole from 1980 to 2000 can be attributed to growth and pole-wards movement of the previously mentioned reverse flux patches. Their study was based on data of the Magsat satellite, which operated in 1979/80, and of the satellite Oersted, which is operating since 1999. Hulot et al. [2002] also showed that the axial dipole moment decay is mostly a phenomenon of the southern hemisphere, which was supported by further studies [Olson and Amit, 2006].

Especially over the Atlantic and close to the equator the field has moved west-wards over the last 100 years. On the contrary the Pacific ocean shows almost no or no clear secular variation and the magnetic field there is relatively constant which can be seen in gufm1 by Jackson et al. [2000]. The models of Constable et al. [2000] see considerable secular variation in the Pacific hemisphere over the last 3000 years. This suggests that the low secular variation during the historical times could be a short time feature. But on contrary the models in Constable et al. [2016] show that the Atlantic hemisphere has sustained consistently more active secular variation than the Pacific hemisphere. As a possible reason they mention large heterogeneities at the core-mantle boundary.

The model gufm1 of Jackson et al. [2000] show 4 static flux patches in the radial component of Earth's magnetic field (figure 1.3). These persist at least over the last 100 years between 60 and 70 degrees latitude in the northern and southern hemisphere. The models of Constable et al. [2000] show that North American and Siberian flux patches can't be considered as permanent feature but they see almost always a dominant flux patch in the northern hemisphere.

The north geomagnetic pole has moved 30 degrees westwards from 1650 AD to 1860 AD and the tilt angle increased from 7.5 degree to 11.4 degree(Olson and Amit [2006], A. C. Fraser-Smith [1987]; Bloxham and Jackson [1992]; Jackson et al. [2000]). From 1860 AD to 1960 AD the tilt remained almost constant while the westward motion of the north geomagnetic pole continued. Between 1970 AD to 2000 AD the pole position has changed by over 1 degree.
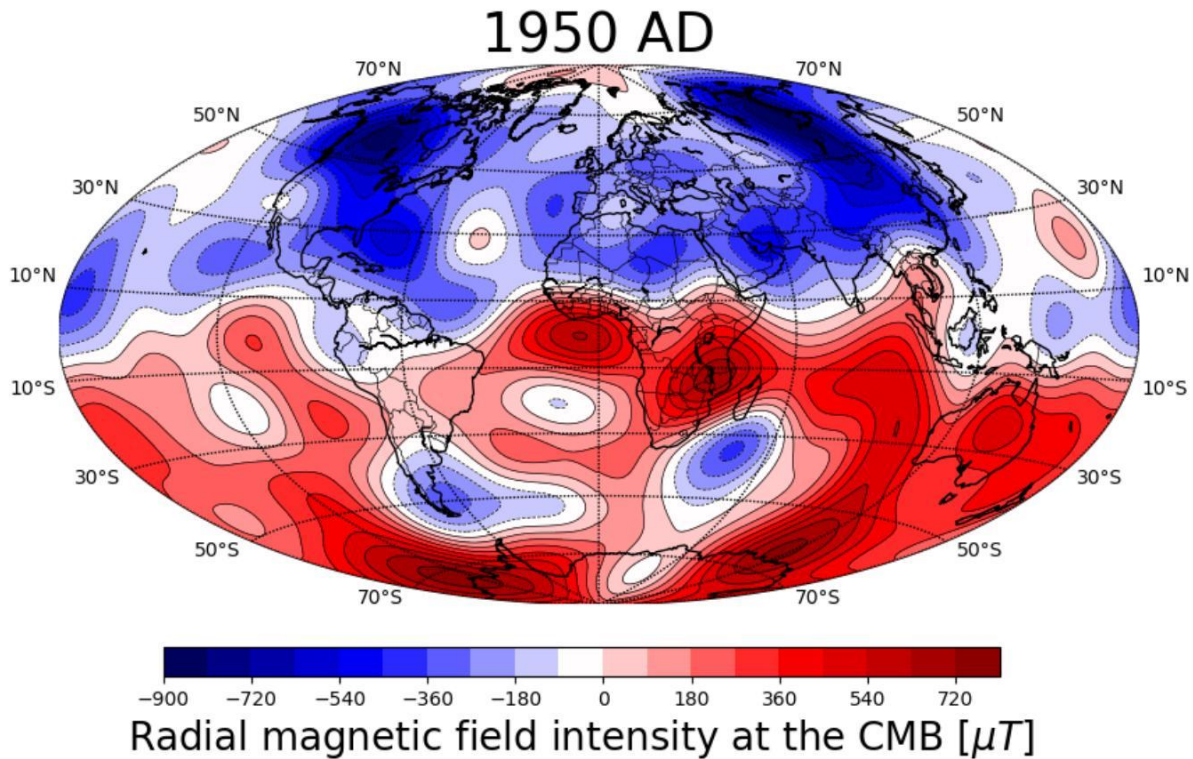
FIGURE 1.3: Radial magnetic field component at the core-mantle boundary of model gufm1 at 1950 AD.

1.3 Open questions related to Earth's magnetic field

1.3.1 Estimation of the axial dipole coefficient g_1^0 prior to 1840 AD

Prior to 1840 AD it was not known how to precisely determine the absolute magnetic intensity. Due to this lack of direct intensity measurements the accuracy of the ancient magnetic dipole moment which is estimated by magnetic field models is rather uncertain. Figure 1.4 shows different results for the axial dipole coefficient which is the main contribution to the dipole moment.

The following studies give an estimation of this quantity:

- The model gufm1 from Jackson et al. 2000 describes the magnetic field over 400 years from 1590 to 1990. It is based on many measurements of declination and inclination which stem mostly from ship logbooks. From 1590 to 1840 there is mainly directional data. From 1840 onwards there are also intensity measurements which allow to constrain the dipole moment of the field. The axial dipole coefficient hence was extrapolated before 1840 due to missing intensity values.
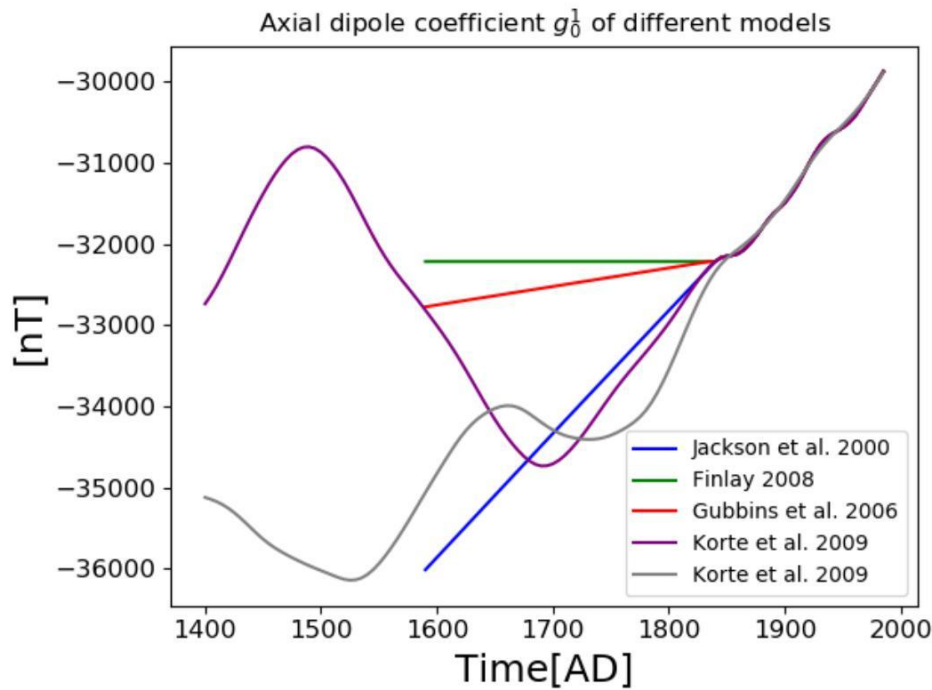
FIGURE 1.4: Axial dipole coefficient of different models. The coefficient is negative and the visual increase translates to an actual decrease of the absolute strength.

- Other models are the CALS series of models for a period of 3000, 7000 and 10000 years (Korte and Constable [2003], Korte and Constable [2005], Korte et al. [2011], Korte and Constable [2011]).They build on a big compiled archeomagnetic and paleomagnetic database and give an estimation of the ancient dipole moment. These models make use of the good knowledge of the magnetic field over the last 400 years and additionally constrain the dipole coefficients by penalizing departure of the model coefficients from the model gufm1.

- Gubbins [2006] used archeointensities and compared them with intensity values which result from the gufm1 model. These ratios of intensity were then used to generate a new axial dipole coefficient. This study resulted in a less decreasing g_0^1 coefficient of 2.28 ± 1 nT before 1840 than gufm1 extrapolated.

- Finlay [2008] used a database which consisted primarily of historical data that was used to construct gufm1 and a subset of an archaeomagnetic intensity database compiled by Korte and Constable [2005]. A range of possible linear models are explored and a value of $\frac{\partial g_0^1}{\partial t} = 2.74 \pm 42.32 \ nT/year$ is found to explain the archeointensity dataset with maximum likelihood. Comparisons to Bayesian model techniques lead to a model with a flat evolution of the axial dipole component as most probable.

- Suttie et al. [2011] used 223 achaeo -and paleointensities to convert them into the corresponding axial dipole coefficients by using the method of Gubbins [2006]. They found that the dipole decay before 1840 is consistent with the rate found in gufm1 since 1840 with around 11.9 nT/y.

- Poletti et al. [2018] used data from GEOMAGIA50.v3 ([Donadini et al., 2006],[Brown et al., 2015]) and other recently published data to convert these to axial dipole moments with the method of Gubbins [2006]. They filtered their data based on criteria concerning age uncertainty, method, additional steps to check for alteration, influence of multi-domain grains anisotropy thermoremanent magnetisation correction, cooling rate correction, standard deviation of the final archaeointensity estimate. 413 data out of 2532 fulfilled these criteria. This study suggest that the linear decay started already between 550 and 750 CE and continued until today.

In this work the dipole moment is determined for the last 1000 years by combining direct and indirect measurements of the magnetic field in a magnetic field model. The archeomagnetic and paleomagnetic data complements the historical database mostly consisting of directional records from 1590 to 1840 and constrains the field before 1590. This is the first time directional and intensity data of historical and archeo-/paleomagnetic sources are combined in one global model.

1.3.2 Uncertainty of archeomagnetic -and paleomagnetic data

The uncertainty of the dipole moment in the previous point is strongly dependent on the uncertainty of the data that is used to constrain the magnetic field model. In the case of the dipole moment prior to 1840 AD this data is mostly archeomagnetic and paleomagnetic data and it is still debated how accurate they are and under which conditions these results can be used to accurately represent the ancient magnetic field. In this work one focus is to estimate the robustness of the output models, that is to estimate their stability against changes in data input. Another focus is to find more realistic weightings for different groups of data as compared to those that are provided with the data.

Comparison of indirect records to the gufm1 model in Suttie et al. [2011] suggest that volcanic data have a greater spread than archaeological data but fewer outliers. In general it is difficult to attribute any real improvement to any data set due to corrections or factors considered. They also mention that the different data subsets are not completely independent because for example

some type of corrections are only done on specific materials. The most outstanding distribution with a mean that is different from the others is the data, which was corrected for cooling rate. This subset is the only one that isn't consistent with a zero mean distribution.

Panovska et al. [2015] look at different variances of spherical harmonic modelling techniques and find that one of the most influencing factors is the weighting of the data compared to certain changes in the actual modelling process.

1.3.3 The evolution of the South Atlantic Anomaly

One of the most outstanding structural features of Earth's magnetic field is the before mentioned SAA. This interesting field structure raises the question of its origin. Where and when did it start to develop and what might be the physical processes behind its creation.

The model in this work can give hints on how to answer these questions by tracking the main sources of the SAA, which is reverse flux at the core-mantle boundary in the South Atlantic region. With additional calculations this model can be used to make estimations about the surface flow of the liquid in Earth's outer core [Bloxham and Jackson, 1991], which also helps to better understand the physical processes that lead to a magnetic field structure such as the SAA. Another method to get information about the physical processes behind the geomagnetic secular variation is data assimilation which combines magnetic observations or in this case a magnetic field model and a model of the core dynamics [Kuang et al., 2008]. This not only allows for a better insight in the physics but also can be used to forecast magnetic secular variation.

Hartmann and Pacca [2009] looked at the time evolution of the South Atlantic Anomaly. With the help of the geomagnetic field models gufm1 and IGRF they determined the location of the South Atlantic Anomaly by choosing a grid of intensities calculated from the field models in the area of interest and finding the lowest values and then choosing a grid with a lower grid spacing and again finding the lowest value. This method was earlier proposed by Heynderickx [1996]. They find that the drift of the SAA for the past 415 years can be mainly divided in three parts. From 1590 to 1750 where the location of the SAA changed 6 degrees in longitude and 1.5 degrees in latitude, from 1750 to 1945-1950, where south- and westward drift were approximately constant and from 1945 to 2005, where only minor latitudinal movement and mainly westward drift occurred. In total, the intensity of the SAA decreased by $8500nT$ with an average decrease

rate of $22nT/year$ and also the area of influence is increasing. They also look at the ratio of non-dipolar field to dipolar field which shows an increase of the non-dipolar field by 5 percent.

Another way to track the SAA is used by Badhwar [1997], where the dose rate (amount of radioactive dose received by a person within a certain period of time) was measured on two manned space-crafts. One was Skylab and one was the Mir orbital station. The dose rates were measured in 1973 and 1995 and averaged over time and over latitude and longitude. This information was used to infer drift rates of the SAA. The result in this study was a westward drift of 0.28 ± 0.03 degrees per year and a northwards drift of 0.08 ± 0.03 degrees per year, which is in good agreement with geomagnetic field models for this time period.

The SAA also could possibly be connected to other significant changes in the last centuries like the global sea water level, as suggested by Santis et al. [2012]. In this study, the area of the SAA over time was determined from the magnetic field models gufm1 till 1940 and IGRF until 2005 using the isoline of $32000nT$ as the border. The area increased approximately from $0.5 \cdot 10^7 km^2$ to $7.5 \cdot 10^7 km^2$ in the last 400 years. This study shows that the increase in the SAA area correlates very well with the global sea level rise. Possible two mechanisms for this correlation are mentioned. An external mechanism would be that the increase of the SAA area facilitates the inflow of charged particles, which leads to warming of the atmosphere and finally to melting of the poles. They also propose as an internal reason a convective force in the outer core, which could cause the variation of the magnetic field and and at the same time create an elastic deformation at the Earth's surface which would cause a sea level rise.

1.3.4   Reversal of Earth's magnetic field

The most intriguing question about the Earth's magnetic field is whether the current configuration of decreasing magnetic dipole moment will lead to a reversal of the magnetic poles in the near future.

One way to study the possible causes of geomagnetic reversals is to make numerical dynamo simulations by using the full three-dimensional magnetohydrodynamics (MHD) equations like Glatzmaiers and Roberts [1995]. In their study, the model maintains a magnetic field for over 40000 years and after undergoing several polarity excursions it shows a successful reversal of the dipole near the end of the simulation.

The last geomagnetic field reversal happened 780000 years ago and it is known the Matuyama-Bruhnes polarity reversal. The question how often a reversal is happening on average in a certain time period and if the Earth is overdue for a new reversal to happen are open questions. Studies have shown that the reversal frequency is highly variant throughout time and tried to find possible explanations. Biggin et al. [2012] looked at the sensitivity of geomagnetic reversal frequency to changes in the core-mantle boundary (CMB) heat flow. They suggest that these changes could originate from sinking lithospheric slaps, which are parts of dense and cold material relatively to the rest of the mantle, or mantle plumes which are up-welling in the mantle. Another link mentioned in this study of Biggin et al. [2012] is the true polar wander which is a reorientation of the entire Earth's mantle and crust relative to the spin axis. All these processes lead to a change in the heat flow at the CMB and are linked to one another.

Olson and Amit [2015] studied the connection between mantle superplumes and geomagnetic superchrons, which are long time periods of at least 10 Myr in which the polarity of the Earth's magnetic field did not change. The last superchron was the Cretaceous Superchron which lasted from 120 to 80 million years ago. They use numerical dynamo simulations which are driven by the dual superplume outer boundary heat flux condition and study how the reversal frequency changes with the average core heat flux. They find that the reversal frequency increases approximately linearly with the global average heat flux on the outer boundary. They also determined the parameter ranges of the height of the superplumes and the average core heat flux for non reversing states i.e. superchrons. For example they found that only a change of 10 percent from the superplume height of today's values could lead to a superchron. Another part of this study was to explain the discrepancy that during the Cretaceous Superchron the mantle global circulation models indicate an increase in average CMB heat flow. By looking at geomagnetic reversal frequency records superimposed with formation ages and estimated volumes of large igneous provinces (LIPs) they found an inverse relationship of these two quantities. The explanation for this would be a time lag between a pulse of thermal plumes initiated near the CMB and their arrival at the base of the lithosphere. In this scenario the geodynamo and with this the reversal frequency would be affected immediately but the activity of the LIPs would increase tens of millions of years after the initial event.

Tarduno et al. [2015] looked at an interesting scenario for reversals based on directional and intensity archeomagnetic data from southern Africa, which showed strong changes in the geomagnetic field around 1300 AD. The directions changed 0.11 - 0.12 degrees per year from 1225 to 1550 and at same time the intensity dropped rapidly at an estimated rate of -0.054 $\pm$ 0.036 μT

per year, which is three time greater than the maximum decay rates seen in historical models. They say that the recurrence of low field values over southern Africa might be explained by flux expulsion which would lead to pairs of normal and reversed flux patches. This takes place at the edges of the low shear velocity patch and might trigger reversals for millions of years.

1.4 Goal of this work

In general this work tries to bring more light in the evolution of the magnetic field and especially of the dipole moment over the last 1000 years. The results should mainly be influenced by the data and not by additional constrains on the dipole coefficients to accommodate for missing data. Because the influence of the data should outweigh other parameters it is important to know which data is more reliable and this was also one of the important tasks of this work.

Further it is important to evaluate the robustness of the model results with this modelling technique regarding changes in the data or data uncertainties. This allows to estimate the credibility in specific magnetic field features to further interpret the results.

The biggest challenges in this work were:

- *Challenge:* Unknown information value in terms of physical interpretation of archeo- and paleomagnetic models calculated at the core-mantle boundary. It is unclear how accurate are field values calculated at core mantle boundary.

  Approach: Calculation of many models with random uncertainties of all data to assess stable structures at the core mantle boundary throughout all the models.

- *Challenge:* Extreme differences in spatial data coverage in earlier times having the biggest part of the archeo- and paleomagnetic data in the northern hemisphere.

  Approach: Minimize the effect of uneven data coverage when modelling to get the smoothest model which still fits the data reasonable well.

- *Challenge:* Extreme differences in the data count before and after 1800 AD which leads to big differences in the resolution and probably to artificial structures in the models.

  Approach: The implementation of a time dependent constraint which regulates the complexity of the model.

- *Challenge:* The uncertainty of archeo -and paleomagnetic data is normally estimated as the standard deviation of the mean which can give extreme wrong weightings for the modelling. This is because many factors can influence the validity of the paleomagnetic results like chemical alteration of the samples or magnetic overprint from other sources then the Earth's magnetic field.

  Approach: Calculation of many models based of data with random uncertainties and comparison to gufm1 to asses possible criteria for reliable data as a foundation to assign uncertainties independent of the ones given by the authors.

1.5   New magnetic data from Fogo

The most important ingredient for a good magnetic field model is accurate and well distributed data. The current data distribution has a lot of data in Europe and in North America but in general very few data in the southern hemisphere and the African area. Especially in this area data would help to constrain the evolution of the South Atlantic Anomaly which is the biggest and most intriguing Earth's magnetic field feature we know today.

Volcanic samples from the Island Fogo which is part of Cape Verde approximately $700km$ west of Senegal were made available to me by Dr. Maxwell Brown (University of Iceland, Institute of Earth Sciences). The ages of the collected samples span between 1662 to 1847. These samples present suitable test data to compare with the model, and also a good opportunity to practice the lab work to recover ancient magnetic field values and to better understand the quality of the experimental results.

New paleointensities are presented from 1663 ± 1, 1771.5 ± 2.5, 1755 ± 30 and from 1847. One directional record including inclination and declination could also be gained from 1847. These new records are compared with our new 1000 year model arhimag1k in chapter 6.

1.6   Overview of the following chapters

Chapter 2 is a description of the data which will be used for modelling in this work. It will give detailed information about the origin and properties of different data subsets.

Chapter 3 explains the modelling method and adaptations that I developed and implemented in this work. It first shows the problems that arise with the original modelling and then presents possible ways to minimize these problems that arise from the uneven data distribution and the uncertainty of the data.

Chapter 4 will be a statistical analysis of archeomagnetic- and volcanic data which will give important conclusions on data uncertainties and possible data weighting of different data subsets for geomagnetic field modelling. It also gives indications of model uncertainties and a rough idea which physical interpretations might be possible from resulting models.

Chapter 5 will show the characteristics of the model which resulted from a combined database of archeomagnetic, volcanic and historical data and the in chapter 3 described modelling method.

Chapter 6 shows 4 new volcanic intensity records and one directional record from the Island Fogo of Cape Verde and compares them to existing models. Further the reliability of paleomagnetic data and their currently used quality parameters is discussed.

Chapter 7 summarizes the most important results and gives an outlook to possible future works.

Chapter 2

The data used for modelling

2.1 Historical data

Historical data are direct measurements of the Earth's magnetic field. Early measurements of declination mostly originate from logbooks of ships for the purpose of navigation. These ships were in general part of trading companies or naval units for earlier times. Inclination data is also available from ship logbooks or land surveys but in fewer numbers. The measurement of the relative intensity was first introduced by Alexander Humboldt around 1800 [von Humboldt and Biot, 1804]. These intensities were acquired by comparing the oscillation rate of a standard dip-needle to the outcome with the value obtained at a reference point. Unfortunately there are no absolute intensities of the magnetic field available before 1832. Only then C. F. Gauss [1833] developed a method for the determination of absolute intensities. More recent sources of historical magnetic field data are observatories and satellites.

2.1.1 Historical data for geomagnetic modelling

The data that will be used here is in general the same data that was used to construct the model gufm1 [Jackson et al., 2000] which is described in detail in the works of Bloxham et al. [1989], Hutcheson and Gubbins [1990] and Jonkers et al. [2003]. Observatory and satellite data only add magnetic field information in the very recent times and are not used in this work which mainly aims to make a good estimation of the dipole moment for the last 1000 years by combining data sources which already have a very large difference in uncertainties.

Possible problems of historical data, which are also described in Jonkers et al. [2003], can be illustrated by some early voyage selected as examples for this work. Figure 2.1 shows the residuals of the declination measurement to gufm1 from the voyage of the ship Ceres 1785 to 1786. Because it was difficult to determine the longitude on sea the travelers usually tried to sail along lines of constant longitude until they reached a certain latitude and then traveled along a path of constant latitude. In this voyage the residuals are small as long as they didn't change the longitude or reached a landmark to orient themselves. Another problem could be a systematic bias in the measurements which seems to be the case in Figure 2.1 b where the measured inclination is around 10 degrees smaller then gufm1 would predict. Reasons for this systematic bias could be defect instruments, iron used in the ships construction or in this case more likely the problem of high latitude which lead the compass needle to get pulled downwards and affecting the reading of declination through higher friction. This would make inclination measurements difficult because it is necessary to align the compass with the local declination.
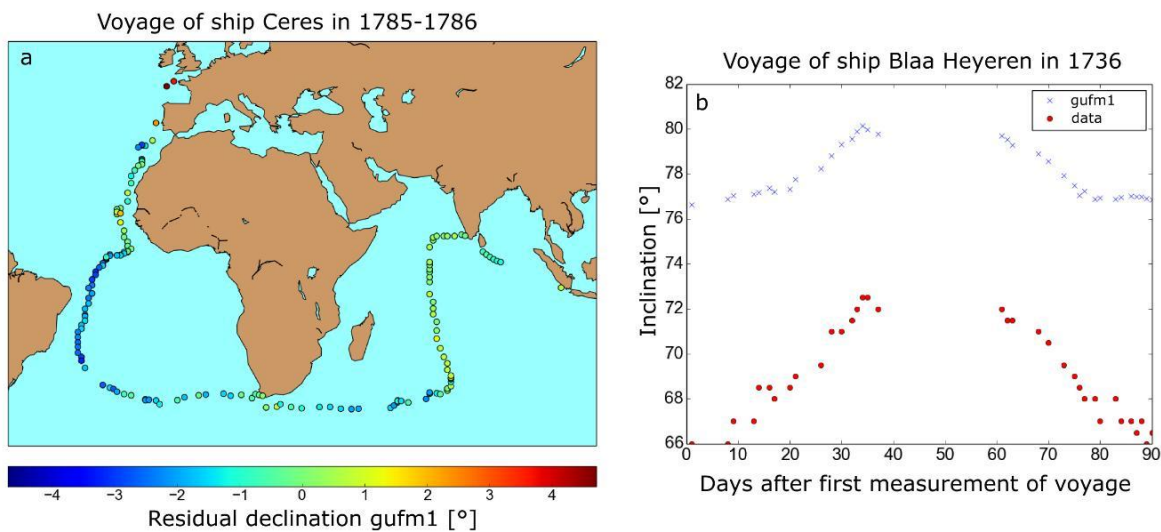
FIGURE 2.1: Residuals of measurements from two selected early voyages with gufm1 calculated by subtracting the model values from the data. a) Voyage of ship Ceres showing higher residuals to gufm1 if longitude is changed. b) Voyage of ship Blaa Heyeren shows a constant offset in inclination to model values gufm1.

Another example of really high inclination residuals is shown in figure 2.2 with the voyage of La Pérouse from 1785 to 1788 where inclination measurements seem to agree very well with gufm1 at first but have a systematic bias in the pacific ocean in a later part of the voyage. La Pérouse along with his crew vanished somewhere close to Australia on this expedition after he managed to send some documents back to Europe.

The simplest and at the same time most extreme source of uncertainties are transcription errors, which is probably the case for the declination data in figure 2.3 from a region near Brazil (around
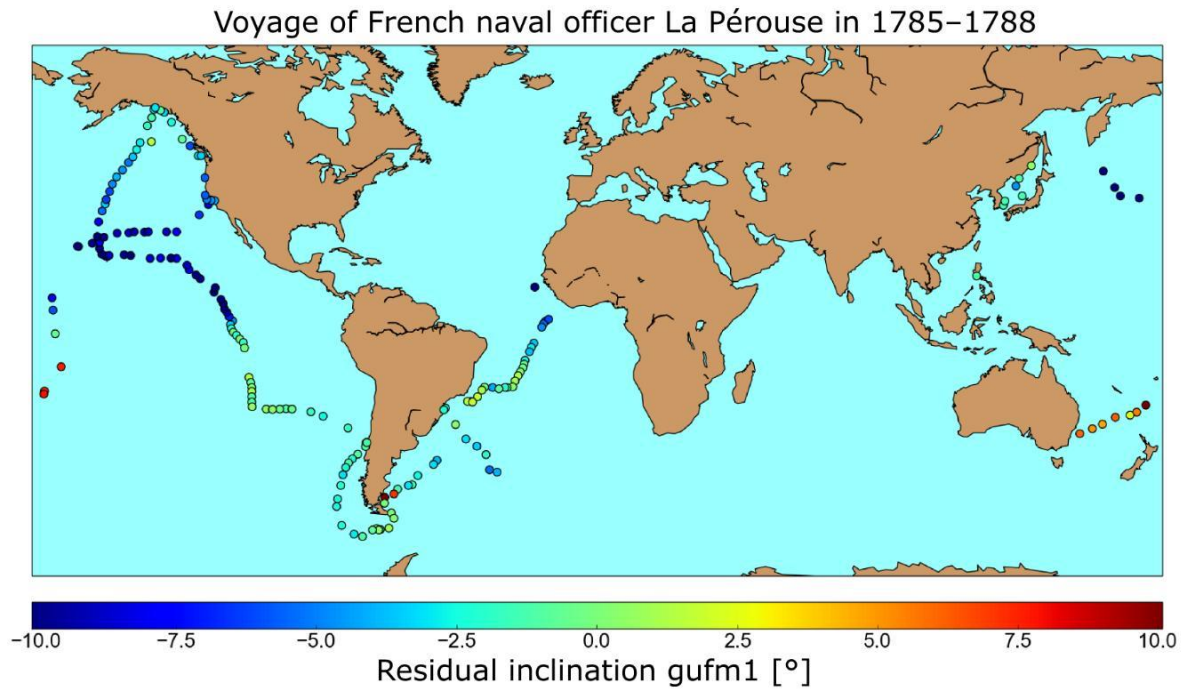
FIGURE 2.2: Voyage of the French naval officer La Pérouse which shows big residuals for inclination to gufm1 in certain locations. The last measurements near Australia are higher then gufm1 values and in the vicinity off Hawaii one finds negative residuals.

-25 degree latitude and 310 degree longitude). An explanation for these outliers could either be, that a minus sign was falsely added for the declination measurements or a minus sign for the longitude, which for some data is defined from -180 to 180 degrees. Assuming this, these data outliers would be placed near Madagascar where other declination data exists with similar values. For comparison the model values of gufm1 close to Madagascar and close to Brazil are also plotted in figure 2.3. These outliers are part of a compilation of many voyages collected from the Bibliotheque Nationale in Paris.

The previous examples make it clear that one has to be very careful to just include all available data in the modelling. A strict rejection or weighting scheme is necessary to avoid big systematic errors in the global magnetic field model.

2.1.2 Temporal distribution and Spatial distribution

The temporal distribution of the historical data is very dependent on the technical progress of measuring the magnetic field and to determine the latitude and longitude of the measurement location accurately. Figure 2.5 shows the temporal distribution of the historical database for
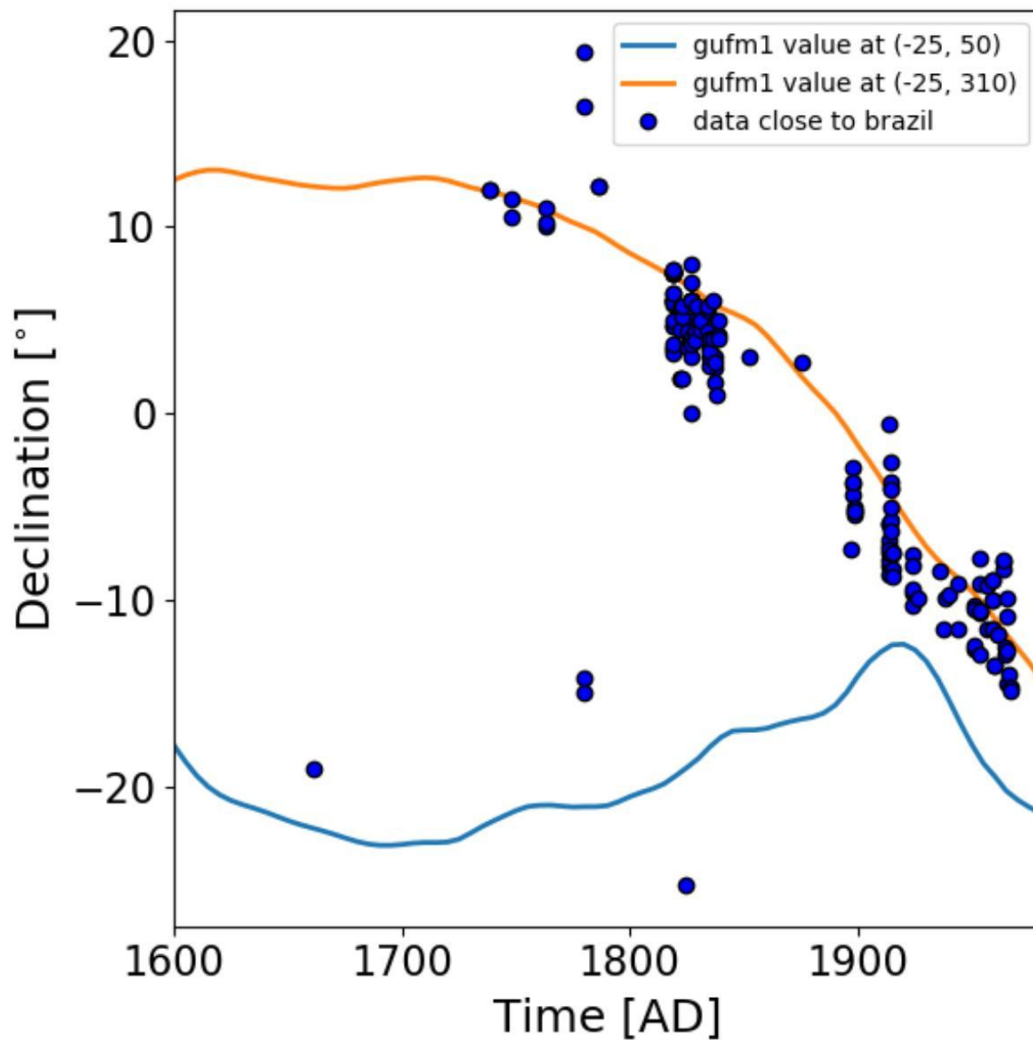
FIGURE 2.3: Data from a region near Brazil (around -25 degree latitude and 310 degree longitude) with some clear outliers probably due to a wrong negative sign in front of longitude value. Model values of gufm1 are plotted for comparison.

the different data types declination, inclination, intensity and horizontal component of the intensity. The declination was already measured since the 15th century and is apart of a few early inclination measurements the only source of direct magnetic field data in earlier times. From 1800 onward there is also a decent number of inclinations and historical absolute intensity data of the magnetic field is only available from 1832 AD onward.

In general the directional historical data provides a good coverage of the oceans for the last 400 years especially over the Atlantic and Indian ocean. Historical absolute intensity data of the magnetic field is giving a good continental coverage especially over Australia, North America, Japan and Europe for the last 150 years (figure 2.4).
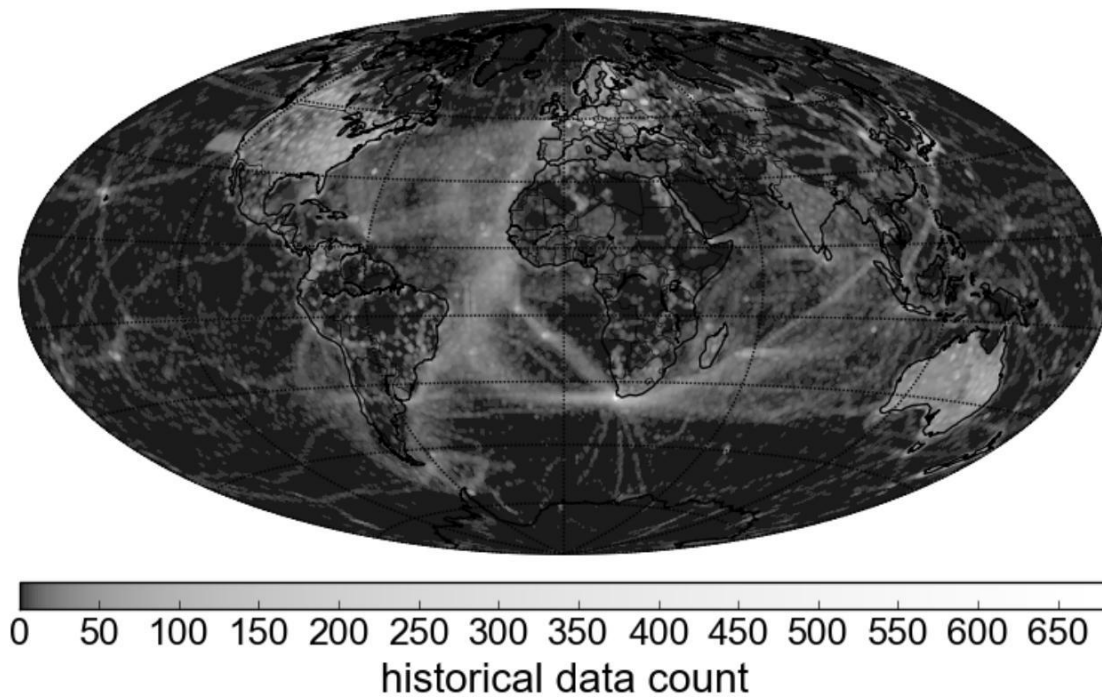
FIGURE 2.4: Global historical data count of the last 400 years. The greyscale is logarithmic and shows the number of data for all magnetic field components binned in 1×1 degree areas.

2.2 Archeomagnetic and volcanic data

The archeomagnetic and volcanic data used in this work originate from an export of GeoMagia50.v3 database ([Donadini et al., 2006],[Brown et al., 2015]) in February 2015. The only filter for the export was the estimated age of the sample falling in the time interval between 800 and 2000 AD.

Archeomagnetic and volcanic data are based on indirect measurements of the Earth's magnetic field from samples collected at different sites on Earth. These samples either stem from man-made materials or from volcanic regions that were active in the past. The bar chart in figure 2.6 shows the data counts used in this work sorted by the type of magnetic field data and the materials used in the experiments. Only samples with a geographic orientation can be used to determine the ancient field direction. Samples which do not provide any information about their orientation at the time the magnetisation was acquired are not usable to make any estimation about the direction of the ancient magnetic field. For example in the case of pottery where the
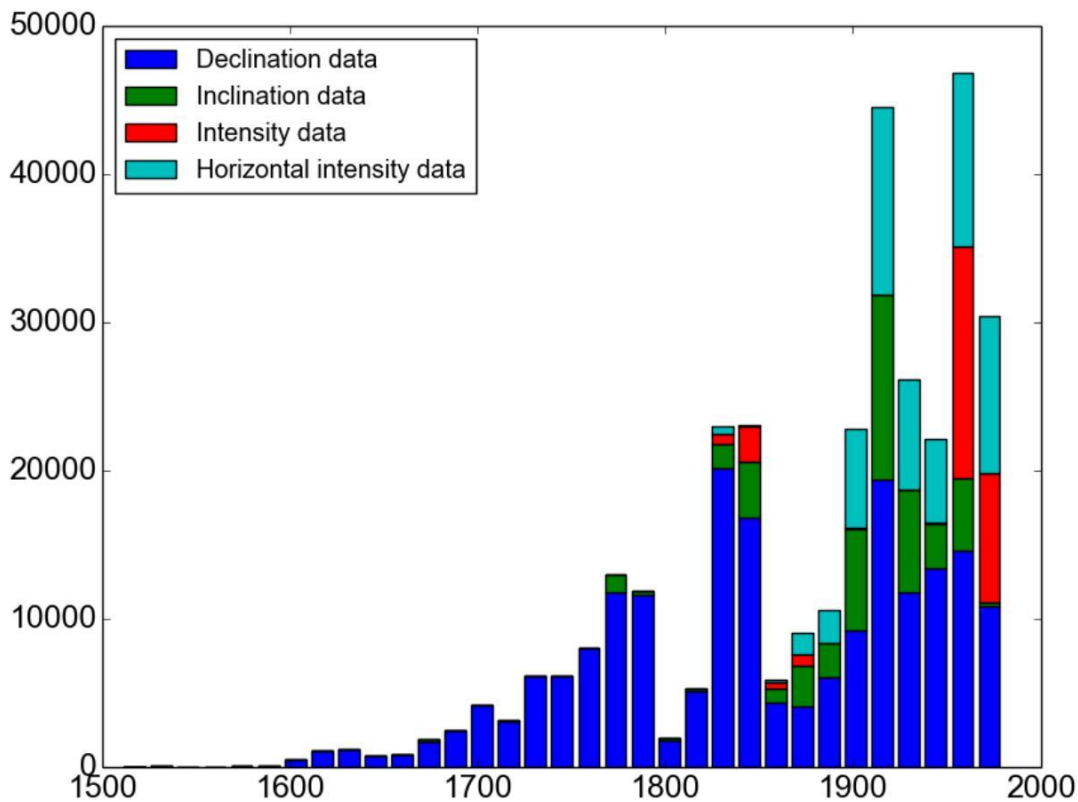
FIGURE 2.5: Historical data count over time in a stacked histogram of declination, inclination, intensity and horizontal intensity data

magnetisation is acquired by cooling down after getting heated up in an oven. In general it is not possible to determine the orientation of the sample when it was cooling down. In the case of brick samples it is reasonable to assume that the sample cooled down on the bigger flat side and further multiple bricks from the same side can be tested to validate this assumption. This allows a determination of inclination values of the ancient magnetic field. The declination cant be determined from bricks, because the horizontal orientation is completely unknown. Only the exact knowledge of the orientation makes it possible to determine declination and inclination. This is the case for materials that were found exactly at the location at which they cooled down. For example oven and hearth, kilns or lava flows which weren't affected by post-cooling rotation. Paleointensity can be determined from all samples in a time consuming way, but it is important to be very careful in interpreting the results (see chapter 6).
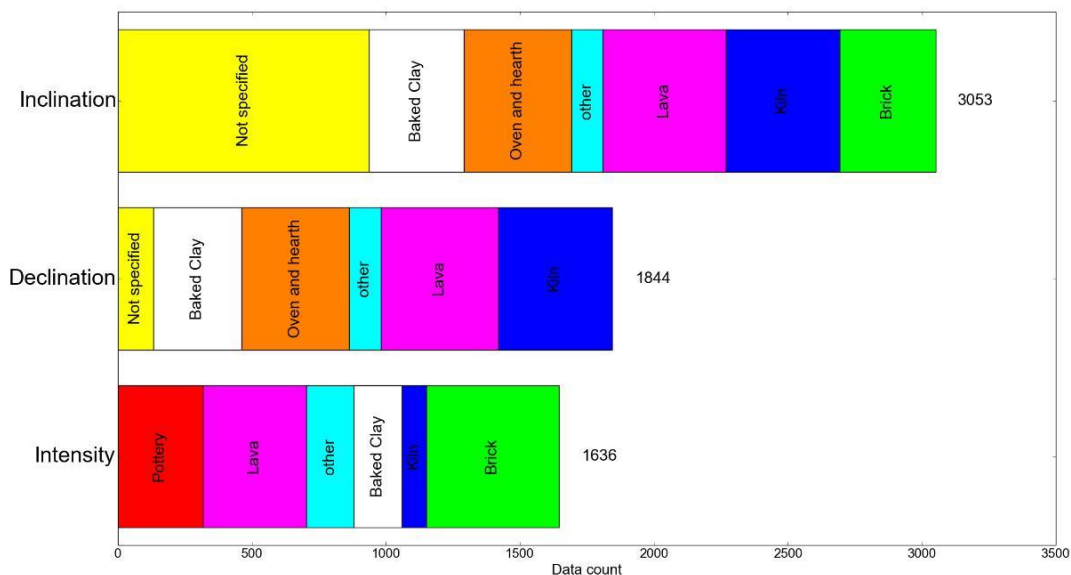
FIGURE 2.6: Data count of different sample materials

2.2.1 Temporal distribution and spatial distribution

The geographic sampling is very limited, either by human or volcanic activities in the past. That also means that there is almost no sampling of oceanic regions, other than a few samples collected at oceanic ridges. Human activity in the past and also a needed accessibility to sample sites are mostly limited to regions in Europe and Northern America (Figure 2.7). Only in the last years there is more and more data available from the southern hemisphere, but still not close to enough to trust the small scale magnetic field structures in archeomagnetic and volcanic magnetic field models.

Figure 2.8 shows how the data count used in this work changes in time (bins of 50 years). On average there are around 300 data points for every 50 years. For the directional data the material was often not specified, which explains that the data count for the single materials don't add up to the data count of all data. For the earlier times there are mostly baked clay and kiln data while the volcanic data takes over in the more recent times, where the date of the eruption is still known through historical documents or time testifies.
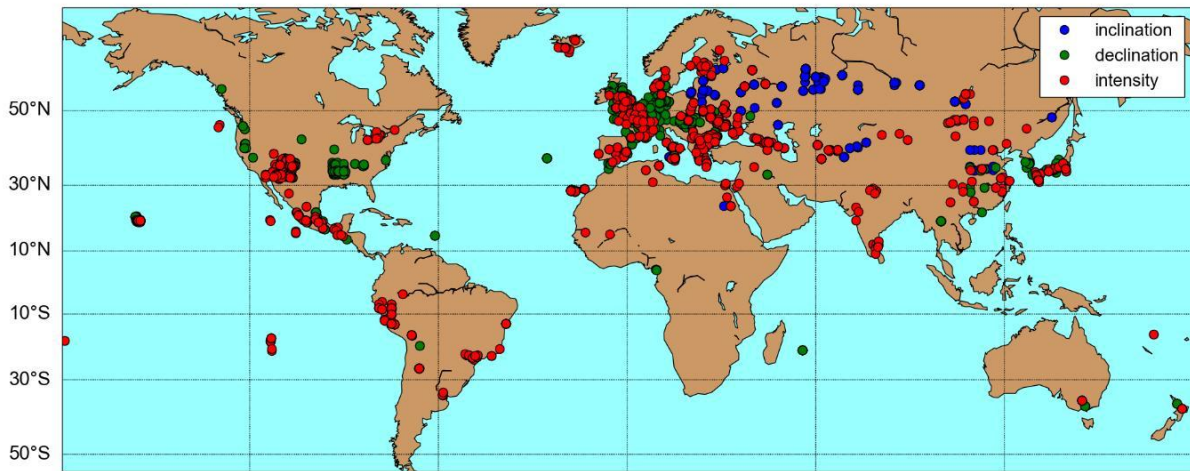
FIGURE 2.7: Spatial distribution of the archeomagnetic and volcanic database
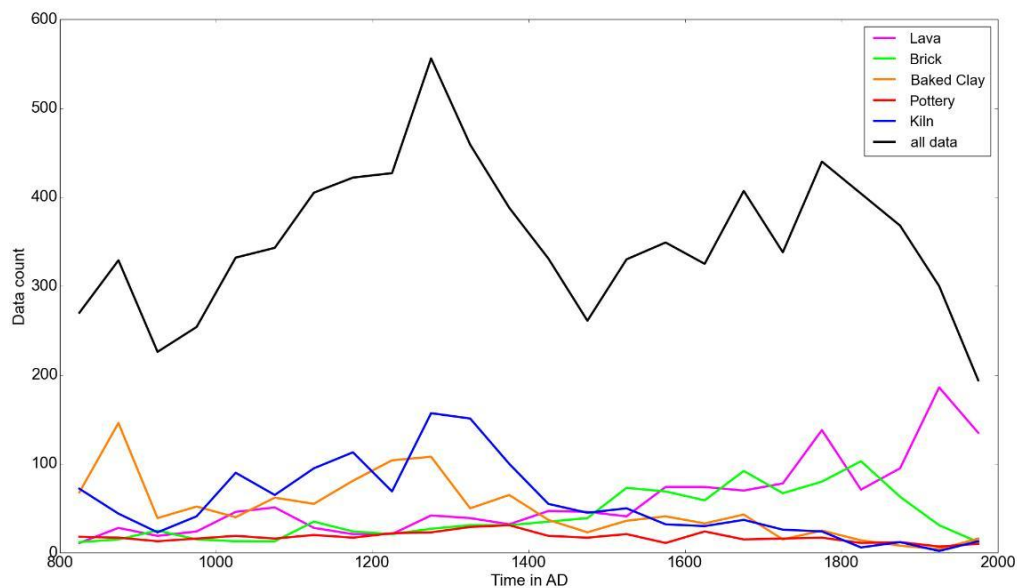
FIGURE 2.8: Temporal distribution of the archeomagnetic and volcanic database

2.2.2 Possible systematic errors in determining the ancient magnetic field

There are many different systematic errors that can contaminate the paleomagnetic and archeo-magnetic data. Sometimes the age of a sample can only be determined to a poor accuracy, which even when the measurements were successful leads to problems for geomagnetic modelling and big uncertainties. When using volcanic samples for the determination of the ancient field directions, it is important that the sample site hasn't rotated after the acquisition of the magnetisation. This could possibly happen in a highly active volcanic region. Furthermore a

really strong magnetic anomaly from an earlier volcanic eruption could influence the magnetisation. Another possibility is that volcanic eruptions that occurred after the one that is of interest could have reheated the material and changed the magnetisation of older volcanic flows. Another more extreme case of alteration would be due to lighting close to the sample, which would completely overwrite any magnetic imprints from earlier times. Fortunately this kind of alteration is easy to distinguish in the laboratory, because this type of magnetisation is usually very strong compared to the samples which were not exposed to lighting.

An example of systematic errors can be found by looking at residuals from recent volcanic inclination data to the historical gufm1 model. One can observe a bias to lower values (Figure 2.10). Here all volcanic inclination data from the database GeoMagiav3 were compared with calculated values from gufm1 [Jackson et al., 2000] and also a Laplace function was fitted to the histogram, which was also done in a previous study by Pavón-Carrasco et al. [2014]. This inclination shallowing is not fully explained yet but especially the effect of deflection of the magnetic direction due to the demagnetizing effect of shape anisotropy ([Coe, 1979], [Abrahamsen, 1989], [Knudsen et al., 2003]) seems reasonable.

Another systematic error can be found in paleointensity data, when the cooling rate of the laboratory experiments differs strongly from the actual cooling rates during the acquisition of the NRM (in this case TRM). In the laboratory the samples generally cool the much faster then the sample cooled in ancient times. Especially volcanic material cools extremely slow if the eruption is very continuous and not explosive.
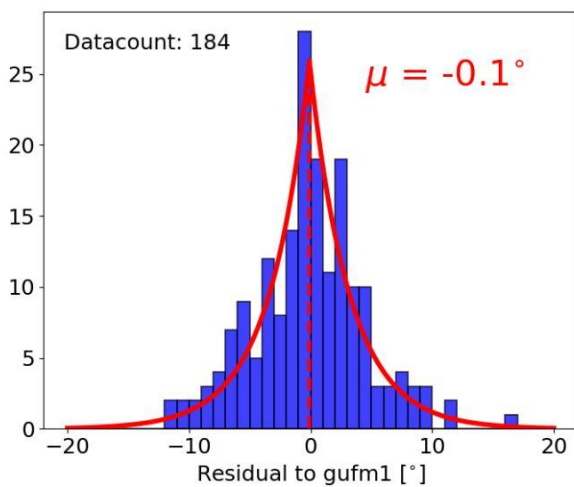
FIGURE 2.9: Residuals brick inclination
data to gufm1 model
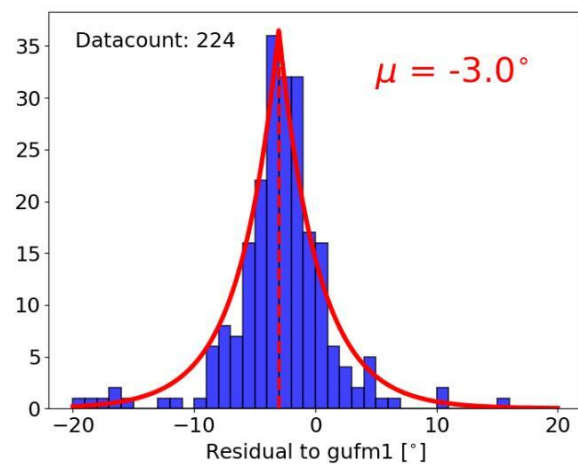
FIGURE 2.10: Residuals lava inclination
data to gufm1 model

2.3 Comparison between archeo/paleomagnetic and historical data
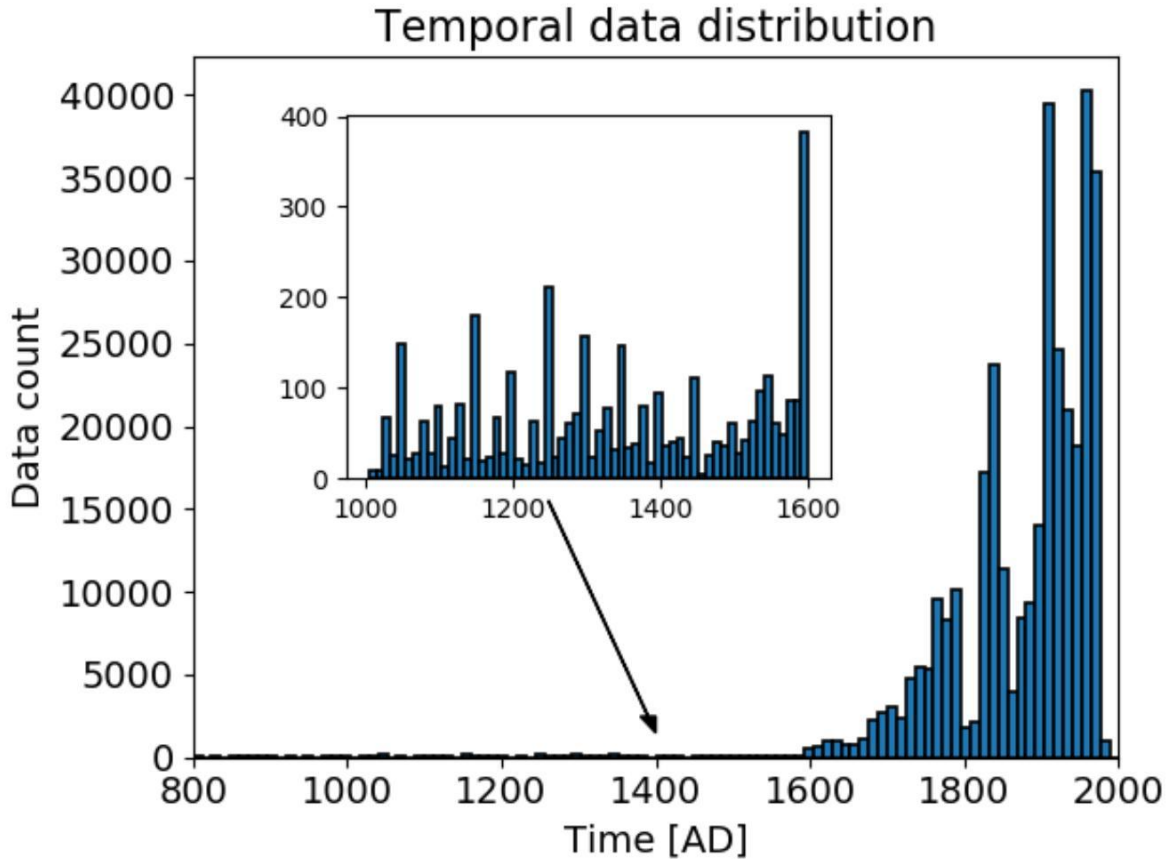
FIGURE 2.11: Temporal distribution from the combined database of archeomagnetic/volcanic and historical data with a zoomed panel at times before 1600 AD

Compared to historical data the archeomagnetic- and volcanic database is very sparse. To illustrate this difference figure 2.11 shows the temporal data distribution of the combined database in time with a zoomed panel on the data before 1600 AD which is manly archeomagnetic and volcanic data. In the last 400 years the historical data dominates very strongly. While earlier times with only acheomagnetic and volcanic data have only around 30 to 40 data points every 10 years, the historical database has up to 40000 data points in 10 years. Even the historical data has a big difference between the time span of 1600 AD to 1800 AD and the time span of 1800 AD to 2000 AD, where the data count increased drastically. This circumstance leads to problems when trying to model the Earth's magnetic field with that combined database which will be explained more in detail in chapter 3.

Figure 2.12 shows the residuals of the archeomagnetic and volcanic data to the gufm1 model with time. There is a clear trend, which can be seen in the linear fit, that older data seems to be in a bigger disagreement with the historical model than younger data. That is probably mostly attributed to the increasing age uncertainty of the magnetic samples with their estimated age. Another reason could be that it is more probable for chemical altering or changes in the magnetisation (i.e. because of lightning or strong heating) to occur in older samples. Another possibility is that the model itself is more inaccurate in earlier time which will also be the case. The quality of the data which went into generating the gufm1 model depends massively on the technology and the quality of the measurements and the measurement devices which were strongly improving in time. This figure also shows that if no uncertainty of archeomagnetic-/paleomagnetic data is known 5000 nT for intensity and 3.5 degrees for directional data seems to be a good approximation for that quantity.

Figure 2.13 shows the residuals of the historical data used here in this study to the gufm1 model. In general these residuals are much lower then for the archeo-/paleomagnetic data which is expected because this data was actually used to compute the gufm1 model. Also the data is from direct measurements of the magnetic field, which are much more accurate then archeo- and paleomagnetic data from indirect measurements. In general the residuals with time have also a trend of decreasing. The reason is again the quality of the data improving with time and also the increasing data count, which better constrains the model. Especially the residuals of the inclination are relatively big before 1800 AD, which could be due to only very little and maybe inaccurate inclination data from that time.
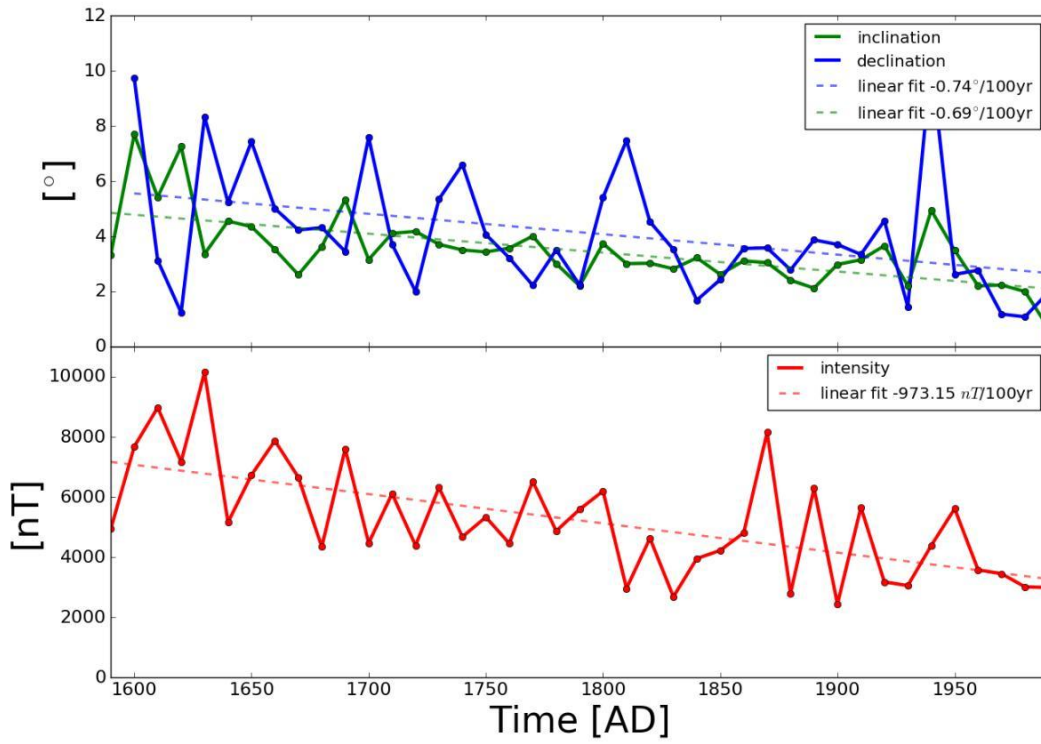
FIGURE 2.12: Residuals of archeomagnetic/volcanic data with time
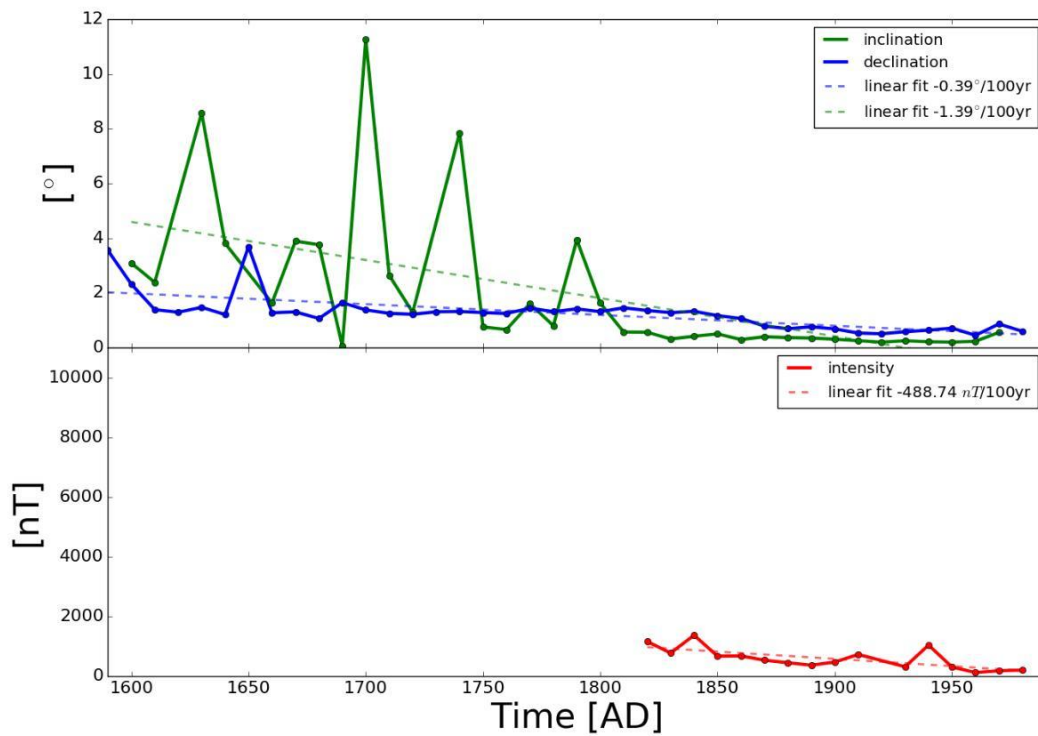
FIGURE 2.13: Residuals of historical data with time

2.4 Consistency of the different data types

Depending on the region, data type and time there are big differences in consistency and accuracy of the data. Especially for archeomagnetic and volcanic data this depends on how well the age of a sample can be determined. In areas where the history is very well documented like in Europe it is easier to determine a reasonable age and to find suitable samples. The accessibility and the historical knowledge of other regions like Africa is far less and hence the consistency of existing data is much worse.
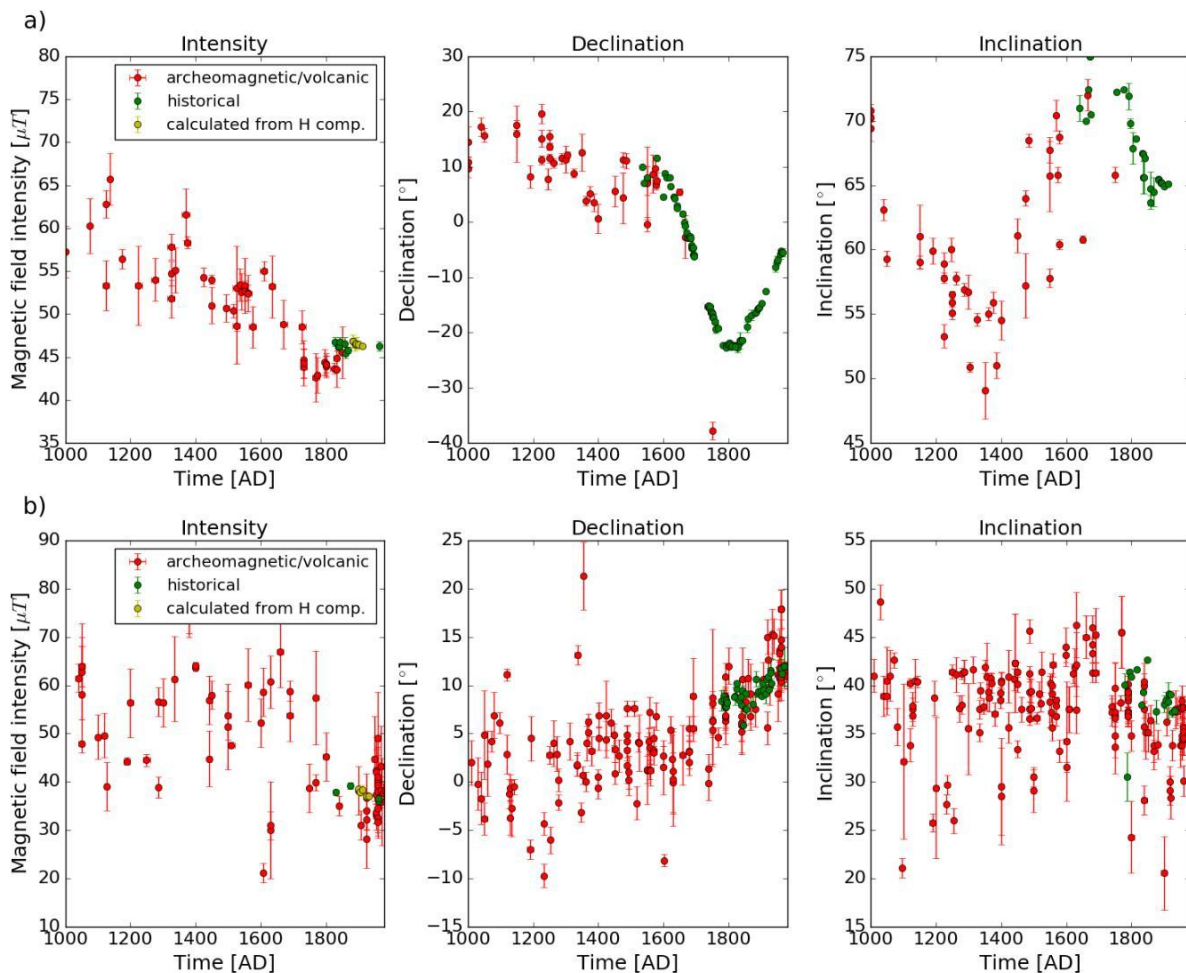
FIGURE 2.14: a) Time series of all French data in the region from 44° N to 50° N and 0° to 6° E b) Time series of all Hawaiian data in the region from 18° N to 22° N and 153° W to 157° W

Figure 2.14 shows two extreme cases of regional data consistency. The upper panel includes all data in a region of France and the lower panel shows all data from a region of Hawaii. While the French data is very consistent, the Hawaiian data does not show very clear trends of secular variation. Especially data before 1800 AD is very inconsistent and spans over a big range of

values in a short amount of time. The main reason for this big difference in consistency in these two regions is that Hawaiian data is mostly volcanic data, which tends to lead to more inconsistent results than archeomagnetic data. An assumption for this kind of data is that the average of all values is a reasonable approximation to the ancient magnetic field, if a lot of data is available.

Chapter 3

Modelling method

3.1 Global Earth magnetic field modelling with spherical harmonic expansions

The spherical harmonics are used for modelling problems with a spherical geometry, i.e. gravity fields, wave functions in quantum mechanics or in this case magnetic fields. A detailed description of the the modelling method used in this work is written by Jackson et al. [2000] and Bloxham and Jackson [1992].

The Earth magnetic field can be represented by the negative gradient of a scalar potential V, written in the geocentric reference frame, is a function of the radial distance from the center of the Earth r, the colatitude Θ and the longitude Φ. At regions where current density is negligible according to Maxwell equations applies

$$\vec{B} = -gradV \tag{3.1}$$

This assumption generally is good for radial distances down to the core-mantle boundary where no or negligible small electric currents are flowing. Inside the outer core where the Earth's magnetic field is generated this assumption cant be used to invert for the magnetic field. The magnetic potential V in form of a spherical harmonic expansion writes

$$V = a \sum_{l=1}^{L} \sum_{m=0}^{l} \left(\frac{a}{r}\right)^{l+1} \left[g_l^m(t)\cos\left(m\phi\right) + h_l^m(t)\sin\left(m\phi\right)\right] P_l^m(\cos\left(\theta\right)) \tag{3.2}$$

where $g_l^m(t)$ and $h_l^m(t)$ are expansion coefficients known as the Gaussian coefficients, P_l^m are the Schmidt quasi-normalized associated Legendre functions and a is the average radius of the Earth. In this study the truncation degree is chosen to be L = 10. The Gaussian coefficients are taken to be time dependent and they are parameterized in the following way:

$$g_l^m = \sum_n {}^n g_l^m B_n(t) \tag{3.3}$$

where $B_n(t)$ is the nth order B-spline function. The set of all ${}^n g_l^m$ and ${}^n h_l^m$ builds the model vector $\vec{m}$ with a dimension of $TL(L+2)$ where T is the number of knot points in time.

The available data count in the time before 1600 is partially very low and is heavily located in the northern hemisphere. Therefore it is necessary to use regularization to achieve a smooth model in time and space, that doesn't show any artificial features or structures. The spatial regularization is done by minimizing the ohmic heat dissipation at the CMB. The ohmic heat dissipation is represented by the following integral:

$$\Psi = \frac{1}{(t_e - t_s)} \int\limits_{t_s}^{t_e} \mathcal{F}(B_r) dt = \vec{m}^T S^{-1} \vec{m} \tag{3.4}$$

with $B_r = -\partial_r V$ being the radial magnetic field at the CMB, t_s the starting time of the model and t_e the end time of the model. $\mathcal{F}$ is the quadratic norm which is connected with the minimum ohmic heating at the core mantle boundary that is demanded and the quadratic norm writes,

$$\mathcal{F}(B_r) = 4\pi \sum_{l=1}^{L} \frac{(l+1)(2l+1)(2l+3)}{l} \left| \frac{a}{c} \right|^{2l+4} \sum_{m=0}^{l} \left[(g_l^m)^2 + (h_l^m)^2 \right] \tag{3.5}$$

where $c = 3485 km$ is the core radius. This term will be called spatial norm or synonymous "spatial complexity" later.

The temporal regularization is realized with a quadratic norm which includes the second derivative of the radial component of the field at the CMB:

$$\Phi = \frac{1}{t_e - t_s} \oint_{CMB} \left(\partial_t^2 B_r \right)^2 d\Omega dt \tag{3.6}$$

The model vector $\vec{m}$ is estimated by minimizing the following objective function:

$$\Theta(\vec{m}) = [\gamma - f(\vec{m})]^T \, C_e^{-1} \, [\gamma - f(\vec{m})] + \lambda\Psi + \tau\Phi, \tag{3.7}$$

where γ is the vector containing the data and C_e is the associated data error covariance matrix, which everywhere in this work is diagonal and doesn't account for any possible correlation of uncertainties. The uncertainties in this methodology are assumed to be Gaussian which allows the use of least-squares for the estimation of the model $\vec{m}$. This assumption might not hold for all data sets. To achieve more robust models, outliers from the input data set i.e., data that give rise to high residuals get rejected.

A good tool to investigate, which degree l most contribute on average to the magnetic field is a spatial power spectrum. The Lowes-Mauersberg equation (Peter Mauersberger [1956], F. J. Lowes [1966]) for the power spectrum $P(l)$ is:

$$P(l) = (l+1) \left| \frac{a}{c} \right|^{2l+4} \sum_{m=0}^{l} \left[(g_l^m)^2 + (h_l^m)^2 \right] \tag{3.8}$$

The actual magnetic field values can be calculated from the potential with the model function f which is depending on the data type (declination D, inclination I, intensity F, horizontal intensity H, north component X, east component Y, vertical component Z):

$$X = \frac{1}{r}\frac{\partial V}{\partial \theta}, \quad Y = \frac{1}{r\sin\theta}\frac{\partial V}{\partial \phi}, \quad Z = \frac{\partial V}{\partial r} \tag{3.9}$$

$$H = \sqrt{X^2 + Y^2}, \quad F = \sqrt{X^2 + Y^2 + Z^2}, \quad D = \arctan\left(\frac{Y}{X}\right), \quad I = \arctan\left(\frac{Z}{H}\right) \tag{3.10}$$

The non-linear nature of the model equations for intensity, declination and inclination which represent the data set used in this study it is necessary to search the model vector $\vec{m}$ through iteration:

$$m_{i+1} = m_i + \left(A^T C_e^{-1} A + C_m^{-1}\right)^{-1} \left[A^T C_e^{-1}(\gamma - f(m_i)) - C_m^{-1}m_i\right] \tag{3.11}$$

with $C_m^{-1} = \lambda_S S^{-1} + \lambda_T T^{-1}$ including the spacial and temporal smoothing terms.

The λ_S and λ_T being the spatial and temporal damping parameters regulate the amount of smoothing to achieve the best trade-off between extracting from the data as much information as possible and avoiding artefacts in the model by over-fitting the data.

In every iteration of the modelling process the data is compared to the current model. If the residual of the data point is higher then a certain threshold, this data point is excluded from the next iteration. The rejection threshold was chosen to be relatively low for the historical data for two reasons. Firstly the data count compared to archeomagnetic and paleomagnetic data is very high and with this choice only the most consistent data is used for the modelling. Secondly a better balance between the number of historical and archeo-/paleomagnetic data is achieved.

	Intenstiy [nT]	Declination [°]	Inclination [°]	Horiz. intensiy [nT]
archeo-/paleomagnetic data	13600	13.6	15.3	-
historical data	8000	2	2	4000

TABLE 3.1: Data rejection threshold for the different data types

3.2 Existing Models and individual differences

The following models span over a time of the last 200 years to the last 14000 years. There are many more models which cover a much shorter or longer time scale, but these are not further described or mentioned because this work will concentrate on the main field of the last 1000 years.

3.2.1 Model gufm1 by Jackson et al. [2000]

This model spans from 1590 to 1990 AD and includes ship log data, observatory data, satellite data and survey data. The maximum degree of spherical harmonics is $L = 14$ and the time spacing is 2.5 years. It is important to note that this model only uses absolute intensities from 1840 onward and consists mostly of declination measurements. Also there are very few inclinations in the compiled database before 1800.

3.2.2 Model CALSxK ([Korte and Constable, 2005],[Korte et al., 2011] ,[Korte and Constable, 2011])

The CALS series of models span over different time periods, from the last 10000 years to the just focusing on the last 3000 years. The maximum degree of spherical harmonics was chosen to be $L = 10$. The knot point spacing in time is different in the individual models and varies between 10 to 55 years. In the recent models of this series all Gauss coefficients were additionally constrained by penalizing departure of the model coefficients from the model gufm1. In particular the coefficient g_0^1 is constrained from 1840 to 1990 and all other coefficients from 1590 to 1990. These models are based on archeomagnetic, paleomagnetic and sediment data and rely on strong regularizations.

3.2.3 Model Arch3k.1 by Korte et al. [2009]

The Arch3k.1 model is calculated from merely archeomagnetic data. It has a higher spatial resolution than the CALSxK models which included sediment data. However, its reliability in the southern hemisphere is much lower then in the northern hemisphere due to lack of data. This model consists of 80 intensities, 20 inclinations and 20 declinations in the time between 1000 AD and 2000 AD.

3.2.4 Problems of existing models

The biggest problem for the above mentioned models are very unbalanced data distributions. Models based on historical data alone have no intensity data before 1832 AD and mainly fall back in declination data in this time. Models based on sediment or archeomagnetic data do no have sufficient data to achieve a high spatial and temporal resolution model. The input data sets of these models is especially sparse over the southern hemisphere. The model Arch3k.1 had 80 intensities, 20 declinations and 20 inclinations in the southern hemisphere from 1000 AD to today. Compared to that the database used in this study includes 145 intensities, 36 declinations and 36 inclinations. This should mitigate problem of sparse data coverage over the southern hemisphere. As a result a more accurate picture of the global magnetic field and the dipole moment can be achieved.
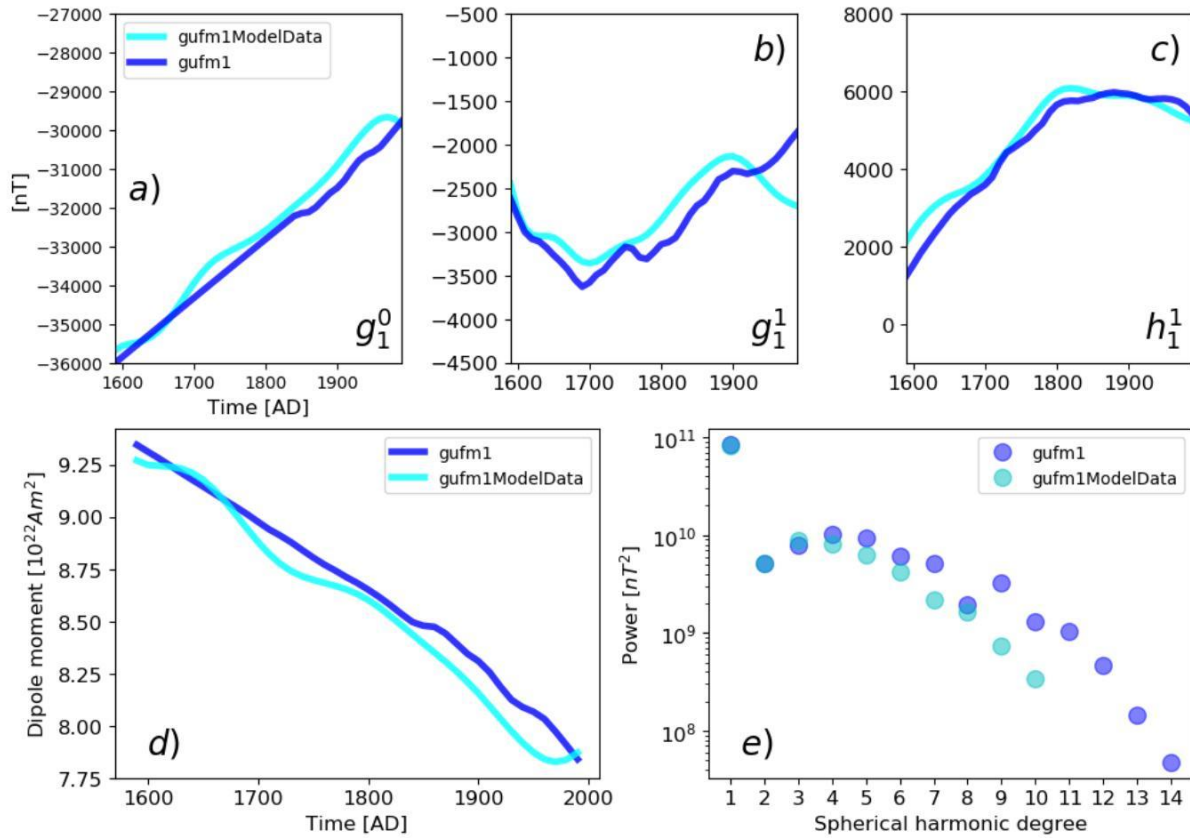
FIGURE 3.1: Panel a), b) and c) show the dipole coefficients of the test model (cyan line) compared to gufm1 (blue line). Panel d) shows the dipole moment and e) shows the average power in every spherical harmonic degree over 1000 years.

3.3 Test model for influence of data distribution on modelling outcome

For the purpose of inspecting the influence of data distribution on arhimag1k with the method described in this chapter, a test model was constructed which took calculated gufm1 magnetic field values at the location from the archeo-/paleomagnetic data as input data. This model will later be used to distinguish between influences of the actual data on the result and the influences of a certain data distribution. By comparing the dipole moment of gufm1 and the test model one can try to account certain model characteristics to a bad data coverage and maybe extrapolate a more accurate picture of the magnetic field evolution.

A comparison of dipole coefficients, dipole moment and power spectrum of the test model with gufm1 is shown in figure 3.1. Especially in the time between 1800 and 2000 the test model differs a lot from gufm1. It is apparent that the dipole moment is systematically lower than gufm1. This suggests that with the current archeomagnetic and paleomagnetic data distribution, the

absolute value of the first Gauss coefficient might systematically be too low, independent of the data quality. Nevertheless, the trend of dipole coefficient is very well reproduced in the main time period of the model, even with the bad data distribution of archeomagnetic and paleomagnetic data. The power spectrum shows which spherical degrees are influenced the most by the poor data distribution. While degree 3 has slightly higher power in the test model than gufm1, degrees equal to a higher than 4 fall of in power quickly. This suggest that the resolution should be quite similar until spherical harmonic degree 4. Because the power in this figure is averaged over 1000 years it helps to look also at the time evolution of the power to see the specific time periods over which the power differs the most. This time evolution can be seen in figure 3.2. According to this plot, the degree 4 of the test model has lower power in the later times. This is mainly because volcanic data of that time are available only on very limited locations on Earth.

3.4 Modelling parameters and adaptations for this work

The magnetic field model of this work was chosen to cover the time interval from 800 AD to 2000 AD, with knot points every 10 years. 800 AD was chosen to secure a model of the last 1000 while at the same time avoiding edge effects arising from the splines that are used to model the temporal variation of the field. The maximum spherical degree is set to $L = 10$, which is clearly higher than the expected resolution based on the data coverage, especially before 1600 AD (Korte et al. [2011]). This way the resolution of the model depends only on the data coverage and the strength of the applied damping rather than on the degree of truncation. The starting model was chosen to be a purely axial dipole field with $g_1^0 = -30\mu T$, with all other Gaussian Coefficients being set to zero.

The order of the B-spline functions is set to 4. The initial temporal and spacial damping parameters were estimated comparing the power spectrum $P(l)$ of the resulting models to the existing models gufm1 and Arch3k.1.

Comparing where the power spectrum of existing models like gufm1 and Arch3k.1 to a model derived from historical, archeo- and paleomagnetic data using a constant temporal damping brings forth an important problem. In particular, by choosing a very high damping parameter the model becomes very smoothed before 1500 AD (see figure 3.3 a) and after 1800 AD the higher degrees have unrealistically high power compared to gufm1 (see figure 3.3 b). This suggests the need of a time dependent spatial damping.
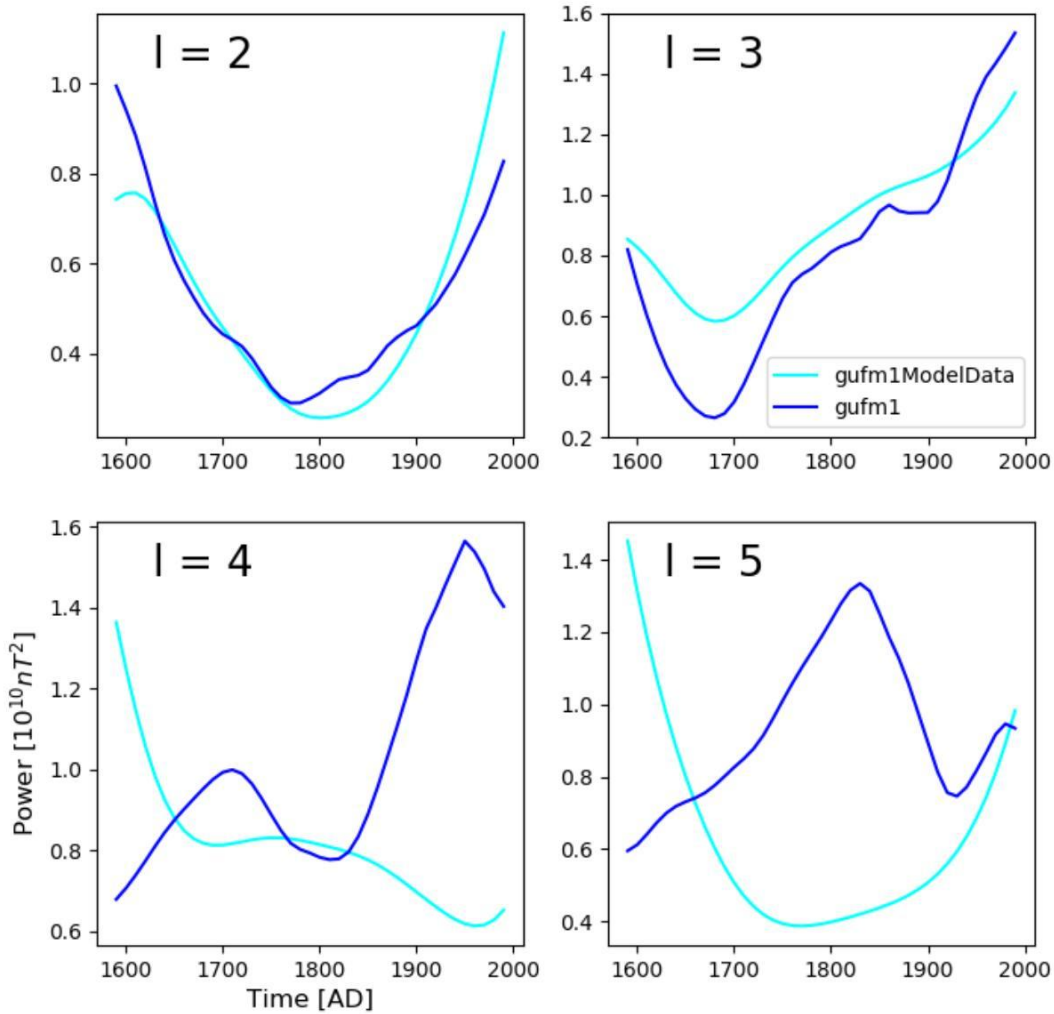
FIGURE 3.2: Time evolution of the power from spherical harmonic degrees $l = 2$ to $l = 5$ of the test model compared to gufm1.

Introducing a time dependent spatial damping parameter has been one of the main innovations of this work. The dimension of the initial damping parameter vector $\vec{\lambda}$ is that of the number of splines used, which in this case is 123. In the inversion, this damping parameter is included in the following way:

$$\Psi_\lambda = \frac{1}{(t_e - t_s)} \int_{t_s}^{t_e} \mathcal{F}(B_r)\lambda_t dt = \vec{m}^T S^{-1} \vec{m} \tag{3.12}$$

with λ_t being the spatial damping parameter at a specific time t.
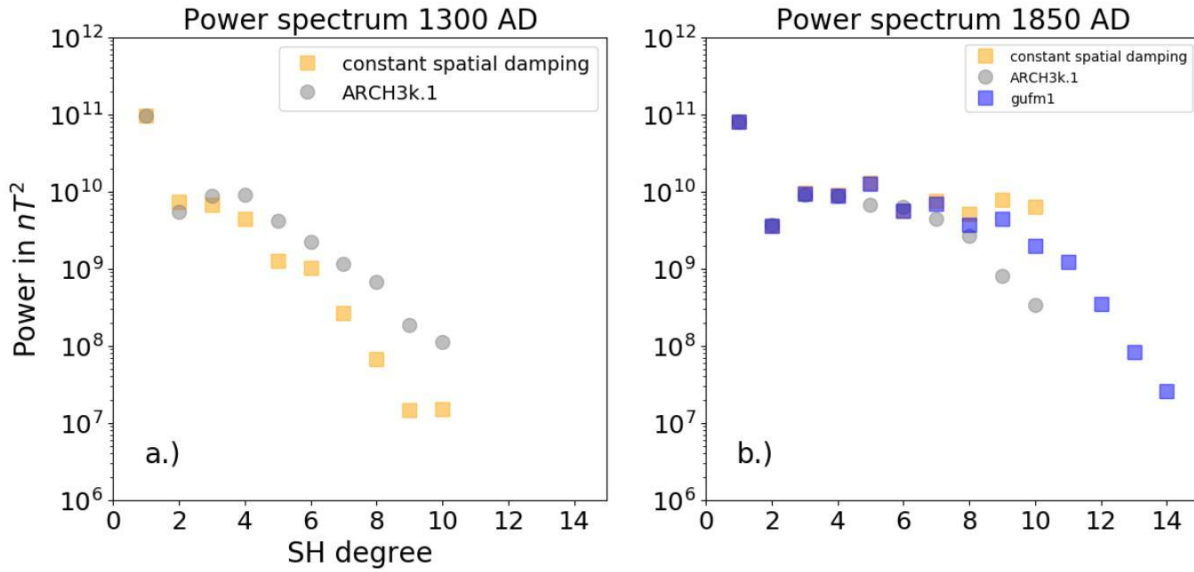
FIGURE 3.3: Power spectrum of the model with constant spatial damping at 1300 AD and 1850 AD compared to Arch3k.1 and gufm1

Then the function to minimize becomes:

$$\Theta(\vec{m}) = [\gamma - f(\vec{m})]^T C_e^{-1} [\gamma - f(\vec{m})] + \Psi_\lambda + \tau\Phi, \tag{3.13}$$

To determine the damping parameter vector $\vec{lambda}$, an iterative approach is used. Initially, the components of this vector are all the same. After each iteration of the inversion the spatial norm $\mathcal{F}$ of the current model is calculated for all times and compared against "wanted" values. The "wanted" values $\mathcal{F}_w$ also correspond to the model complexity and is one of the following:

- a constant model complexity for the whole time period comparable to ARCH3k.1

- constant complexity for the time before 1600 and comparable to ARCH3k.1, from 1600 to 1980 complexity of gufm1, after 1980 again a constant complexity

The new λ_t for every iteration then gets calculated by looking at the percentage difference of the wanted and the current model complexity and adding this value to the damping value.

$$\lambda_{i+1} = \lambda_i + \lambda_i \left(\frac{\mathcal{F}}{\mathcal{F}_w} - 1 \right) \tag{3.14}$$
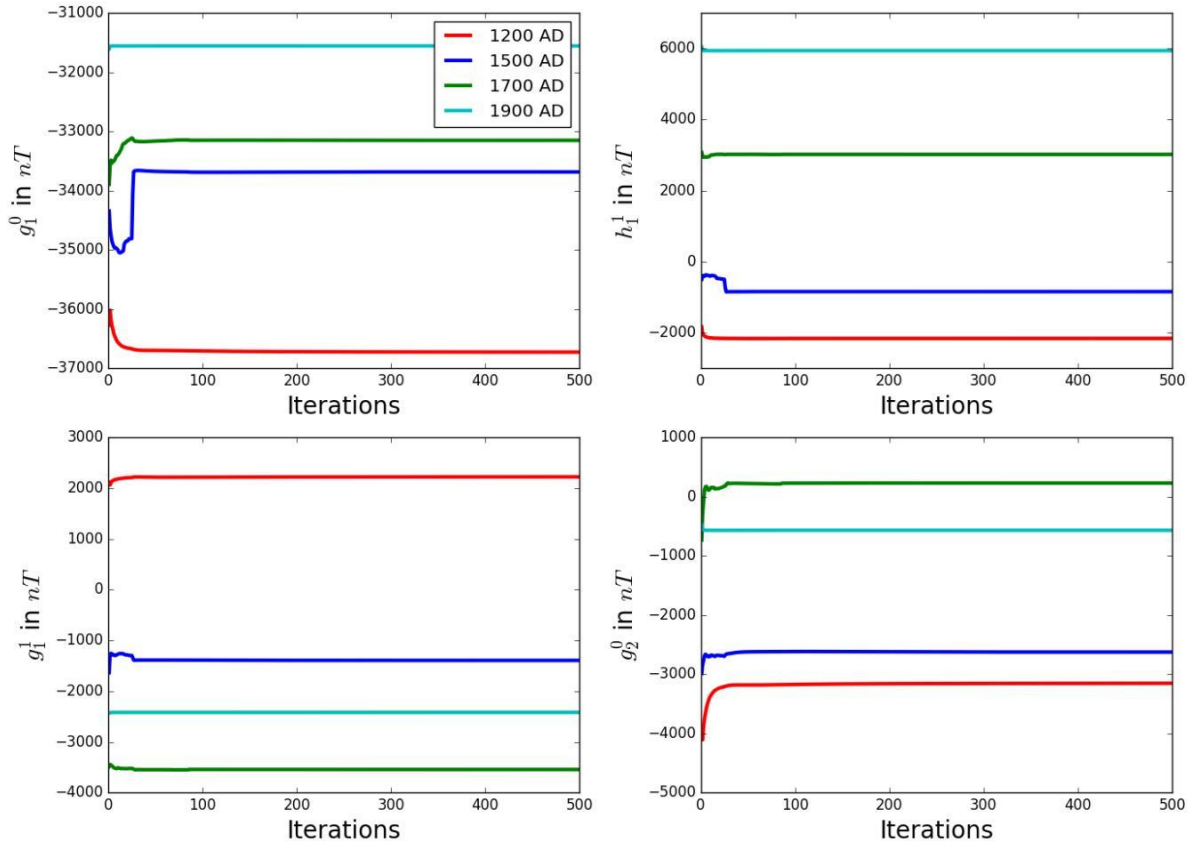
FIGURE 3.4: Convergence of the first 4 Gauss Coefficients at different times

By using that approach the model complexity can be easily controlled and is independent of the big changes in data coverage. Because this approach of determining $\vec{\lambda}$ is iterative, it is important to check if the the solution for the model vector $\vec{m}$ is still converging.

Figure 3.4 shows the first 4 Gauss coefficients for 4 different times as representatives for all coefficients from all times. It is apparent that quite a lot of iterations are needed to find a stable solution. Especially for the time period where historical data became available, that is around 1600 AD, the convergence is not very smooth and up to 60 iterations are needed to reach a stable solution. For further modelling the number of iterations is set to 100.

In figure 3.5 (right panel) the complexity of models for different choices of time-depended damping are shown. The brown line shows the complexity of a model which was done with a constant damping factor λ of $2 \cdot 10^{-13}$. As it becomes apparent, this leads to low complexity in earlier times but compared to gufm1 too high complexity in later times. The big increase of complexity coincides with the large increase of data count (left panel of Figure 3.5). A complexity higher than that of gufm1 is unwanted since our model over the historical time period is constrained using the almost the same data then gufm1.
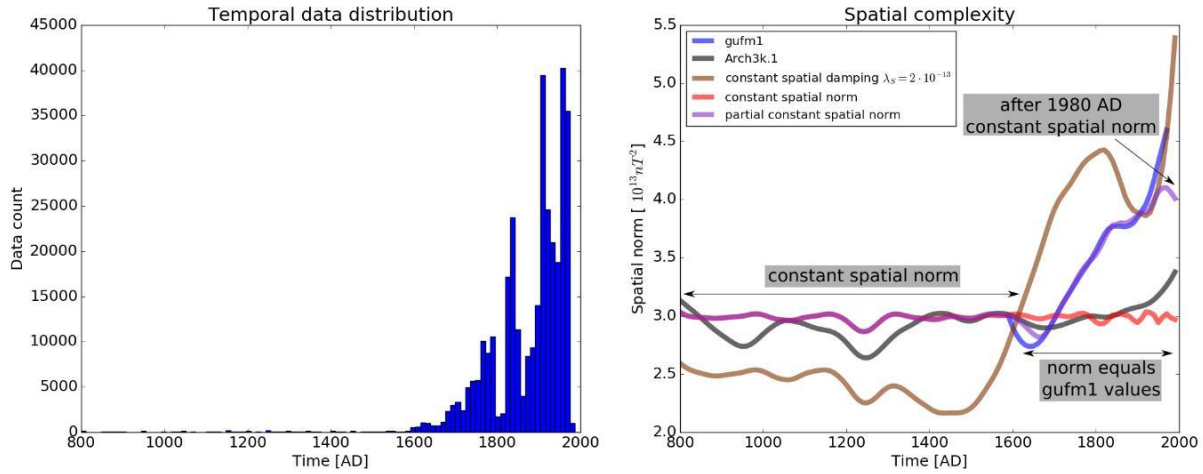
FIGURE 3.5: On the right side the spatial complexity for different choices of the time depended damping are plotted. Fur comparison the temporal data distribution is shown the left side.

The red line shows a model with a constant complexity over the whole time interval which was realized by choosing $\vec{\lambda}$ according to equation 3.14. It shows that constant complexity can be achieved even if the data coverage differs a lot during the chosen time interval. The constant complexity was chosen to be $3 \cdot 10^{13} nT^2$ which is approximately the value of Arch3k.1 (grey line).

However a constant complexity over the whole time interval is not ideal in the sense that it does not allow to make use of the higher information content of the data from 1600 to 1980. The violet line in figure 3.5 shows a model which adapts its complexity to be that of gufm1 (blue line) int the time interval between 1600 and 1980 and sets it to a constant value of $4 \cdot 10^{13} nT^2$ afterwards. This partial constant complexity was used to construct the final model which will be presented in chapter 5.

Chapter 4

Statistical analysis of archeomagnetic and volcanic data for global magnetic field modelling

The uncertainties of archeomagnetic and volcanic data are very important for global magnetic field modelling. The resulting model is very sensitive and dependent on these uncertainties. Unfortunately the uncertainties are not as well defined as needed for the purpose of modelling. The lack of sister samples sometimes leads to having no uncertainties at all, because its not possible to determine a useful deviation from a sample mean.

Even if a sufficient amount of samples is available and a standard deviation can be calculated, there still can be many additional systematic errors, which are not taken into account. The goal of this chapter is to infer consistent uncertainty estimates for data of all times by comparing test models to the existing historical field model gufm1.

4.1 Monte-Carlo-Simulation with random uncertainties

To find data weightings that lead to a model, which is similar to gufm1, 2000 models were calculated with randomly chosen uncertainties for every data point. These uncertainties were chosen from realistic intervals, so that the power spectrum of the model is comparable to already existing models. For intensity this interval is from 1000 to 10000 nT and for directional data it
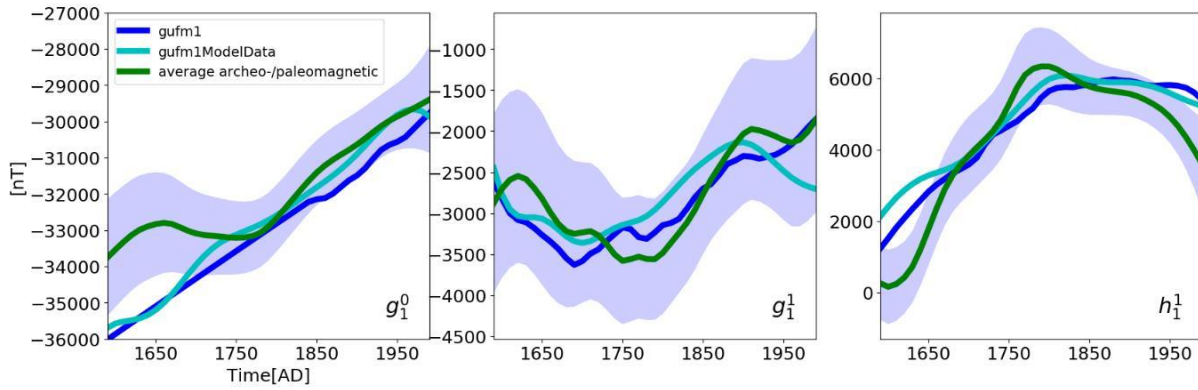
FIGURE 4.1: Average model and one standard deviation of the 2000 models compared to gufm1 and the test model created from synthetic data calculated with gufm1 at positions and times of archeomagnetic/volcanic database (see chapter 3.3).

is from 0.5 $^\circ$ to 5.0 $^\circ$ This also can be seen as a stability analysis of the modelling in terms of the uncertainties applied to the data. It should give an estimate which effect a bad data weighting can have on the model and which properties of the magnetic field are still preserved and hence can be interpreted in a physical sense. For comparison the test model in chapter 3.3 is used which allows to distinguish better between effects of spatial and temporal data distribution and the effect of the data itself.

In figure 4.1 the average and the standard deviation of all dipole coefficients are shown. For the g_1^0 coefficients it is clear that almost all models are shifted to lower absolute values, where the average model differs around 1000 nT from gufm1. This can be mostly attributed to the bad data distribution due to missing southern hemisphere data, because a similar trend can also be seen in the synthetic test model (cyan line). From 1750 AD backwards in time the calculated models don't show the linear decrease, which was extrapolated in gufm1. The origin of this difference lies within the data itself and not in the data distribution, because the synthetic model lies very close to the gufm1 extrapolation. While the g_1^1 coefficient seems to roughly agree with gufm1 the h_1^1 coefficient shows some bigger differences especially in the beginning and the end of the investigated time period (gufm1 time range).

4.2 Ranking the models by comparison to the gufm1 model

To get a quantitative ranking of the calculated models, a comparison for every single model to gufm1 was made. This comparison included only the dipole coefficients (equation 4.1) of the magnetic field, because the main target is to get a good estimate of the dipole moment evolution.
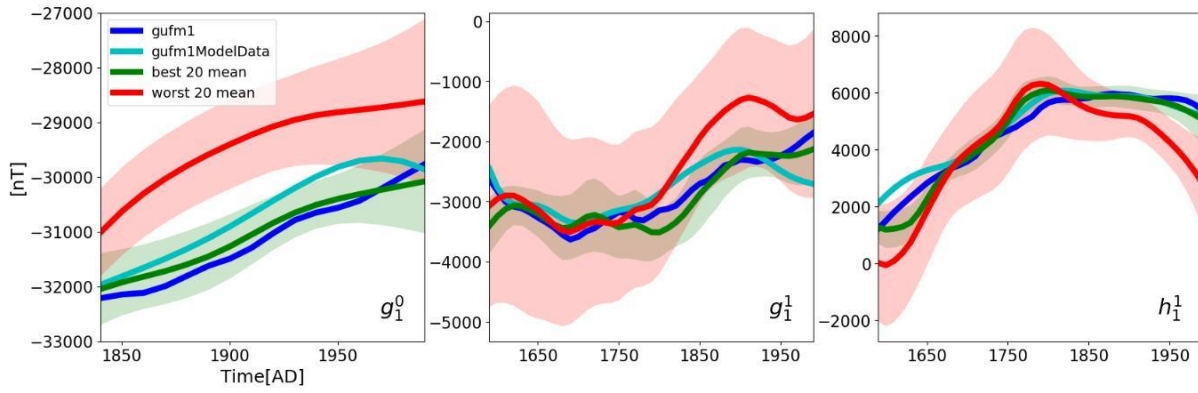
FIGURE 4.2: Average of best and worst ranked models according to equation 4.1 with one standard deviation.

As ranking tool the absolute difference of the model dipole coefficients to the gufm1 dipole coefficients is used. For the axial dipole coefficient only the values from 1840 AD and later are considered because at earlier times the gufm1 axial dipole coefficient is only a linear extrapolation. For the equatorial coefficients the whole time interval of gufm1 is used.

$$A_{di} = \sum_{t=1840}^{1990} |g^0_{1_{gufm1}} - g^0_1| + \sum_{t=1590}^{1990} \left(|g^1_{1_{gufm1}} - g^1_1| + |h^1_{1_{gufm1}} - h^1_1| \right) \tag{4.1}$$

Every model can be associated with a value A_{di} which makes it possible to look at the individual statistics of the good and bad models with respect to their similarity of the dipole coefficients to gufm1. Another rankings was calculated in which only on the axial dipole coefficient g^0_1 was used for calculation.

$$A_{axdi} = \sum_{t=1840}^{1990} |g^0_{1_{gufm1}} - g^0_1| \tag{4.2}$$

Dipole coefficients of best and worst ranked models according to equation 4.1 are plotted in figure 4.2. While the best models plot as expected very close to gufm1 the worst models have a g^0_1 coefficient which is strongly shifted to lower absolute values. It seems that certain data weightings strengthen the effect of a the bad data distribution that already leads to lower absolute values of g^0_1. The worst models also have a much higher standard deviation which is due to the missing constraint the be close to the gufm1 coefficients.
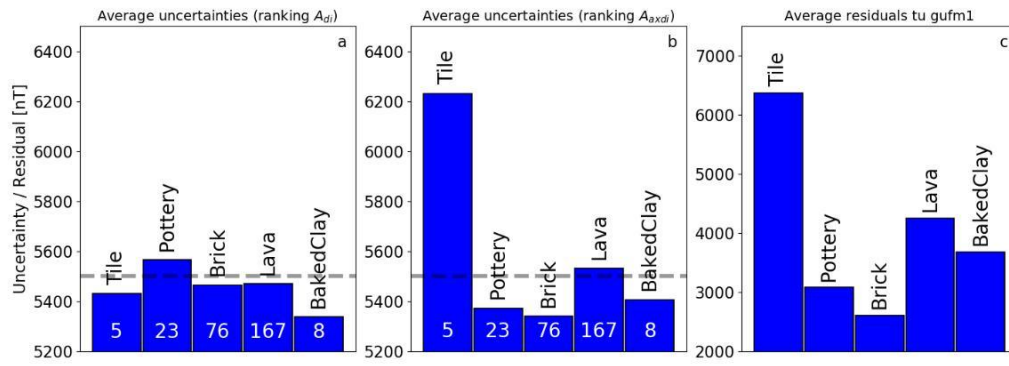
FIGURE 4.3: Average uncertainties of intensity data subsets grouped by different materials. Residuals of same subsets to gufm1.

4.3 Uncertainties of data subsets

Through the ranking system it is possible to determine for example the 20 highest ranked models. These model were all calculated with the same data set but different uncertainties, which were chosen at random for every individual model. The general assumption for the following investigation is that models, which score high in the ranking should have similar weightings for certain data subsets. Possible subsets to investigate are materials or methods, which were used in the experiments. Further subsets are cooling rate correction, anisotropy correction, method of dating or alteration monitoring. To validate the uncertainties or weightings for the individual subsets, residuals from the same subset to gufm1 were determined.

The intensity of the magnetic field is mostly determined by the axial dipole coefficient, which would suggest that models who have a low A_{axdi} give good uncertainty estimates for the paleointensities. To investigate this in detail the uncertainties of the two different rankings from material subsets were plotted in figure 4.3 in addition with the residuals to gufm1 of the same subset. It is clear that there are discrepancies between gufm1 residuals and uncertainties of the best 20 models of the dipole ranking A_{di}. The data from materials like brick or pottery seem to have higher uncertainties than volcanic data. Looking at the same subsets by the A_{axdi} ranking in figure 4.3 b the relative weighting of the data from the subsets of materials is in agreement with the residuals of gufm1 to the data subset. Hence for the analysis of all intensity data subsets the ranking is done by comparing A_{axdi} and for the directional data subsets A_{di}.

The averaged uncertainties extracted from the best 20 models of some important subsets and the average residuals to gufm1 are summarized in table 4.1. The materials baked clay, brick and

Subset	Intensity			Inclination			Declination		
Material	μ_m [nT]	μ_{gufm1} [nT]	N_d	μ_m [°]	μ_{gufm1} [°]	N_d	μ_m [°]	μ_{gufm1} [°]	N_d
Brick	5340	2608	76	2.7	3.4	204	2.6	1.9	1
Lava	5531	4254	167	2.8	3.7	253	2.8	3.9	248
Pottery	5372	3081	23	-	-	-	-	-	-
Baked Clay	5406	3678	8	2.7	3.5	40	2.7	3.5	30
Tile	6230	6370	5	-	-	-	-	-	-
Not specified	-	-	-	2.8	3.2	671	2.7	6.4	18
Methode	μ_m [nT]	μ_{gufm1} [nT]	N_d	μ_m [°]	μ_{gufm1} [°]	N_d	μ_m [°]	μ_{gufm1} [°]	N_d
Thellier-Thellier	5410	3230	87	-	-	-	-	-	-
Coe	5566	3747	55	-	-	-	-	-	-
Shaw	5496	3070	35	-	-	-	-	-	-
Aitken	5211	3628	9	-	-	-	-	-	-
Dating method	μ_m [nT]	μ_{gufm1} [nT]	N_d	μ_m [°]	μ_{gufm1} [°]	N_d	μ_m [°]	μ_{gufm1} [°]	N_d
Hist. dating	5469	3594	227	2.8	3.3	338	2.8	4.0	214
Other dating	5490	4240	64	2.7	3.3	942	2.8	4.9	195
Alteration	μ_m [nT]	μ_{gufm1} [nT]	N_d	μ_m [°]	μ_{gufm1} [°]	N_d	μ_m [°]	μ_{gufm1} [°]	N_d
Alteration check	5462	3428	116	-	-	-	-	-	-
No measurement	5498	4215	160	-	-	-	-	-	-
Anisotropy	μ_m [nT]	μ_{gufm1} [nT]	N_d	μ_m [°]	μ_{gufm1} [°]	N_d	μ_m [°]	μ_{gufm1} [°]	N_d
Anisotropy corr.	5398	3881	96	-	-	-	-	-	-
No measurement	5532	4181	163	-	-	-	-	-	-
Cooling rate	μ_m [nT]	μ_{gufm1} [nT]	N_d	μ_m [°]	μ_{gufm1} [°]	N_d	μ_m [°]	μ_{gufm1} [°]	N_d
Cooling rate corr.	5541	3935	30	-	-	-	-	-	-
No measurement	5481	3881	230	-	-	-	-	-	-

TABLE 4.1: Over 20 best models and a subset averaged uncertainties μ_m and average residuals to gufm1 μ_{gufm1}. N_d is the data count of the investigated subset.

pottery have the lowest uncertainties, while tile and lava have higher uncertainties attributed to them. For the directions it is not possible to see any big preference to weight data subsets stronger or weaker in the 20 best models. Also the residuals to gufm1 show that there is not much difference between the subsets with residuals between 3 and 4 degrees.

For the subsets that are representing different methods for the determination of paleointensity the Thellier-Thellier and the Aitken method show the lowest uncertainties. The Shaw method has relative high uncertainties even if the residuals to gufm1 are lower then for other methods.

Considering the dating methods of the samples no big difference are visible comparing historical dating to other methods with slightly higher intensity uncertainties for non historical dating.

The residuals to gufm1 show a preference of the historically dated samples which should be the most accurate dating method.

The check for alteration should be important for the reliability of paleointensities but the best ranked models show only slightly higher uncertainties for samples with no alteration checks. A direct comparison to gufm1 showed lower residuals for data which had accompanied alteration checks.

Data subsets with anisotropy corrections have lower uncertainties in the best ranked models than data with no correction which is in agreement with what the residuals to gufm1 show. Paleointensities corrected for cooling rate show higher uncertainties in the 20 best ranked models than data that was not corrected for cooling rate. The residuals to gufm1 show slightly higher residuals for data which was corrected for cooling rate.

4.4   Radial component at the core-mantle boundary

The radial component at the core-mantle boundary gives a lot of insight about the actual flow, that produces the earth magnetic field and determines its secular variation. To estimate, which features of a magnetic field model calculated from archeomagnetic and volcanic data are robust and can be possibly used to make physical interpretations, the radial component at the core-mantle boundary of gufm1 at 1950 and different outcomes of the statistical modelling are compared. Figure 4.4 c shows the model that was closest to gufm1 according to the criteria in equation 4.1. Four high latitude flux patches can be seen in the best ranked archeo-/paleomagnetic model and also the mid latitude flux patches over Africa. Reversed flux patches can clearly not be resolved in the archeo-/paleomagnetic models, but it is possible to estimate their location by the surrounding field structures. Calculated models are similar to gufm1 truncated at degree 4 in figure 4.4 b which indicates that this is the expected resolution of archeo-/paleomagnetic models. The average model in figure 4.4 d shows in general the same field structures as the best model with the high latitude flux patches shifted to lower latitudes. This result is very promising for modelling with archeomagnetic and volcanic data because the main large scale structures of gufm1 can also be found in these models. With the knowledge of their rough position and their movement, changes in the earth magnetic dipole can be explained and physically interpreted.
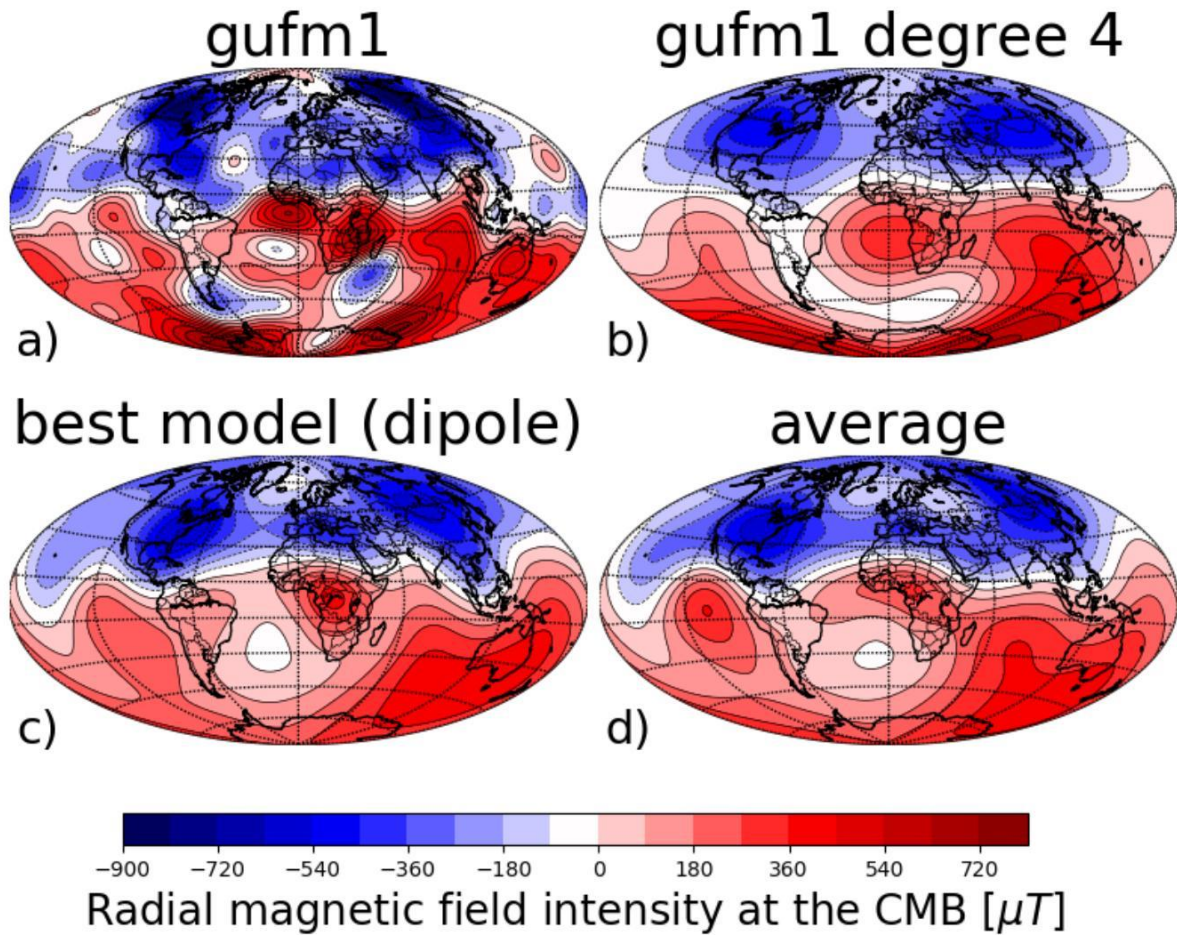
FIGURE 4.4: Radial component of the magnetic field at 1950 AD for the best model (according to equation 4.1) and the average model. For comparison the same is shown for gufm1 and gufm1 truncated at degree 4.

4.5 Statistics of rejected data

The modelling of the archeomagnetic and volcanic data included a rejection scheme that rejects data dependent on their residual to the model in the current iteration step. The threshold for the data rejection was set to 14000 nT for intensity, 12 ° for inclination and 14 ° for declination data. For the statistics a data point was only considered as rejected, when it was rejected in more then 1200 models out of the 2000.

With the chosen rejection thresholds around 7 percent of the intensity data was rejected, 5 percent of the declination data and 2 percent of the inclination data. One would suspect that intensity data has a higher probability of systematic errors, because of many conditions that have to be fulfilled to consider a paleointensity reliable. In table 4.2 the intensity data was separated in subsets dependent of material or method, which was used in the experiments

to investigate if certain materials or methods were rejected more often. Mainly volcanic and pottery/ceramic have a higher percentage of rejected data. Volcanic material is expected to have a higher rejection rate, because it usually alters quicker and the magnetic grains in slow cooling lava don't behave as single domain as the fast cooling pottery, which is the main condition for successful paleointensity estimations.

Another uncertainty is the age of the volcanic material, which can't be determined that well for older samples. It is surprising that pottery and ceramic samples were rejected that often. The comparison of the data that was not rejected in chapter 4.3 with the historical field did on the contrary show that this data has lower residuals. Out of the 4 most used methods no method seems to be particular more susceptible to be rejected.

It is also possible to divide the rejected data into subsets to investigate individual studies and determine if these studies might be unreliable, because a substantial part of their data was rejected. The definition of an unreliable study was chosen to be a study with more then 10 intensity results and if more than 10 percent of the data was rejected. One study with a high rejection percentage was from Games and Davey [1985] with 6 out of 21 results rejected. The material researched in this study was ceramic with only 1 tested specimen per result. Other studies were from Sternberg [1989] and Tulloch [1992], which were also pointed out as outliers in Suttie et al. [2011]. These two studies make up 18 out of the 39 rejected intensities for pottery/ceramic. This indicates that the high rejection rate of pottery/ceramic could also be attributed to other reasons, than just the material of the samples in this case.

In figure 4.5 the spatial distribution of the rejected data and the average number of models, which rejected data from that location is shown. It seems the data is mostly located in Greece, Britain, North America and Canary Islands.

4.6   Inferred estimation of uncertainties

To infer uncertainty estimates of archeomagnetic and volcanic data is not an easy task. Modelling with the given uncertainties from the authors leads to big differences in the dipole coefficients and also to probably much higher temporal variation of those (figure 4.6). The statistical analysis showed that uncertainties for intensity between 1000 and 10000 nT seem realistic and consistent with gufm1. In general the directions showed good agreement with gufm1 and can be considered more reliable.

Type	*Intensity data*		
Material	N_{rej}	N_{all}	N_{rej}/N_{all} [%]
Brick	21	494	4.3
Lava	34	386	8.8
Baked Clay	6	179	3.4
Pottery	30	318	9.4
Kiln	5	92	5.4
Ceramic	9	47	19.1
Tile	2	26	7.7
Methode	N_{rej}	N_{all}	N_{rej}/N_{all} [%]
Thellier and Thellier	60	862	7.0
Shaw	8	114	7.0
Aitken	2	74	2.7
Coe	19	289	6.6

TABLE 4.2: Rejected intensity data sorted by subsets. N_{rej} and N_{all} is the number of rejected data and the number of all the data of a certain subset.
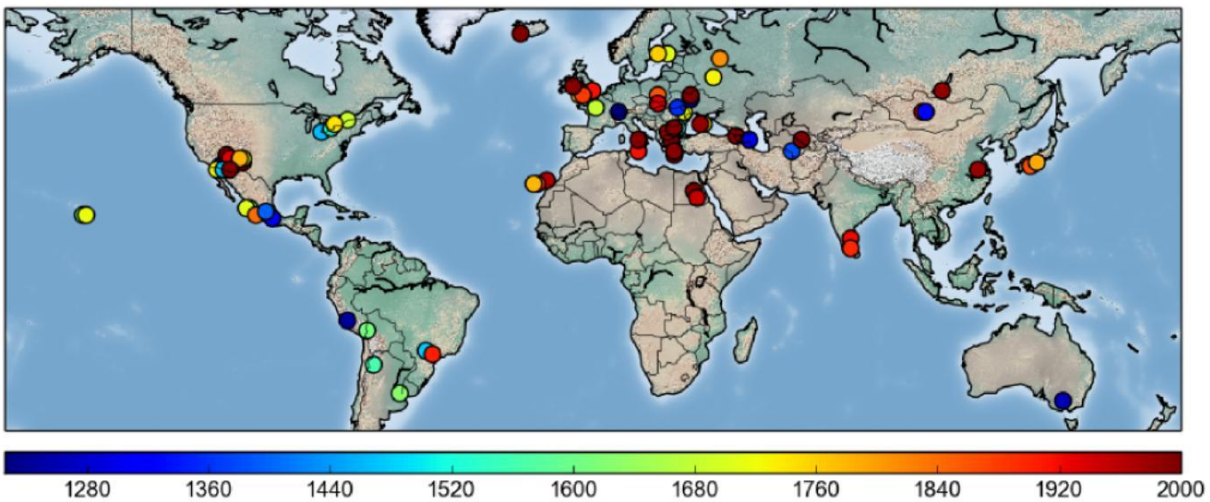
FIGURE 4.5: Spatial distribution of rejected intensity data with the rejection count (maximum is 2000 which would mean that data was rejected in all 2000 test models).

The statistics in chapter 4.3 show that certain subsets of data are more in agreement with the historical model gufm1 then other subsets. Especially the material should dictate the uncertainties of the paleointensity result, mainly contributed to magnetic grain sizes in the samples. The more the magnetic grains in a sample behave single-domain like the more reliable the result should be. Especially volcanic material, which might cool very slow during the acquisition of the TRM often contain big multi-domain grains, while man made material generally should have cooled much quicker.

How much uncertainty differences can be attributed the the choice of the method to determine
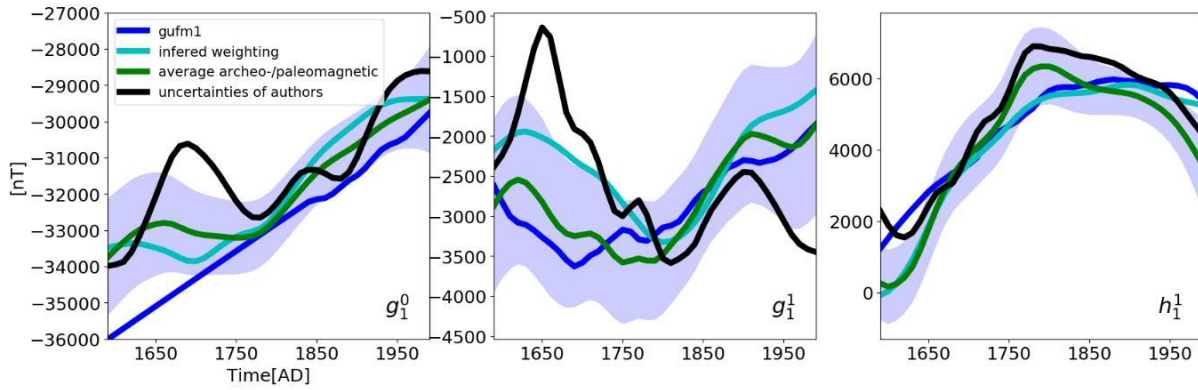
FIGURE 4.6: Gauss Coefficients of models with different initial weightings.

paleointensity was not clear from the analysis done here. The best models suggest that Thellier-Thellier seems to be the most reliable method. The residuals to gufm1 don't show big differences in the methods , which is the reason that weighting in further modelling is not done by method. This analysis unfortunately gives not much insight how much the dating method influences possible uncertainties because most of the investigated data is from recent times and could be dated historically. This allows no estimations for a possible weighting by dating method for earlier times.

The fact that alteration checks are done gives additional reliability to a result especially when chemical alteration can't directly be seen in the Arai plots. But if the Arai plot already show some curving behaviour at higher temperatures then the paleointensity result would have been rejected even without alteration checks. The degree of alteration is also highly dependent on the material. Anisotropy and cooling rate correction are also not considered the main uncertainty predicting properties because residuals to gufm1 only showed small differences.

Hence for further modelling the main influence from uncertainties of intensities will be attributed to the material of the samples, which were used in the experiments. In chapter 4.3 it was shown that baked clay, pottery and brick have the lowest residuals while lava and tile have the highest residuals to gufm1. For further modelling the uncertainties of baked clay, pottery and brick is set to 2000 nT and the uncertainty of lava and tile is set to 8000 nT to suppress possible unrealistic dipole moment behaviour. The uncertainty for other materials is set to 5000 nT. For declination and inclination the uncertainty was set to 3.5 °. Modelling archeomagnetic and volcanic data with these uncertainties leads to to purple model in figure 4.6, which is reasonable close to gufm1. Especially the h_1^1 coefficient gufm1 is very well reproduced in the recent years.

Chapter 5

1000 year global Earth magnetic field model from a combined database of archeo-/paleomagnetic and historical data

5.1 The final model - arhimag1k

In order to obtain uncertainties for the final model, I run a bootstrap inversion and obtain 501 models. Each inversion was based on a different input data set. The different input data sets have been constructed by considering that each data point is a Gaussian random variable, whose mean is the original value and whose standard deviation is its uncertainty. This algorithm resulted in a set of 501 different estimations for each of the Gauss coefficient. This set was used to compute the mean value of each coefficient and its standard deviation. The final model consists of these mean values which should be a reasonable model to describe the large scale features of Earth's magnetic field discussed in this chapter. Furthermore the statistical test in chapter 4 showed in spite of drastic variation of the data uncertainties, the models share in general, the same large scale magnetic features at approximately the same locations. The averaging gives a measure of uncertainty for the averaged model by means of the standard deviation of the Gauss coefficients.

5.2   Statistics of the models

To see how well the 501 models fit the data and different data subsets, normalized residuals for every model were calculated in the following way:

$$RMS = \sqrt{\sum_i \frac{1}{N} \left(\frac{(V_m^i - V_d^i)}{\delta V_d^i} \right)^2}$$
(5.1)

Here V_m^i is the calculated model value associated to the data value V_d^i at at the location and time of the data value. δV_d^i is the uncertainty of the data value.

Data subset	Data Type	Avg. Data Count	RMS
Average RMS from Data which was not rejected	All data	220494	1,47
	Intensity	58120	1,62
	Declination	86551	1,24
	Inclination	46919	1,47
	Horizontal Intensity	28904	1.74
Average RMS from all Data	All data	333694	3,69
	Intensity	58251	2,90
	Declination	195433	3,72
	Inclination	50470	5,00
	Horizontal Intensity	29540	1,86
Material Brick	All data	643	1,96
Material Lava	All data	657	1,21
Material Baked Clay	All data	491	1,62
Material Pottery	All data	229	2,26
Material Tile	All data	3	1,18
Material Other	All data	1908	1,25

TABLE 5.1: Relative residuals averaged over all models

Table 5.1 shows relatively high residuals for the data which includes all the rejected data. This has multiple reasons. For one the historical declination residuals at high latitudes are very sensitive to where exactly the pole lies in the associated model because there is a very high spatial gradient for the declination around the poles. The historical inclination residuals for earlier times are also quite high which can be also seen in the figure 2.13 in chapter 1. That only a small part of all the inclination values give high residuals can be seen in the low rejection count of 7 percent in contrary to the declination data where more than half of the data was rejected. This high rejection count can be attributed to the strict rejection criteria of having

a maximum absolute residual of 0.25 ° which was chosen to make use of the large number of historical directional data.

Very promising is that only around 100 intensity values were rejected which was one of the goals of the modelling to balance out the big difference in data count of directional and intensity data.

Looking at the residuals of the different materials and comparing it to the results of chapter 4 where a statistical test was made to discover which materials are more likely to give good results reveals that here brick, baked clay and pottery have the highest residuals. This is expected because there were artificially weighted higher then for example the lava data which has now relatively low residuals because it was weighted lower.

5.3   1000 year model compared to different archeomagnetic-/volcanic intensity data sets that went into the modelling

The following plots show how well intensity data from certain locations are fitted by different models. Especially the intensity data are of particular interest because the strength of the dipole moment is mainly determined by them.

Figure 5.1 shows the fit of a high quality data set of [Gallet et al., 2005] and [Genevey et al., 2009] with different models. All models capture the basic trend of this data set, but especially at 1600 and after 1700 AD they disagree with the data. Around 1600 the data shows an intensity peak which arhimag1k fits quite well. The model gufm1 also fits this peak well, even if it is not constrained by absolute intensity data before 1840. Arch3k.1 doesn't reproduce the peak suggested by the french data. The data after 1700 AD suggest a big decrease in intensity from approximately 50 μT to 43 μT in 50 years. None of the plotted models can reproduce such an extreme decrease in intensity. Nevertheless arhimag1k is the one that follows the intensity decrease closest and this is expected because the french data set was included in our inversion and one of the data subsets that was weighted higher due to the material of the archeomagnetic samples (see chapter 4).

Figure 5.2 shows one of the rare data sets that originate from the southern hemisphere ([Hartmann et al., 2010],[Hartmann et al., 2011]). arhimag1k fits this data well and also the other models capture the basic trend. In general the models show less secular variation in the southern hemisphere than in the northern hemisphere because of much less data and therefore much less

information about the magnetic field. The strong decrease of the magnetic field intensity after 1600 AD from 40 μT to 25 μT is also captured by all the models and mirrors the increasing strength of the South Atlantic Anomaly.

The same plot was done in figure 5.3 for the location of Hawaii and in particular for intensity data from two studies with volcanic material ([Teanby et al., 2002] in blue and [Laj et al., 2002] in red). All the data from Hawaii in general show a large dispersion and also have large uncertainties.

The models only reproduce the general trend of the data but estimate a much lower intensity than the data suggests. arhimag1k seems to fit this data the least, which is due to the low weighting for the volcanic data in the inversion (see chapter 4). The large discrepancy between the data point at 2000 AD and the models justifies our choice of weighting data based on volcanic material lower, since at this time the models should be a very good approximation to the true magnetic field.

arhimag1k seems to agree well with the data from very different regions, even if there are regions where only volcanic with high uncertainties or no data is available.
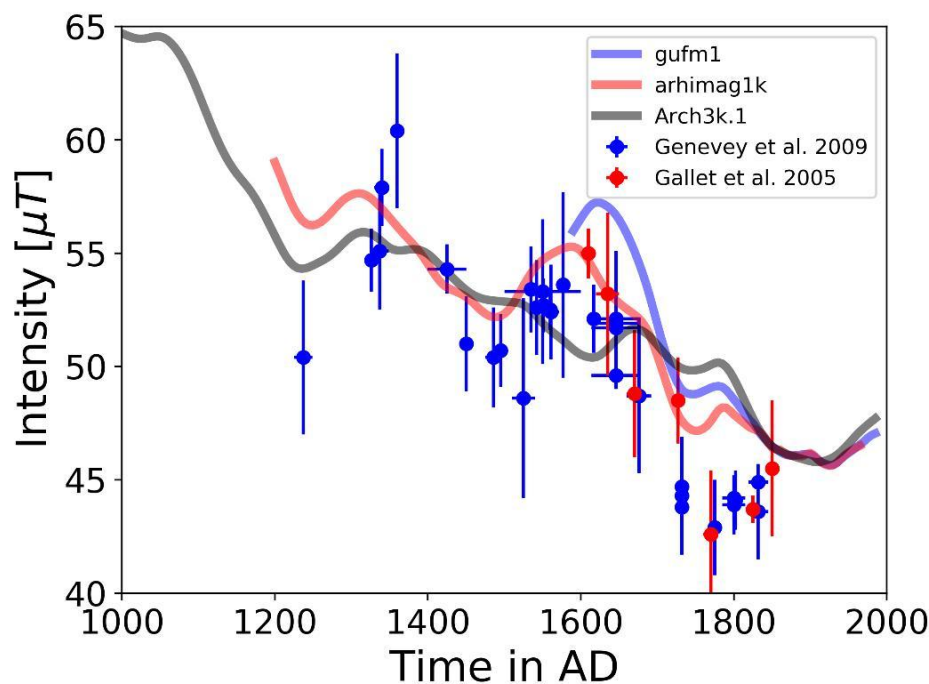
FIGURE 5.1: The models gufm1, ARch3k.1 and this study compared to high quality intensity data originated in France from [Genevey et al., 2009] (blue) and from [Gallet et al., 2005] (red). The model curves are calculated at a location of 48° N and 4° E.
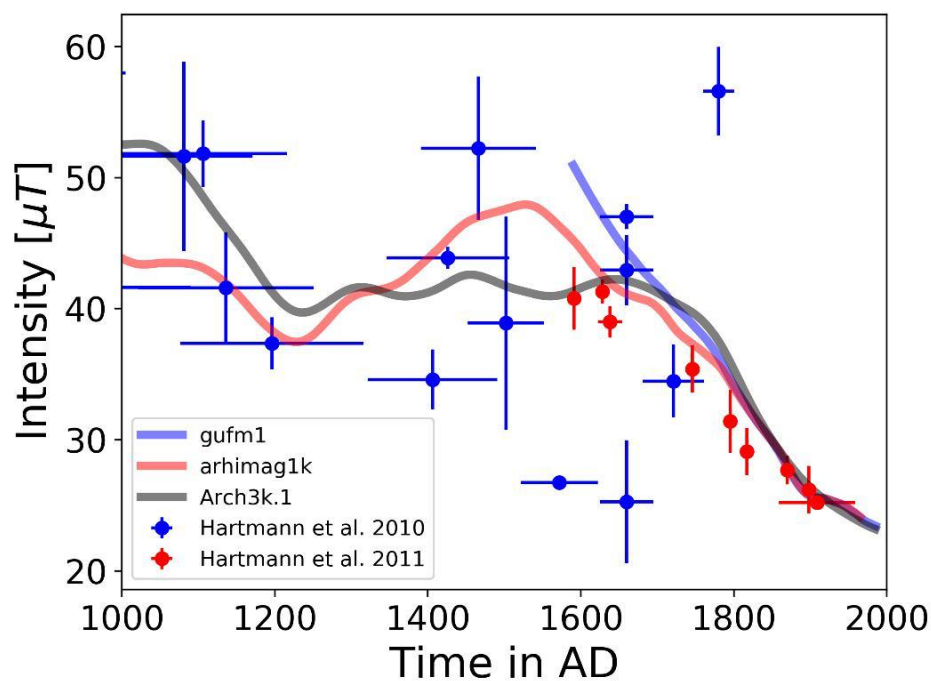
FIGURE 5.2: The models gufm1, ARch3k.1 and this study compared to intensity data originated in Brazil from [Hartmann et al., 2010] (blue) and from [Hartmann et al., 2011] (red). The model curves are calculated at a location of 23° S and 50° W.
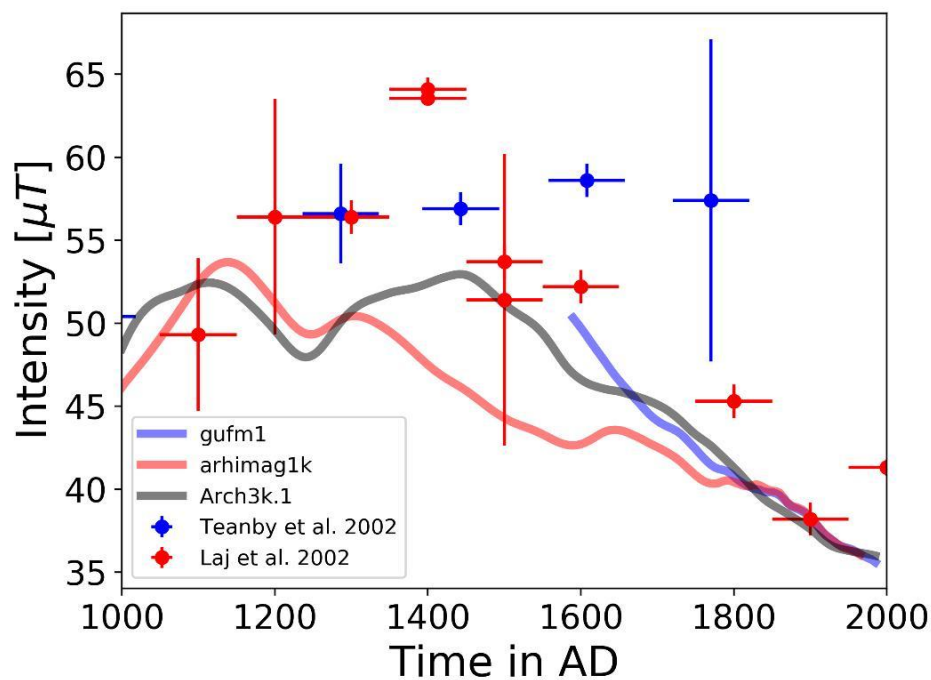
FIGURE 5.3: The models gufm1, ARch3k.1 and this study compared to intensity data originated in Hawaii from [Teanby et al., 2002] (blue) and from [Laj et al., 2002] (red). The model curves are calculated at a location of 20° N and 156° W.

5.4   1000 year model compared to independent data sets

To validate our 1000 years model independent data sets are needed. For this purpose, I use certain data sets from the database HISTMAG [Arneitz et al., 2017]. This database is a compilation of archeomagnetic and paleomagnetic data from GEOMAGIA50.v3 [Brown et al., 2015], the historical database compiled by Jonkers et al. [2003] and data from other sources, e.g. data from mining activities like adit directions, mining maps and other observations. Since these data have not been included in our inversion, they are suited to validate arhimag1k.

In figure 5.4 declination data from three mining areas are compared to arhimag1k at the respective locations. The change in declination over time of the 3 different locations in Europe is very well reproduced by the model. A further comparison between arhimag1k and an independent data set relies on declination data from sundials with attached compasses. Figure 5.5 shows declination values from two different locations compared to the 1000 year model at 11° N and 49° E. This data is much more inconsistent compared to the mining data but also is represented well by the model. [Arneitz et al., 2017] associated an uncertainty of 1.6° to the mining data and 4.3° to the sundial data.

Another independent data set from Hawaiian lava flows from Yamamoto and Yamaoka [2018] is shown in figure 5.6. This data set has very similar features to data which was already included in our inversion. It shows very large variation of the magnetic field intensity in time and also very large uncertainties. On average, the general trend of the data is well reproduced by arhimag1k. In particular, the more recent lava flows, which are well documented are fitted better than the older ones.
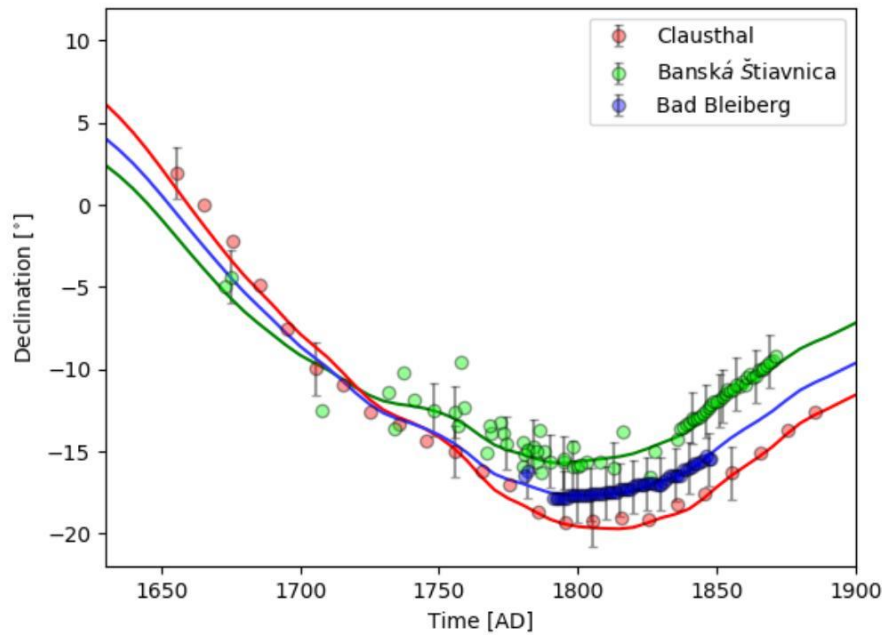
FIGURE 5.4: Declination data from three mining areas compared to the 1000 year model at the associated locations of the mining area. The uncertainty of all values is 1.6° and is plotted representative for every 5th data point.
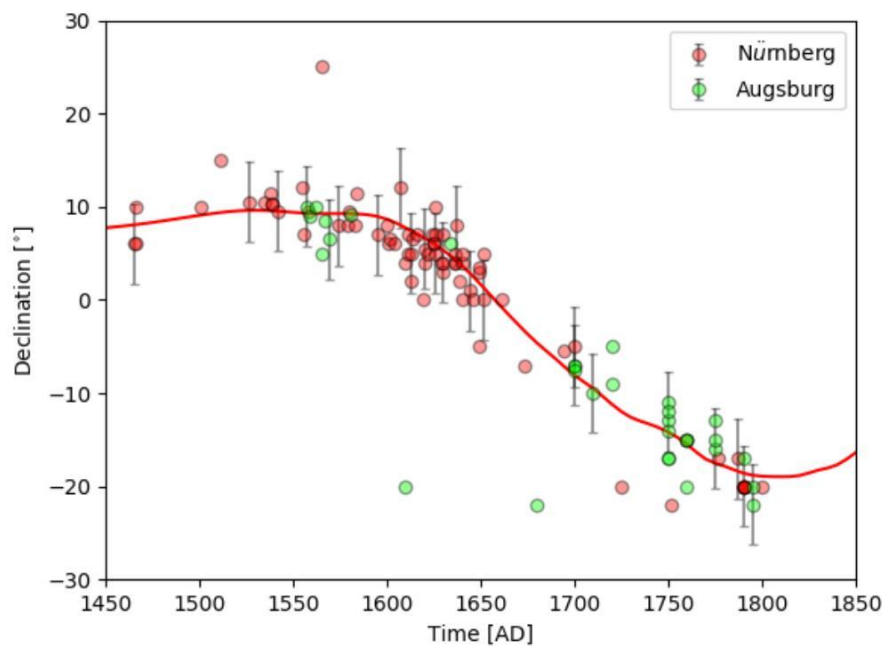
FIGURE 5.5: Declination data of sundials from two different locations. Model values are plotted for 11° N and 49° E. The uncertainty of all values is 4.3° and is plotted representative for every 5th data point.
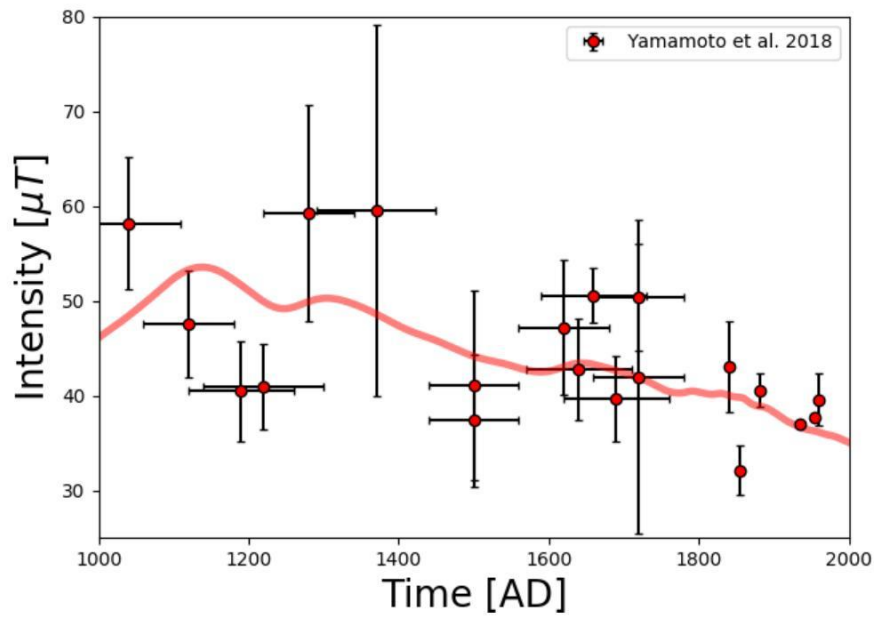
FIGURE 5.6: Hawaiian paleointensity data from lava flows [Yamamoto and Yamaoka, 2018]. The model curve is calculated at 19.5° N and 155° W

5.5 Geophysical interpretations of different features from the model

5.5.1 Snapshots of the field at different times
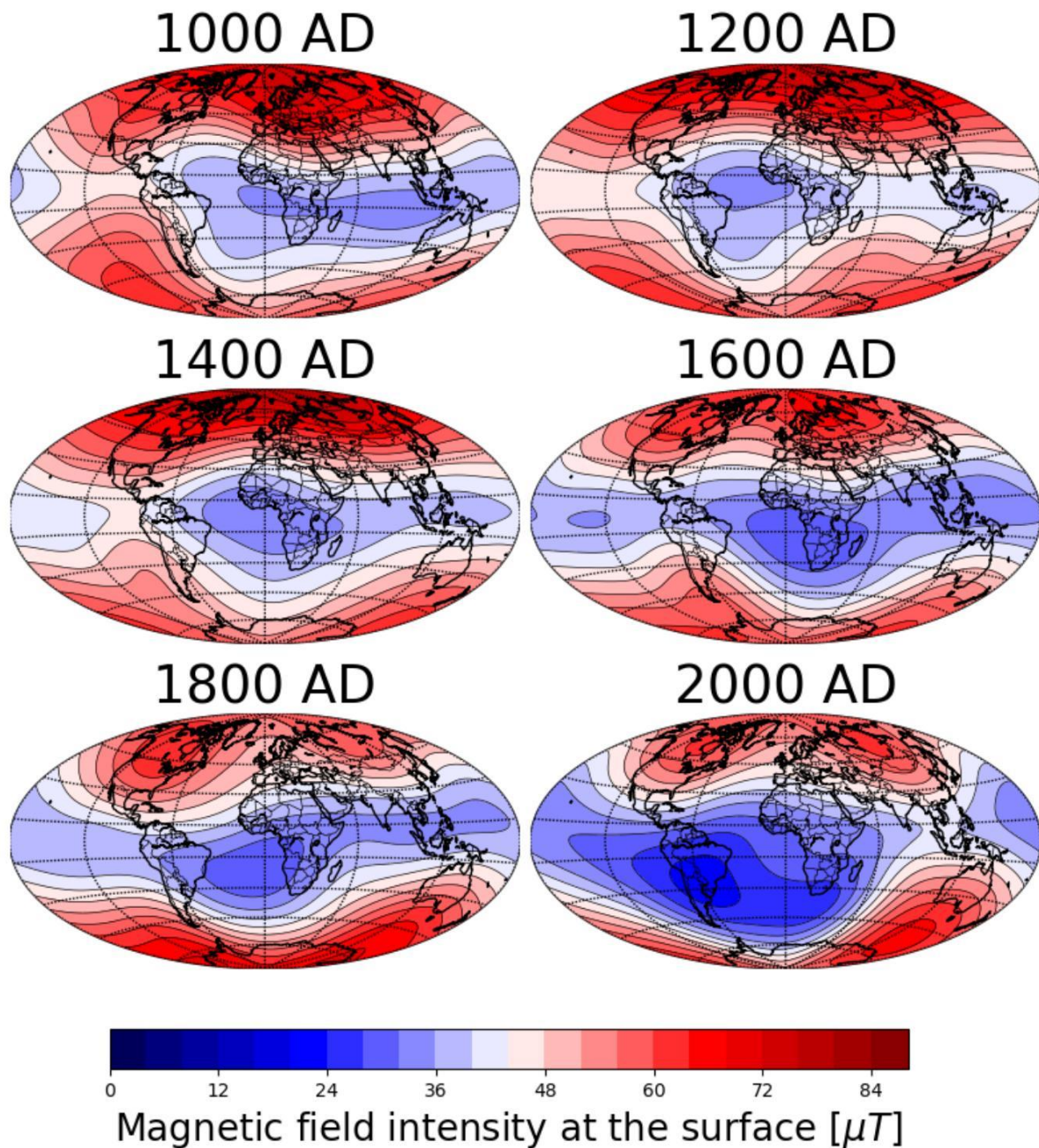
FIGURE 5.7: Snapshot at different times from the magnetic field intensity at the Earth surface.
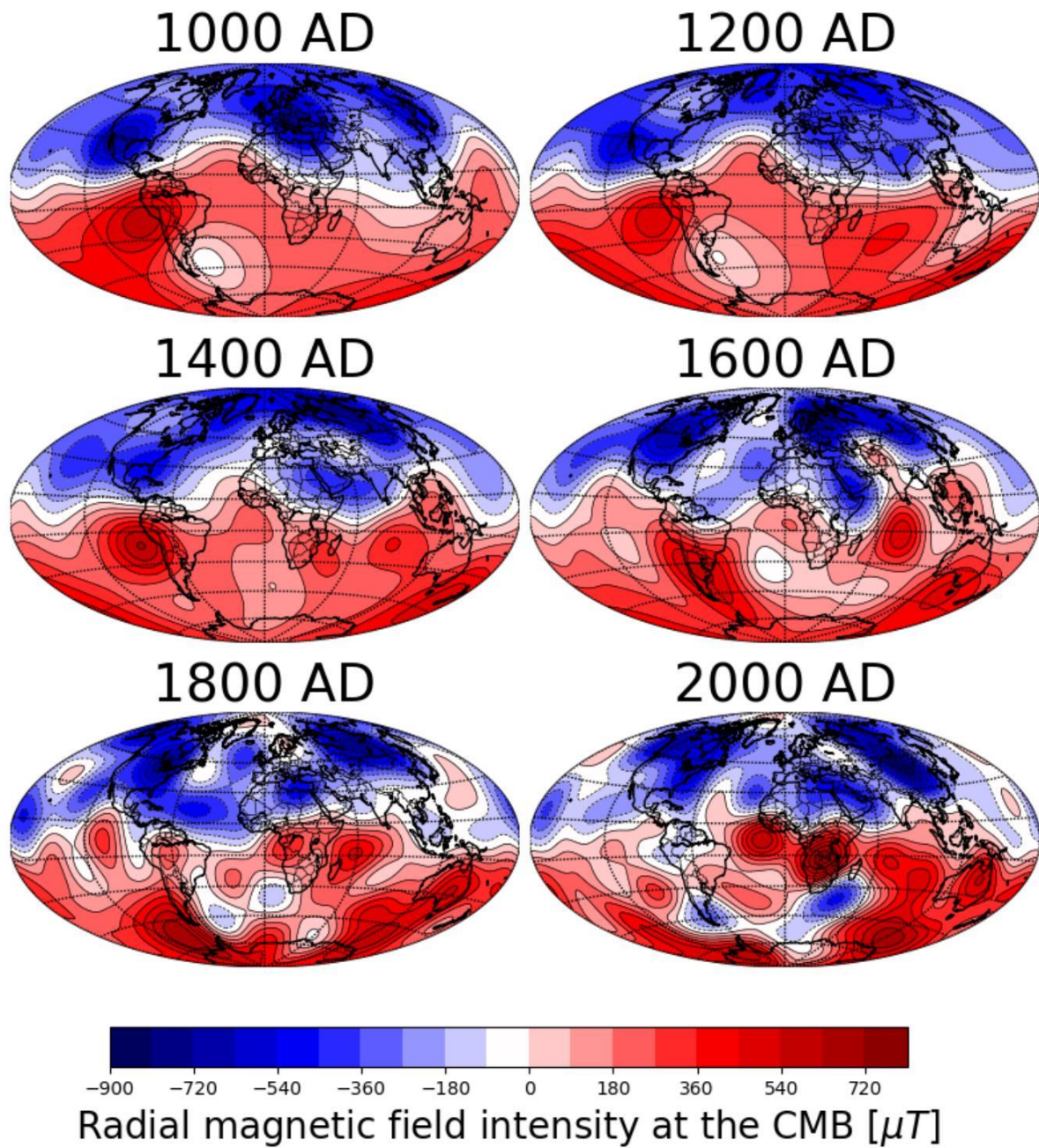
FIGURE 5.8: Snapshot at different times from the radial component of the magnetic field at the core-mantle boundary.

To investigate how the South Atlantic Anomaly evolved in the time before 1840 AD, snapshots of the magnetic field intensity at the Earth surface were made. Figure 5.7 shows how the area of low magnetic field intensity is very variable in time. At 1000 AD it is very spread over Africa and the Indian ocean, at 1200 AD it moved westwards over the Atlantic ocean and from 1200 AD to 1600 AD it drifted eastwards until it reached Africa again. The SAA as it is today seems to have moved from Africa westwards to its actual location over the last 400 years, while growing in size and area over the last 200 years.

Figure 5.8 shows the radial component of the magnetic field at the core-mantle boundary at different times. In general, more and more structures are visible the more we approach the present. This is due to a much better data distribution and data quality, mostly attributed to the historical data set.

From 1000 to 1200 AD a weak reversed patch can be observed over the South American area. It is roughly in the same area as the reversed flux patch today which causes the South Atlantic Anomaly. After 1200 AD this anomaly seems to disappear and it reappears at 1600 AD closer to Africa and then further moves westwards to the present location in 2000 AD.

Another structure which can be seen over the whole time period are flux patches at the mid latitudes, i.e. areas with a strong radial magnetic field component near the equator. These seem to be very dynamic both in terms of their position and their strength. From 1600 AD to the present, we see the expected westward movement of mid latitude flux patches over Africa. Before 1600 AD it is hard to determine any movement direction of these structures.

The structures which mostly influence the dipole strength and direction of Earth's magnetic field are the high-latitude flux patches. In general the main 4 flux patches (Eurasia, North America, south of South America and south of Australia) are roughly at the same positions at all times. However in the earlier years, from 1000 AD to 1600 AD, the period over which only archeomagnetic and volcanic data were used, it seems that, the position of these flux patches, especially in the southern hemisphere is not very apparent. Also, they are closer to the equator in earlier times which might be due to the scarcity of data from the southern hemisphere. Other than these main flux patches, the model shows additional flux patches which seem to disappear over time. At the beginning of the model, there is a high latitude flux patch over Europe, which vanishes until 1400 AD. 1200 AD shows a third flux patch in northern hemisphere, over Greenland, which disappears completely around 1600 AD.

5.5.2 Dipole moment of the last 1000 years

One of the main goals of this work is to research the evolution of the dipole moment over the last thousand years, without assuming any constraints for the g_0^1 Gauss Coefficient before 1840 AD. This was done by using archeo-/paleomagnetic data and historical data in the time interval of 1950 AD to 1990 AD.

Previous works came to very different conclusions which either suggest a linear decrease or a constant first Gauss Coefficient from 1590 AD to 1840 AD. Figure 5.9 shows the dipole coefficients and the dipole moment evolution according to arhimag1k. The results of previous works are shown in comparison.

This work suggests a more or less constant behaviour of the g_0^1 coefficient in the time between 1600 and 1800 AD (figure 5.9 a). That result is in agreement with the "most probable" model by Finlay [2008] and also agrees quite well for the g_0^1 coefficient with Gubbins [2006] from 1700 AD onwards, predicting a small decrease of 2.28 nT per year. The other two dipole coefficients g_1^1 and h_1^1 in panel b) and c) show almost the same evolution as the gufm1 model.

Figure 5.9 d) shows the dipole moments of the different models. The the dipole moments of Finlay [2008] and Gubbins [2006] were calculated by using the g_0^1 from the respective works and the other dipole coefficients g_1^1 and h_1^1 of gufm1.

arhimag1k shows a slight increase until 1700 AD and then a more or less constant evolution until 1840 AD. Panel e) of figure 5.9 shows the time averaged power spectra of gufm1 and this work. They are quite similar with the exception of degrees 5 to 10, which have more power for arhimag1k. This might be due to spectral leakage from even higher degrees because arhimag1k is truncated at degree 10, while gufm1 is truncated at degree 14.
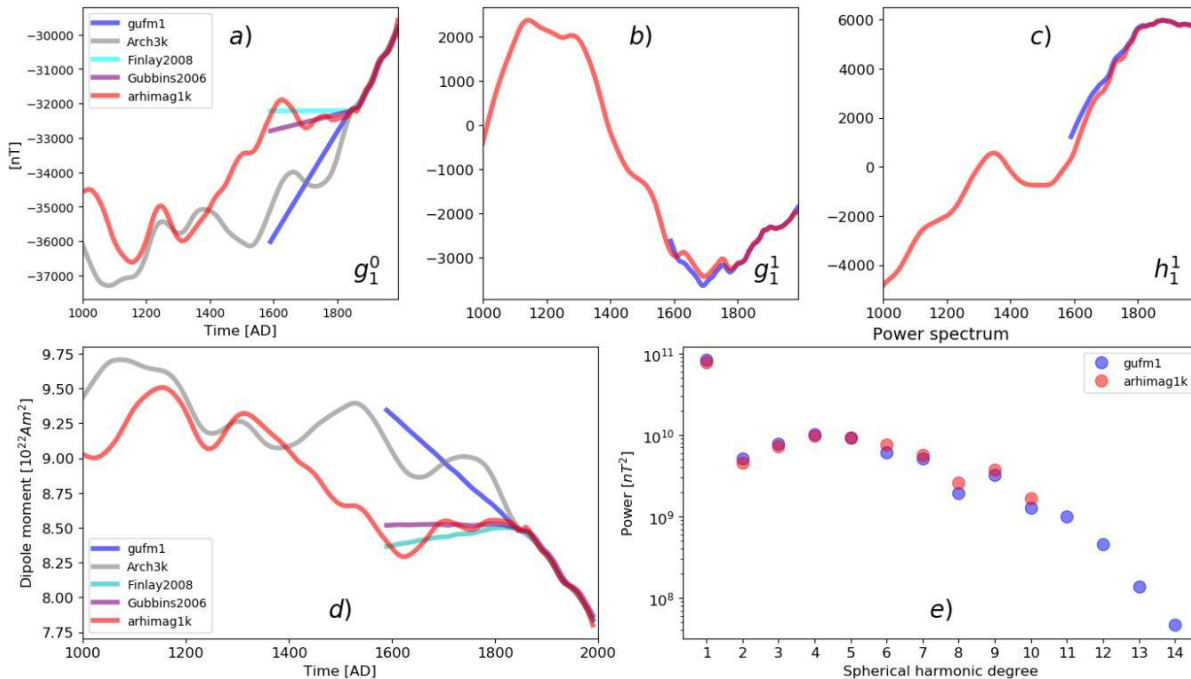
FIGURE 5.9: Panel a), b) and c) show the 3 first Gauss Coefficients of different models compared to this study (red line). Panel d) shows the dipole moment of the different results for g_0^1. Panel e) shows the time averaged power spectra of gufm1 (blue line) and this work.

5.5.3 Longitude time plots and westwards drift

We know that Earth's magnetic field over the Atlantic ocean and close to the equator has moved westwards in the last 100 years. To verify whether this behaviour is reproduced in arhimag1k and investigate the drift prior to this period, longitude time plots were calculated as described by Dumberry and Finlay [2007]. Using this graphical representation for the drift of field patches allows to visualize the west or east drift of certain flux patches at one specific latitude.

The first step of the calculation is to determine the time averaged axisymmetric part and remove this signal from the radial component of the magnetic field at the CMB for the whole time period. The next step is to generate a time series for every location, i. e., longitude and latitude. All periods longer than 400 years are filtered by a Butterworth filter. The resulting signal is then organized in a grid of longitude and time at a specific latitude.

Figure 5.10 shows the longitude-time plots at the latitudes $0°$ N and $30°$ N. Lower latitudes were not used to determine drift velocities due to the lack of a good resolution in the southern hemisphere, which did not allow to see clear drift patterns. In the last 300 years a clear westward drift in the Atlantic hemisphere can be seen at $0°$ N and at $30°$ N with slightly higher drift velocities of around $0.24 \ °/yr$ to $0.32 \ °/yr$ close to the equator. In Finlay [2003] the calculated drift velocity for these features was $0.27 \ °/yr$. Before 1650 AD no clear drift patterns can be seen at the equator.

At $30°$ N drifting patterns can be seen before 1650 AD. From 1100 AD to around 1450 AD there is a westward flux from around $60°$ east longitude to $0°$ with a drift speed of around $0.32 \ °/yr$.

From 1500 AD to around 1800 AD there is a relatively fast eastwards drift in the eastern hemisphere and a westwards drift in the western hemisphere. These two movements of magnetic features are simultaneous at the same latitude. This time also corresponds with a time of constant magnetic dipole moment in the 1000 year model.

From 1100 AD to 1400 AD there is a westwards drift of flux in the eastern hemisphere with a velocity of around $0.32 \ °/yr$.
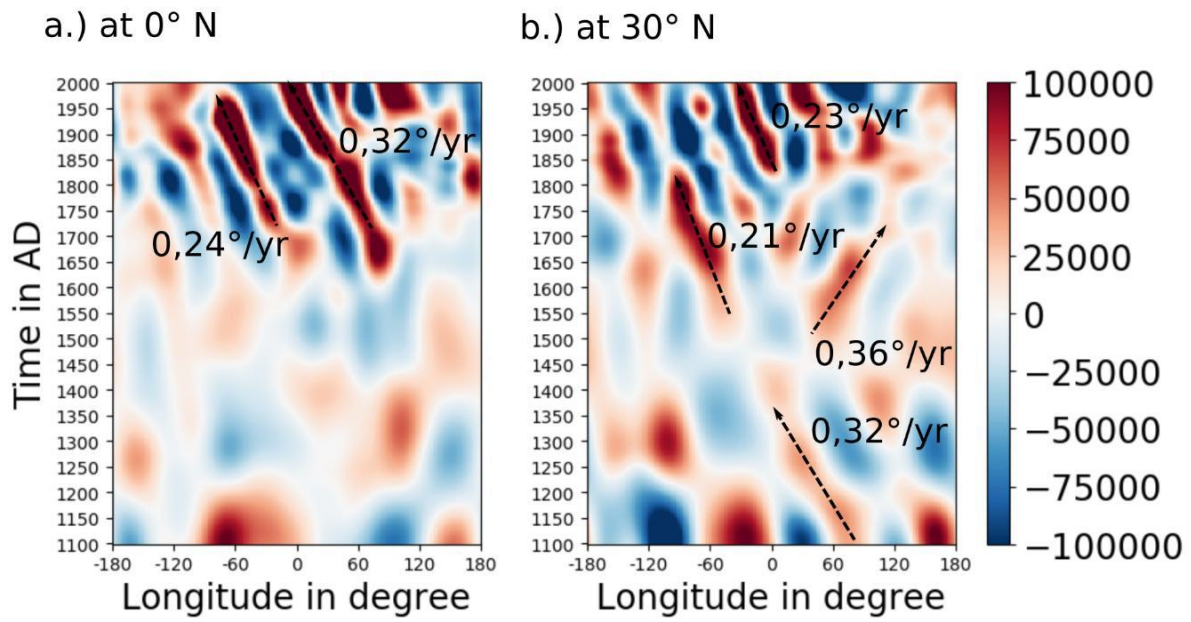
FIGURE 5.10: Longitude-time plot at a.) 0° N and b.) 30° N. Dashed lines are eyeball estimated time-longitude movements of specific flux patches. These lines were used to calculate the drift velocity of these flux patches.

Chapter 6

Lava flow samples of island Fogo from Cape Verde

This chapter presents new palaeointensity data from four historical lava flows on the island of Fogo, Cape Verde, approximately 700 km west of Senegal, Africa; a location on the northern periphery of the current SAA. The ages of the lavas were assigned previously through a combination of historical accounts and geological mapping and span 1662 to 1847 AD.

6.1   Sample sites

6 cores from the 1799 and 18 cores from the 1857 flow were taken at the site and magnetically oriented. Unoriented whole rock hand samples were taken from 1664, 1721, 1769, 1816, 1847 and 1852 flows. These blocks were then cored using a drill press at the GFZ Potsdam. The relative orientation of cores from the same block was maintained. Standard paleomagnetic cylinders which are 25mm in diameter and 22mm in height were cut from all the sampled material. Slices from the end of the core were removed and crushed to obtain small pieces which were used for rock magnetic analysis.

6.2   Basic introduction of paleomagnetism

This section will give a very short extract of how material can gain a magnetisation and how this magnetisation can be used to infer ancient Earth magnetic field values.
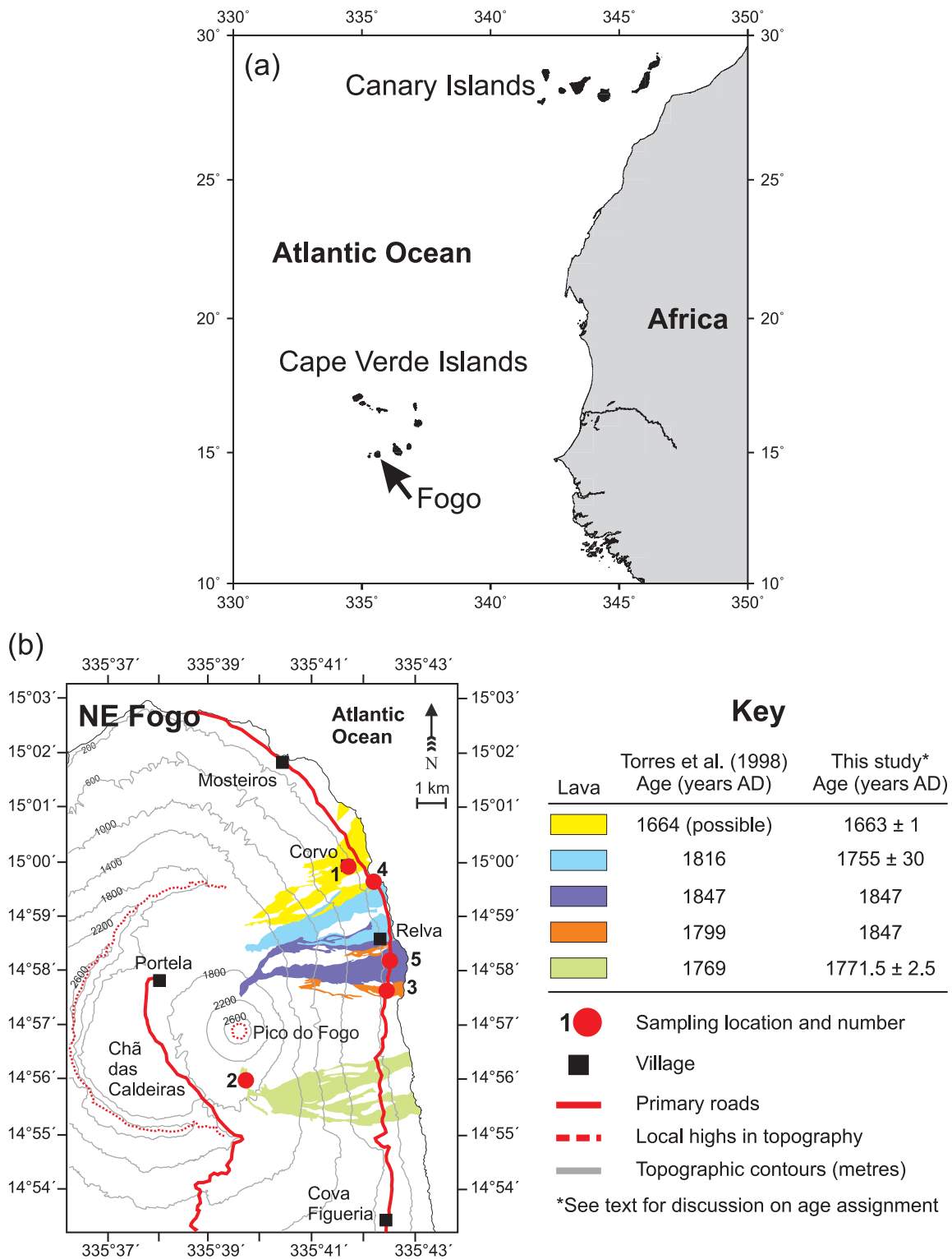
FIGURE 6.1: Sample sites and estimated ages of the sampled lava flows.

6.2.1 Different types of magnetisation in samples

By making use of the natural remanent magnetisation (NRM) of ferromagnetic samples it is possible under certain conditions to achieve good estimates of the ancient geomagnetic field. This NRM can originate from one or multiple overlapping scenarios which are described in detail in Butler [1991]. One source of the NRM is the thermoremanent magnetisation (TRM) which occurs if a ferromagnetic material is cooled from above the Curie temperature in the presence of a magnetic field. Another source is the chemical remanent magnetisation (CRM) where chemical changes lead to formation of ferromagnetic minerals below their blocking temperature while being in the presence of a magnetizing field. A third process is detrital remanent magnetisation (DRM) which is acquired during deposition of sedimentary rocks. Another process is viscous remanent magnetisation (VRM) which is gradually acquired while being exposed to weak magnetic fields. If a material was exposed to a very strong magnetizing field for a short period of time at a constant temperature, for example lightning striking close to the material, it is called isothermal remanent magnetisation (IRM).

6.2.2 Simplified model of TRM acquisition

In this work the focus will be on thermoremanent magnetisation because it is the main type of magnetisation in the samples studied here. A theoretical model behind that kind of magnetisation is that the magnetic moment of the single-domain ferromagnetic grains are either parallel or anti-parallel to the applied magnetic field (uni-axial anisotropy). This is a strong simplification because in reality one expects a random distribution along the easy axes of magnetisation. The energy difference between the two states in the theoretical model will lead to preferred occupation of the state with the magnetic moment $\vec{m}$ parallel to the applied field $\vec{H}$. The extend of aligning parallel with the magnetic field depends on the ratio b of aligning energy to thermal energy kT.

$$b = \left(\frac{\nu j_s H}{kT} \right) \tag{6.1}$$

Here ν is the volume of the grain and j_s is the saturation magnetisation and is a function of temperature. The alignment will diminish very quickly after removing the applied field if the temperature is bigger than the blocking temperature T_B. This temperature is defined as

the temperature at which the magnetic grains have a relaxation time above a critical value, which could be chosen as $\tau_c = 100s$ for laboratory experiments. Because the relaxation time is changing exponentially with decreasing temperature it reaches quickly geological time scales while going to lower temperatures. In an event where a ferromagnetic material gets heated above the Curie temperature and then cools down in the presence of a magnetic field, which in this case is the Earth magnetic field and reaches temperatures lower then the blocking temperature, the material will be left with a TRM. This TRM can be used to make inferences of the magnetic field which was present. For the simplistic model of uniaxial anisotropy mentioned before the TRM at the blocking temperature can be calculated as follows.

$$TRM(T_B) = N(T_B)\nu j_s(T_B) \tanh\left(\frac{\nu j_s(T_B)H}{kT_B}\right) \tag{6.2}$$

$N(T_B)$ is the number of SD grains per unit volume with blocking temperature T_B.

6.2.3   Rock magnetic experiments

Mineralogy experiments are very important to design and chose experimental methods to determine ancient magnetic field components. These experiments are generally categorized in three branches which are microscopy techniques, determination of Curie temperature T_C and coercivity spectrum analysis.

The Curie temperature can be estimated by heating and subsequent cooling of a sample in a strong magnetic field while monitoring the magnetisation or susceptibility of the sample. Points of major decrease in magnetisation or susceptibility are then interpreted as the Curie temperature. There are multiple mathematical methods to determine the Curie temperature from the resulting experimental curves. The knowledge of T_c helps determining the composition of ferromagnetic minerals in the samples by comparing it to values in the literature. This experiment also allows the detection of alteration or other possible effects with temperature if the heating and cooling curve are different. This information is especially important for paleomagnetic experiments, which include heating of the samples.

The coercivity analysis in this study consists of measuring hysteresis, backfield coercivity, IRM acquisition and FORC measurements. With the hysteresis curve which is determined by monitoring the induced magnetisation while changing the strength of the applied magnetic field.

After the magnetic field is reduced to zero its direction is changed and its strength is increased again in the other direction. An example hysteresis curve with the most important parameters is shown in figure 6.2 where M_s is the saturation magnetisation, M_{rs} is the remanence of the magnetisation and H_c is the coercivity.
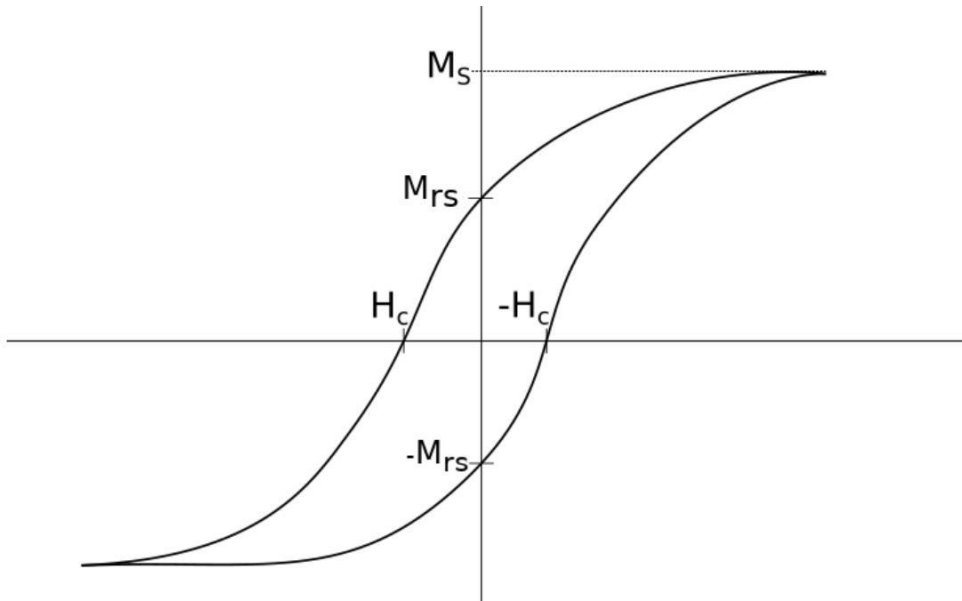
FIGURE 6.2: Drawing of an hysteresis curve with important parameters

6.2.4 Removing secondary component of the NRM

Initial thermal or alternating-field demagnetisation experiments on smaller specimens can be very helpful in revealing secondary NRM components in the sample and finding appropriate demagnetisation levels for additional experiments. By looking at the direction of the magnetisation and its change while demagnetizing the specimen, a rapid change in direction can often be observed for the first few demagnetizing steps until the direction stays stable for further steps. This allows demagnetisation of the samples and removal the secondary component in many cases. The secondary component in this case is mostly VRM and it points in the direction of the current Earth magnetic field.

In some cases it is very difficult to distinct the secondary component from the primary. If the sample was reheated above or close to the Curie temperature after the initial acquisition of the NRM in most cases it is impossible to determine the field components before the reheating. Also in case of strong IRMs i.e. from lightning strikes close to the sample it is often necessary to almost remove all of the magnetisation to be left with the primary component, which make estimation of the ancient direction and intensity of the Earth magnetic field very uncertain.

6.2.5   Determining the ancient field direction

After successfully removing the secondary component, the demagnetisation steps are continued until the Curie temperature is reached or until no NRM is remaining in the sample. A very common way to plot the resulting demagnetisation data which consists of three vector components from the magnetisation at every step on a two dimensional plane is the Zijderveld diagram [Zijderveld, 1967]. It allows the display of directional and intensity information in a single plot. Here the distance of each data point from the origin is proportional to the remaining intensity of the NRM. An example of a Zijderveld plot is shown in figure 6.3 which shows the magnetisation from an alternating field demagnetisation process of a specimen from the 1857 AD flow.
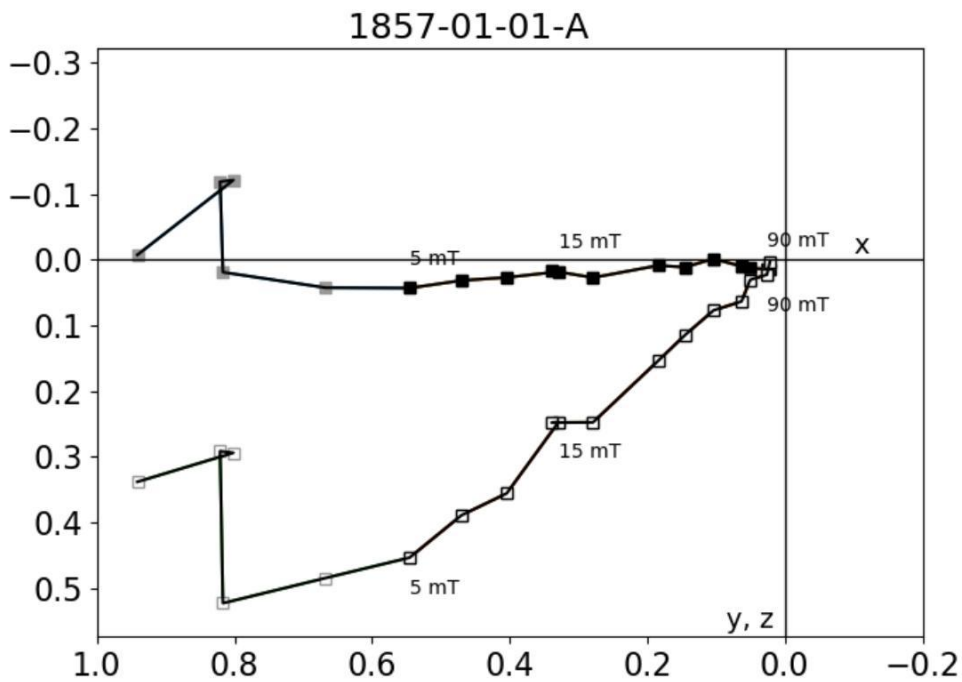
FIGURE 6.3: Zijderveld plot of an alternating field demagnetisation from a specimen of the 1857 AD flow. Open squares denote the projection in X-Z plane and closed squares the projection in the X-Y plane.

The paleomagnetic directions can be calculated by principle component analysis [Kirschvink, 1980]. The first step is to calculate the center of mass for all the vector components:

$$\overline{x} = \frac{1}{N} \sum_{i=1}^{N} x_i, \quad \overline{y} = \frac{1}{N} \sum_{i=1}^{N} y_i, \quad \overline{z} = \frac{1}{N} \sum_{i=1}^{N} z_i \tag{6.3}$$

The next step is the calculation of the co-variance matrix where the mean is subtracted from original vector components.

$$
\begin{bmatrix}
\sum (x_i - \overline{x})^2 & \sum (x_i - \overline{x})(y_i - \overline{y}) & \sum (x_i - \overline{x})(z_i - \overline{z}) \\
\sum (x_i - \overline{x})(y_i - \overline{y}) & \sum (y_i - \overline{y})^2 & \sum (y_i - \overline{y})(z_i - \overline{z}) \\
\sum (x_i - \overline{x})(z_i - \overline{z}) & \sum (y_i - \overline{y})(z_i - \overline{z}) & \sum (z_i - \overline{z})^2
\end{bmatrix} \tag{6.4}
$$

By solving for eigenvalues and eigenvectors one can find the characteristic axes which describe axes of lowest and highest variance in the data. The eigenvector $\vec{v}$ associated with the biggest eigenvalue λ is the desired direction. Declination D_{Pal} and inclination I_{Pal} can be calculated the following way:

$$
D_{Pal} = \tan^{-1}\left(\frac{v_y}{v_x}\right) \cdot \left(\frac{180}{\pi}\right), \quad I_{Pal} = \tan^{-1}\left(\frac{v_z}{\sqrt{v_x^2 + v_y^2}}\right) \cdot \left(\frac{180}{\pi}\right) \tag{6.5}
$$

A measure of uncertainty for the paleodirections is the maximum angular deviation (MAD). This quantity is calculated with the eigenvalues.

$$
MAD = \tan^{-1}\left(\frac{\sqrt{\lambda_1 + \lambda_2}}{\sqrt{\lambda_0}}\right) \cdot \left(\frac{\pi}{180}\right) \tag{6.6}
$$

6.2.6 Determining the ancient field intensity

There are different methods of paleointensity determination. Most of them consist of consecutive thermal demagnetisation steps where parts of the NRM are removed. Generally a demagnetisation step consists of two heating steps with one cooling in zero field and one cooling in a known lab field. The idea is that the ratio between the NRM which was produced by cooling in the ancient field H_{anc} and the TRM after cooling in present known lab field H_{lab} should be the same as the ratio of the two fields.

$$
\frac{H_{anc}}{H_{lab}} = \frac{NRM}{TRM} \tag{6.7}
$$

This relation is only true if the TRM is proportional to the field strength, which is in general the case for weak magnetic fields like the Earth magnetic field. If the magnetic field is small then $\tanh(b)$ is approximately b in equation 6.2, which shows the proportionality. Other conditions are that the acquired TRM in the lab field must completely replace the corresponding part of the NRM. Another condition is that the magnetic minerals and hence their ability to lock in an

NRM was not altered since the time the magnetisation was acquired and also that the NRM itself was not strongly altered.

The nature of these experiments also requires some additional conditions. It is important that there are no changes of the magnetic minerals during the experiment, like grain sizes or compositional changes, hence the ability of the sample to acquire TRM stays the same for all demagnetisation steps. Also the partial thermoremanent magnetisation (pTRM) acquired in one interval of heating should be independent of pTRM acquired in other intervals. To check if this condition is met additional steps which are called pTRM checks are often included. These are in field heating/cooling steps to lower temperatures to check if the same TRM is acquired as in the initial heating step to that temperature. If there is a big discrepancy, the sample significantly changes its ability to acquire TRM during the experiment and is not reliable for higher temperature steps.

If all these conditions are satisfied the plot of NRM remaining against pTRM acquired for every heating step should give a straight line where the slope m of this line is

$$m = \frac{H_{anc}}{H_{lab}} \tag{6.8}$$

To validate the success of a single experiment there is a big variety of statistical parameters. The following parameters were used in this work.

- $SCAT$: is a boolean value that determines if the scatter around the best fit line is in certain boundaries

- $DANG$: the angle between the best-fit line through NRM steps and the line anchoring the center of mass

- MAD: the maximum angular deviation or a measure of scatter around the best-fit line through the NRM steps

- Gap_{max}: the maximum value of the difference of the NRM of two consecutive demagnetisation steps normalized by the sum of all consecutive NRM differences of the experiment

- $FRAC$: the fraction of the original NRM used to estimate paleointensity

- $|k'|$: curvature of the Arai plot
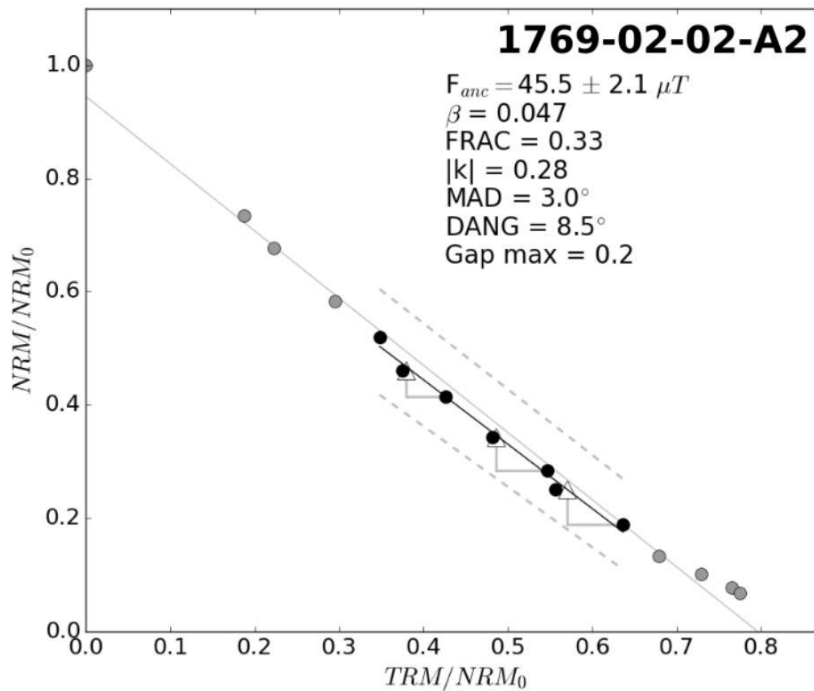
FIGURE 6.4: Sample Arai plot

- σ_m: standard error of the slope

- β: relative error of the slope m: $\beta = \frac{\sigma_m}{|m|}$

Figure 6.4 shows a an Arai plot from one of the measurements. The y axis shows NRM remaining normalized by the original NRM_0 in the sample and the x axis shows the TRM gained by the laboratory field also normalized by NRM_0. The black points were used to calculate the slope m which led to an ancient field strength of $45.5 \pm 2.1\,\mu T$ by using equation 6.8. The grey lines with the arrows denote the pTRM checks and the dashed grey lines show the boundaries for a successful SCAT test.

6.3 Rock magnetic experiments

To figure out which samples are more likely to lead to successful paleomagnetic experiments the following experiments were done. The temperature-dependence of magnetic susceptibility $\chi(T)$, hysteresis loops, back-field coercivity, isothermal remanence (IRM) acquisition and first-order reversal curves (FORCs) were measured at the Laboratory for Paleo- and Rock Magnetism, GeoForschungsZentrum (GFZ) Potsdam. All measurements were made on small chips of core material.

The $\chi(T)$ behaviour was measured with an AGICO MFK-1A Kappabridge with CS-3 furnace. Heating and cooling curves were measured between 20 $°C$ and 620 $°C$. The measurements were done in argon and in air because argon might suppress oxidation on heating and cooling allowing clearer identification of magnetic phases and estimation of Curie temperatures. Further it allows to discern between oxidation of titanomagnetite and inversion of titanomaghemite to magnetite. Heating and cooling in air will result in an increase in susceptibility on cooling for both. Heating in argon can suppress oxidation of titanomagnetite, which may otherwise oxidize to form a low-Ti magnetite with increased susceptibility and higher curie temperature on cooling. 15 experiments were done in air and 14 were done in argon. At least 2 specimens of every flow were measured either in air or in argon or both. To estimate the onset temperature of magnetomineralogical alteration in air, 9 specimens were progressively reheated to increasingly greater temperatures between 20 $°C$ and 620 $°C$ with an average step size of 50 $°C$.

The curie temperature of the magnetic carriers was estimated from the $\chi(T)$ curves. This was done by calculating the curvature (second derivative) of the curve and estimating temperatures of maximum curvature [Ade-Hall, 1974]. The accuracy of this method depends on the noise level and the chemical alteration in the experiment. Using a polynomial fit function by Bleil and Petersen [1982] then allows to make an estimation of $FeTiO_4$ content in the specimens.

Hysteresis, backfield coercivity, IRM acquisition and FORCs were measured on a Princeton Measurement Corporation MicroMag 2900 Series Alternating Gradient Magnetometer (AGM). FORCS were measured for at least one specimen of every flow and the other measurements were done for at least 4 specimens from every flow. In total 72 specimen were measured.

6.4 Paleomagnetic experiments

Paleomagnetic directions were determined at the Laboratory for Paleo- and Rock Magnetism, GFZ Potsdam by demagnetising the samples stepwise either by heating or an alternating magnetic field. 10 specimens of each oriented flow have been demagnetised, half of them by heating with a Magnetic Measurements Thermal Demagnetizer (MMTD18) and half of them by an alternating magnetic field with a Single-axis 2G Enterprises alternating field demagnetizer. This allows for a comparison of the results from both methods. The stepwise heating was done up to 520 $°C$ with a step size of around 50 $°C$ and the maximal strength of the alternating field

was 120 mT with a step size of around 10 mT. The remanence was measured after every de-magnetisation step with a AGICO JR6-A Spinnermagnetometer. To test for possible alteration of the heated samples, the susceptibility was measured with a Bartington Susceptometer MS2 after every heating step.

To determine the paleointensity the Tristan 14 GHz microwave palaeointensity system in the University of Liverpool Geomagnetism Laboratory was used. Prior to the actual experiments demagnetisation curves were measured for one specimen of every flow in order to estimated the power step sizes for the microwave experiment which avoids loosing a big part of the NRM in one step. Flows with a clear principle component, i.e. a stable direction while demagnetizing the sample, were then prioritized for paleointensity measurements, to achieve a higher success rate. The method used for the paleointensity was the modified version of the IZZI protocol [Tauxe and Staudigel, 2004] incorporating pTRM checks [Thellier and Thellier, 1959] to assess the amount of alteration occurring between heating steps. To accommodate pTRM checks the order of the infield (I) and zero-field (Z) steps was reversed so that a zero-field check preceded the pTRM check. Therefore the order of the steps was ZIIZP. The infield steps were done in a laboratory field of 40 μT. Different orientations to the NRM of the sample were tested in order to minimize multi domain effects of the magnetic grains. In total 35 paleointensity experiments were done.

6.5   Rock magnetic results

6.5.1   Susceptibility-temperature-behaviour

The behaviour of the specimens can be grouped into mainly four types, which are shown in figure 6.5. Type I specimens are dominated by one (type Ia) or two (type Ib) low-Curie temperature phases between 40 and 170 °C. Type Ia specimens mainly had only a very low temperature phase, which is an indicator for Ti-rich Ti-magnetite. Type Ib has two low temperature phases with the lower one being under 100 °C and the other one around the same curie temperature as Type Ia between 100 °C and 200 °C. Type II shows a more complicated behaviour. The specimens show two or three different phases, one low temperature phase from Ti-rich Ti-magnetite and either one or two higher temperature phases at around 400 °C for most likely Ti-poor Ti-magnetite and sometimes around 600 °C for a third phase possibly from magnetite

or maghemite. Type III shows one or two high temperature phases from magnetite and Ti-poor Ti-magnetite. Specimens of 1721, 1769, 1799, 1847 and 1852 can mostly be grouped into type I with only very low temperature phases. Only the 1664 and the 1857 flow have a more complex behaviour (type II and type III).

For the heating in argon type I susceptibility curves look reversible (figure 6.5). This reproducibility of $\chi(T)$ heating and cooling curves may suggest that such specimens might not undergo magnetomineraological alteration during thermal palaeointensity measurements. However, it has been noted previously (e.g.[Coe, 1967]; [Thellier, 1977]) that reversible susceptibility behaviour during heating and cooling may not be representative of the alteration of the remanence carriers. Therefore, reversible $\chi(T)$ behaviour may not result in reliable palaeointensity estimates. Type II curves are not reversible in an argon atmosphere. On cooling the intermediate magnetic phase disappears and only the low and the high temperature phases remain. Type III curves are also not reversible and have a lower susceptibility and lower curie temperature on cooling which might result from processes other then oxidation like homogenization of products from oxyexsolution or cation distribution changes through faster cooling ([Evans and Wayman, 1974], [Bowles et al., 2013]).

The heating to 620 $^{\circ}C$ in air showed no reversibility for all types of specimens (figure 6.6). Type I curves are reversible to a temperature of about 500 $^{\circ}C$, which followed from stepwise heating susceptibility experiments (figure 6.7). Heating to higher temperatures leads to a higher susceptibility on cooling due to oxidation. Type II and type III curves shows similar then in argon with the addition of possible oxidation processes.

The curie temperature of the magnetic carriers was estimated from the $\chi(T)$ curves (table 6.1). This was done by calculating the curvature (second derivative) of the curve and estimating temperatures of maximum curvature [Ade-Hall, 1974]. The accuracy of this method depends on the noise level and the chemical alteration in the experiment. Using a polynomial fit function by Bleil and Petersen [1982] then allows to make an estimation of $FeTiO_4$ content in the specimens. For the very low curie temperatures in Type Ib the titanomagnetite content is between 70% and 80%. The curie temperatures between 130 $^{\circ}C$ and 170 $^{\circ}C$ would indicate an titanomagnetite content of 60% to 70% which can be found in all types but type III. The higher curie temperatures range between 340 $^{\circ}C$ and 620 $^{\circ}C$ in which medium temperatures up to 500 $^{\circ}C$ have a titanomagnetite content of 10% to 40%. Because pure magnetite has a curie temperature around 580 $^{\circ}C$ the higher temperatures of over 600 $^{\circ}C$ would suggest a material with a slightly

FIGURE 6.5: Different types of $\chi(T)$ behaviour in argon. Dashed line is the cooling curve and the solid line is the heating curve.

higher Curie temperature like maghemite but due to a very low susceptibility at such high temperatures the curie temperature estimation might be not accurate and this phase could still be attributed to magnetite. Further it was noted by Fabian et al. [2013] that the methods of linear extrapolation or maximum curvature tend to result in too high estimates of T_C.

6.5.2 Hysteresis

In figure 6.8 some examples of hysteresis curves are shown. Especially the specimens of the 1721 flow differ quite strongly from each other with coercivities that vary over almost one magnitude (figure 6.8a, 6.8b). But also 1664 and 1816 specimens show exceptions of higher coercivity. Most of the specimens show a very low coercivity between $1\ mT$ to $7\ mT$ and resemble a wasp-wasted shape which indicates at least two magnetic components with strongly contrasting coercivities.
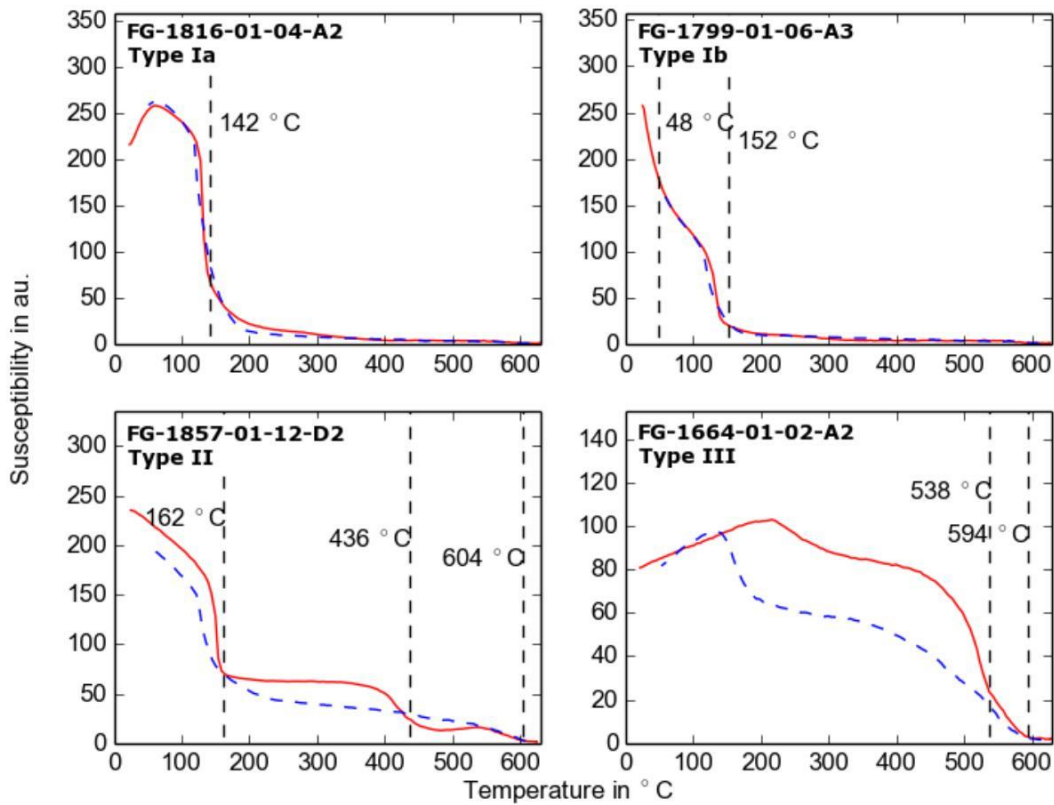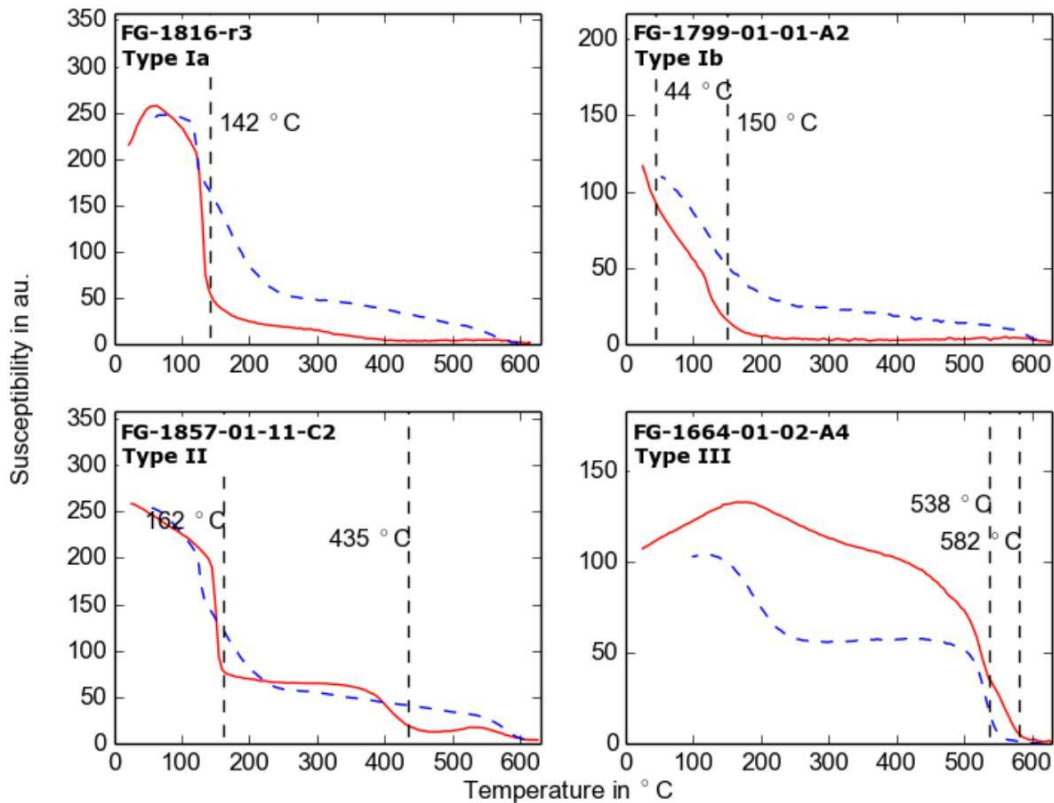
FIGURE 6.6: Different types of $\chi(T)$ behaviour in air. Dashed line is the cooling curve and the solid line is the heating curve.

In the Dayplot (figure 6.11, upper panel) it is apparent that the specimens have a big variety of magnetic grain sizes. The 1799, the 1852, the 1664 and the 1857 flow plot both in the PSD (MD+SD) and SD+SP ranges defined by Dunlop [2002]. The 1847, the 1816 and the 1769 flow plot well in the PSD range or have a mixture of MD and SD grains. The 1721/25 flow seems very inhomogeneous and plots over a big range from pseudo single domain to multi domain. The mixing curves (black solid lines) are defined for pure magnetite by Dunlop [2002]. This is the reason almost all specimens plot to the right of these lines because the magnetic carrier is titanomagnetite. The Squareness (M_{rs}/M_s) plotted over H_c in figure 6.11 (lower panel) shows two least-square linear regression lines for Ti-rich (60 percent titanium) samples and for Ti-poor magnetite or pure magnetite Wang and van der Voo [2004]. While most of the specimens cluster around the TM60 fit line at low coercivities, at higher coercivities the data flatten off and are more scattered. Distinctive is the 1664 flow which plots between the fits of Wang and van der Voo [2004]. This plot mostly underlines the results from the susceptibility measurements. The main carrier of magnetisation in our samples is Ti-rich Ti-magnetite, only for the 1664 flow it
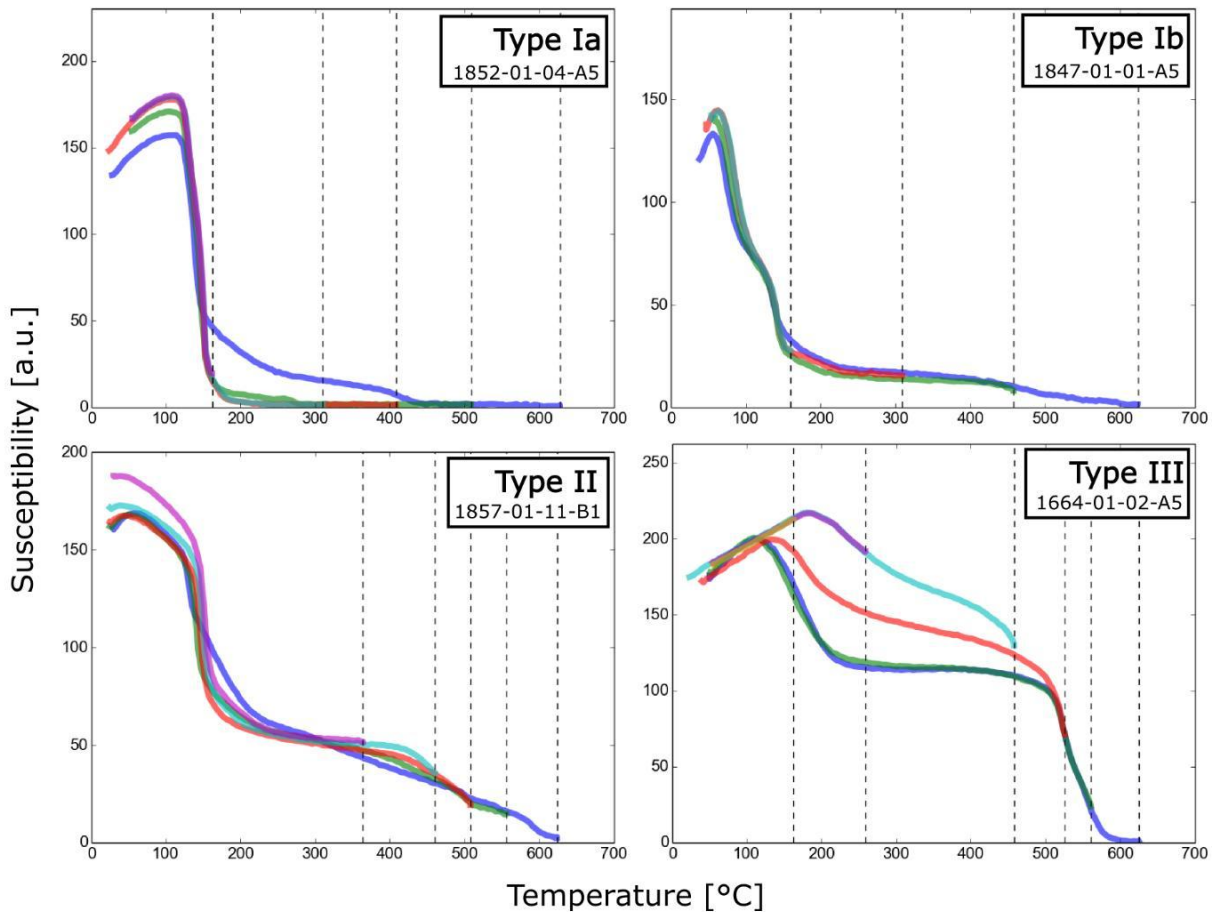
FIGURE 6.7: $\chi(T)$ behaviour in air for stepwise heating.

is Ti-poor Ti-magnetite.

FORC diagrams are shown in figure 6.9. For the 1664 specimen the diagram is unfortunately too noisy and probably doesn't contain much magnetic material. For 1721 there is a clear peak near the origin (SP particles) of the plot and one weaker peak around 10 mT which is probably due to SD titanomagnetite particles. The 1769 flow shows no clear SP component and again a peak most likely from SD titanomagnetite around $8mT$. Specimens of 1799, 1816, 1847, 1852 and 1857 have clear peaks at the origin from SP particles and probably an overlapping low coercivity component. All show only little vertical spread except 1847 which shows a bigger vertical spread indicative for MD particles.

IRM measurements and coercivity spectra are shown in figure 6.10. Most of the specimens were saturated at a field strength of $500mT$ and show a low coercivity component in the derivative of the IRMs except specimens of the 1664 flow. 2 of the tested specimens of 1664 have a very noisy IRM curve. They also produced the FORC diagrams that had almost no signal (Fig. 6.9, top left). 1721 has mostly peaks at lower field strengths but also some examples at higher field

sample	type	T_1 in $°C$	T_2 in $°C$	T_3 in $°C$	Atmosphere	Ti-content
1664-01-02-A4	III	538	582	-	air	TM06, magnetite
1664-01-02-A2	III	538	594	-	argon	TM06, magnetite
1721-01-05-A2	Ia	168	-	-	argon	TM61
1721-01-02-A4	Ia	159	-	-	air	TM62
1721-01-02-A5	Ia	159	-	-	air	TM62
1721-01-08-A5	Ia	163	-	-	air	TM62
1769-01-01-A4	Ia	138	-	-	air	TM65
1769-01-02-A5	Ia	129	-	-	air	TM66
1799-01-06-A3	Ib	60	157	-	argon	TM75, TM62
1799-01-01-A3	Ib	48	152	-	air	TM76, TM63
1799-01-01-A2	Ib	44	150	-	argon	TM77, TM63
1799-01-01-A4	Ib	46	133	-	air	TM77, TM66
1799-01-06-A2	Ib	44	145	-	argon	TM77, TM64
1799-01-06-A5	Ib	47	145	-	air	TM76, TM64
1816-r1	Ia	170	-	-	air	TM61
1816-r2	Ia	142	-	-	argon	TM64
1816-r3	Ia	142	-	-	air	TM64
1816-01-04-A2	Ia	142	-	-	argon	TM64
1847-01-01-A4	Ib	83	152	-	air	TM72, TM63
1847-01-01-A5	Ib	98	153	-	air	TM70, TM63
1847-01-02-A1	II	156	492	-	argon	TM63, TM14
1852-01-04-A6	Ia	164	-	-	air	TM62
1852-01-02-A2	Ia	136	-	-	argon	TM65
1857-01-05-A2	II	160	388	601	argon	TM62, TM30, magnetite/maghemite
1857-01-11-C2	II	162	435	-	air	TM62, TM23
1857-01-11-E2	II	160	379	615	argon	TM62, TM32, magnetite/maghemite
1857-01-12-B2	II	159	442	-	argon	TM62, TM22
1857-01-12-D2	II	162	436	604	argon	TM62, TM23, magnetite/maghemite
1857-01-18-C2	II	154	340	609	argon	TM63, TM37, magnetite/maghemite

TABLE 6.1: Assigned type for $\chi(T)$ behaviour, Curie temperatures of different magnetic phases and inferred/theoretical compositions of the samples. The composition was calculated with the polynomial fit function $T_c = -150x^2 - 580x + 851$ (Bleil and Petersen [1982]), where T_c is the curie temperature in K and x is the mole fraction of the ulvöspinel end-member $FeTiO_4$

values which is also visible in the FORC diagram and the big spread of that flow in the Dayplot. All specimens of 1769 show the same low coercivity peak and one specimen additionally shows a peak at a higher field strength. 1799 specimens give a very noisy signal and seem to have mostly two components. 1816 has the IRM curves with the clearest signal and peak mostly at low field values and one at a higher field strength. 1847 shows noisy signals and has peaks at very different field strengths. 1852 has the most noisy IRM curves and is therefore hard to interpret. Reason is most likely that the specimen only contained very few magnetic material. The 1857 coercivity spectra look similar to 1799 but also include a peak at even higher field values.
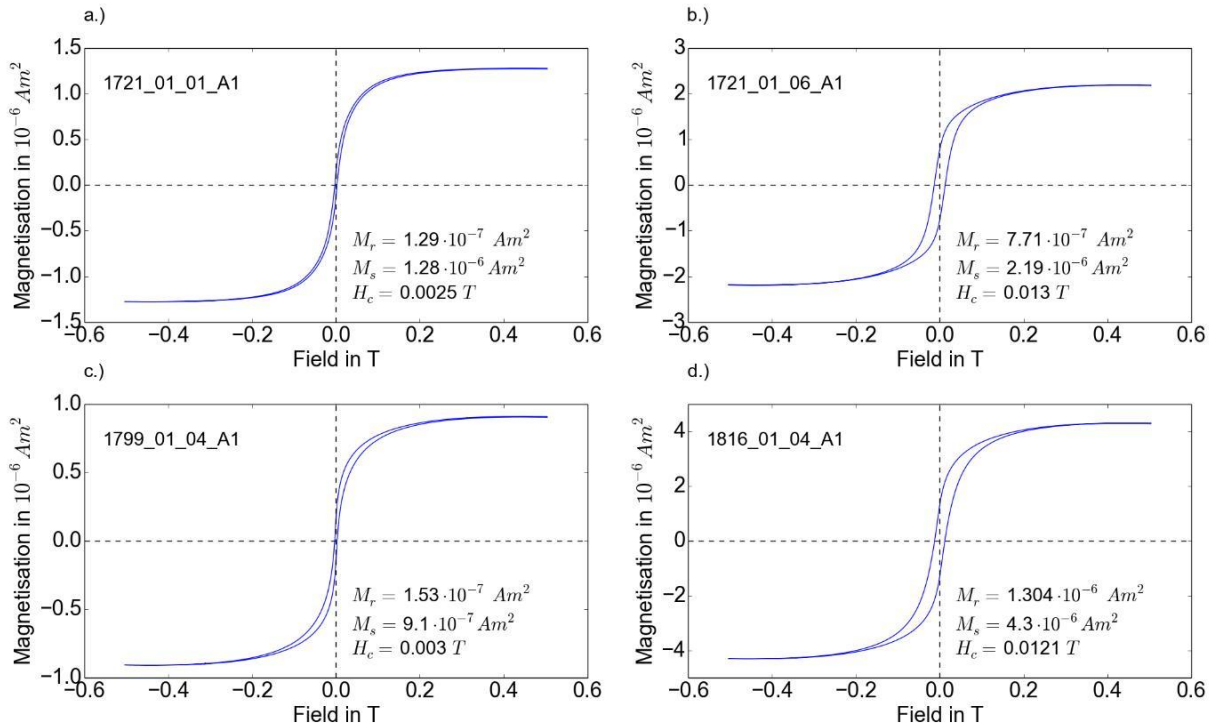
FIGURE 6.8: Representative hysteresis curves. M_{rs} is the remanence, M_s is the saturation magnetisation and H_c is the coercivity. (a)-(b) Hysteresis curves of the 1721 flow showing a difference in coercivity of almost one order of magnitude. (c) Wasp-waisted hysteresis curve from the 1799 flow, which points to at least two very different grain sizes. (d) Example from the 1816 flow with relatively high coercivity and slightly wasp-waisted shape.

6.6 Paleomagnetic results

6.6.1 Paleomagnetic directions

The specimens of the only flows that were oriented 1799 and 1857 had mostly two components, but the secondary component was removed with an alternating field (AF) of 5 mT or heating to 90 °C (figure 6.14). The specimens in the left part of figure 6.14 were demagnetised by an AF and the specimens on the right part were thermally (TH) demagnetised. Demagnetisation with an AF shows an exponential decay of the magnetisation (left side, lower panel Fig. 6.14) while thermally demagnetisation is irregular and similar to the $\chi(T)$ curves. The susceptibility stays approximately constant until the specimen was heated to a temperature between 300 and 400 degree which indicates alteration.

The direction of the characteristic remanent magnetisation was determined with the principle component analysis ([Kirschvink, 1980]). Directional results from the same core were averaged. Maximum angular deviation (MAD) values are between 2° to around 4° which are reasonable
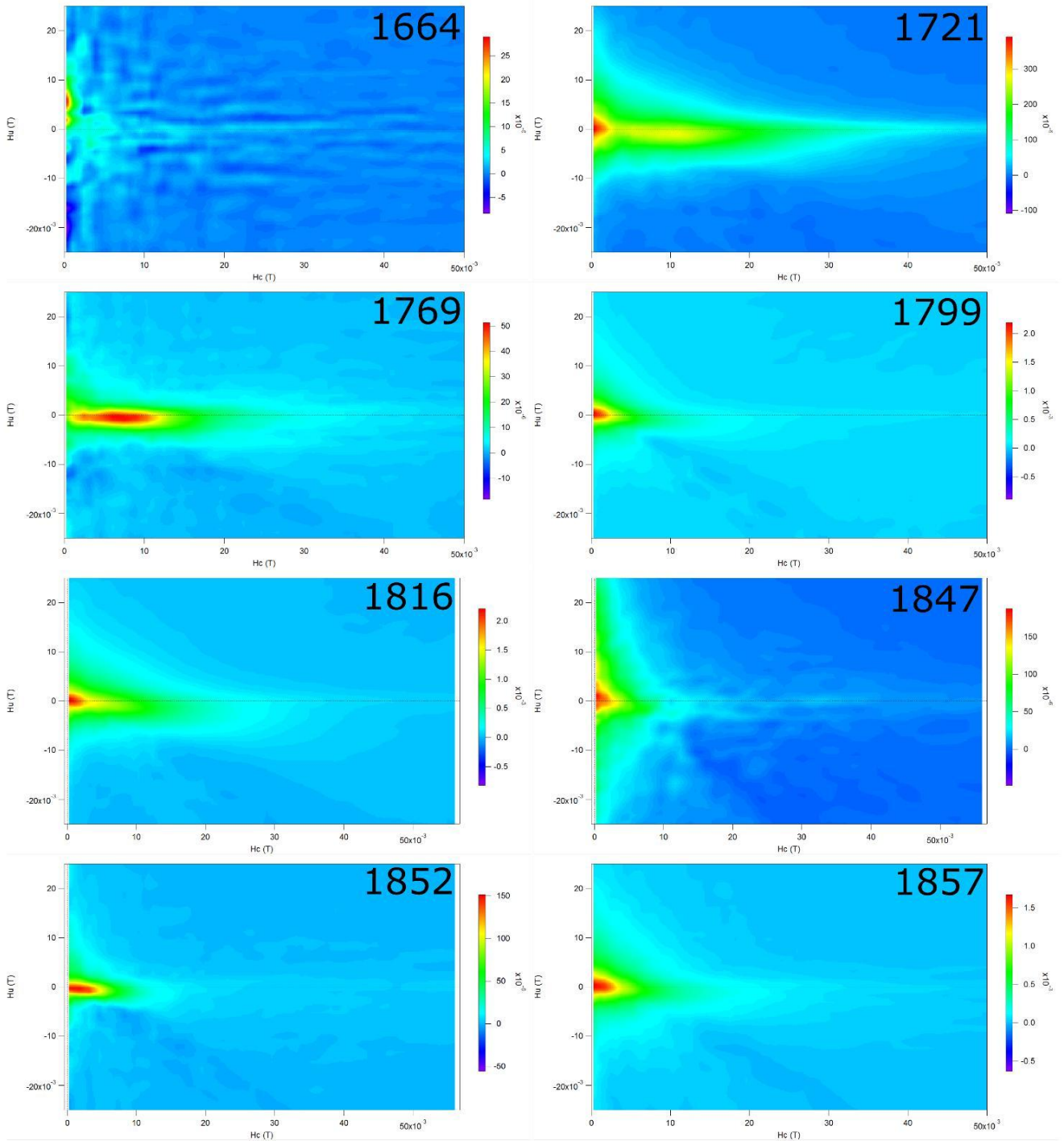
FIGURE 6.9: FORC diagrams of specimens from all flows. Raw FORCs were processed with the VARIFORC (R. Egli [2013]) function in FORCinel v1.5 (Harrison and Feinberg [2008]) for the software tool Igor Pro 7.
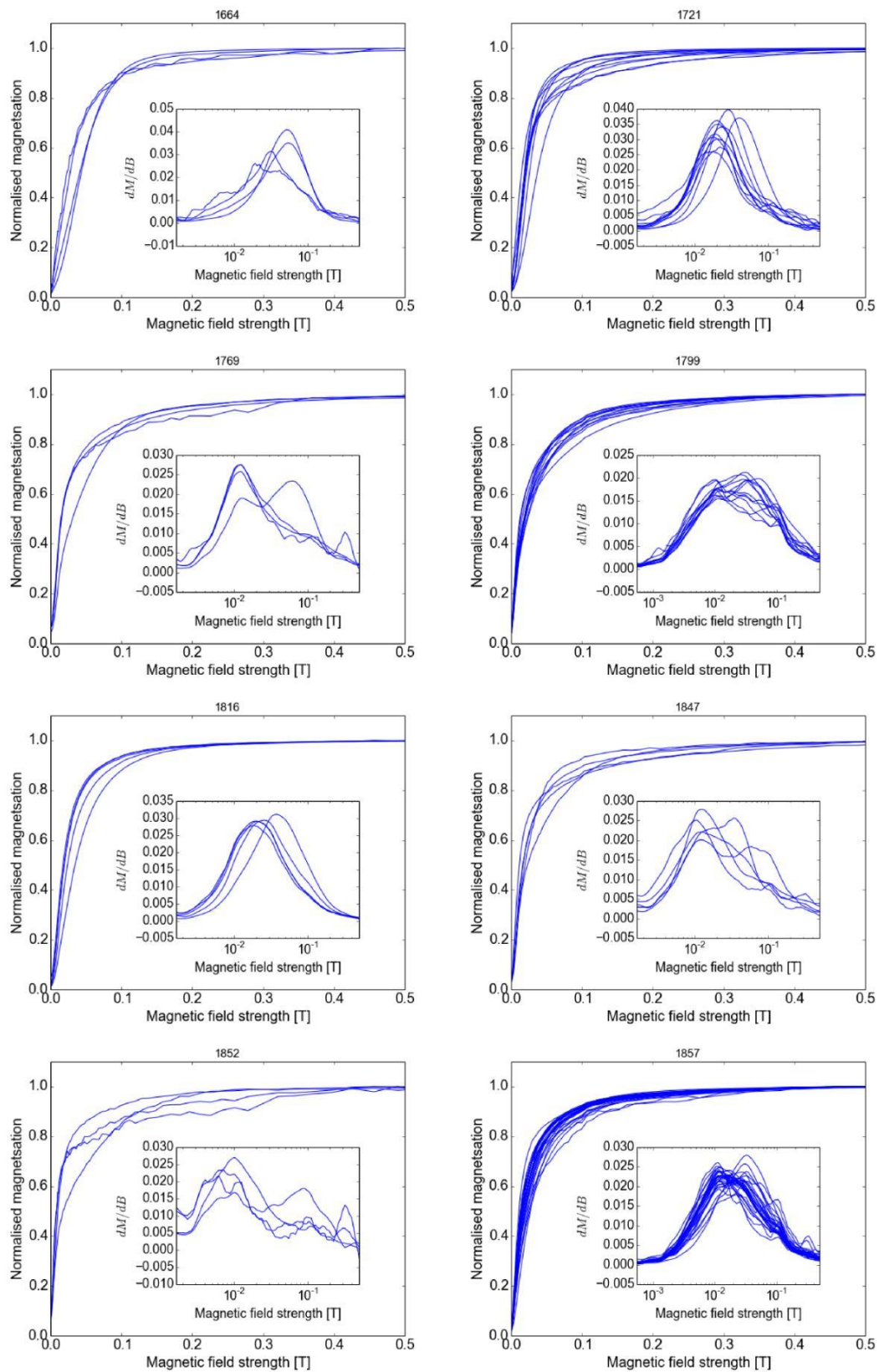
FIGURE 6.10: IRM curves
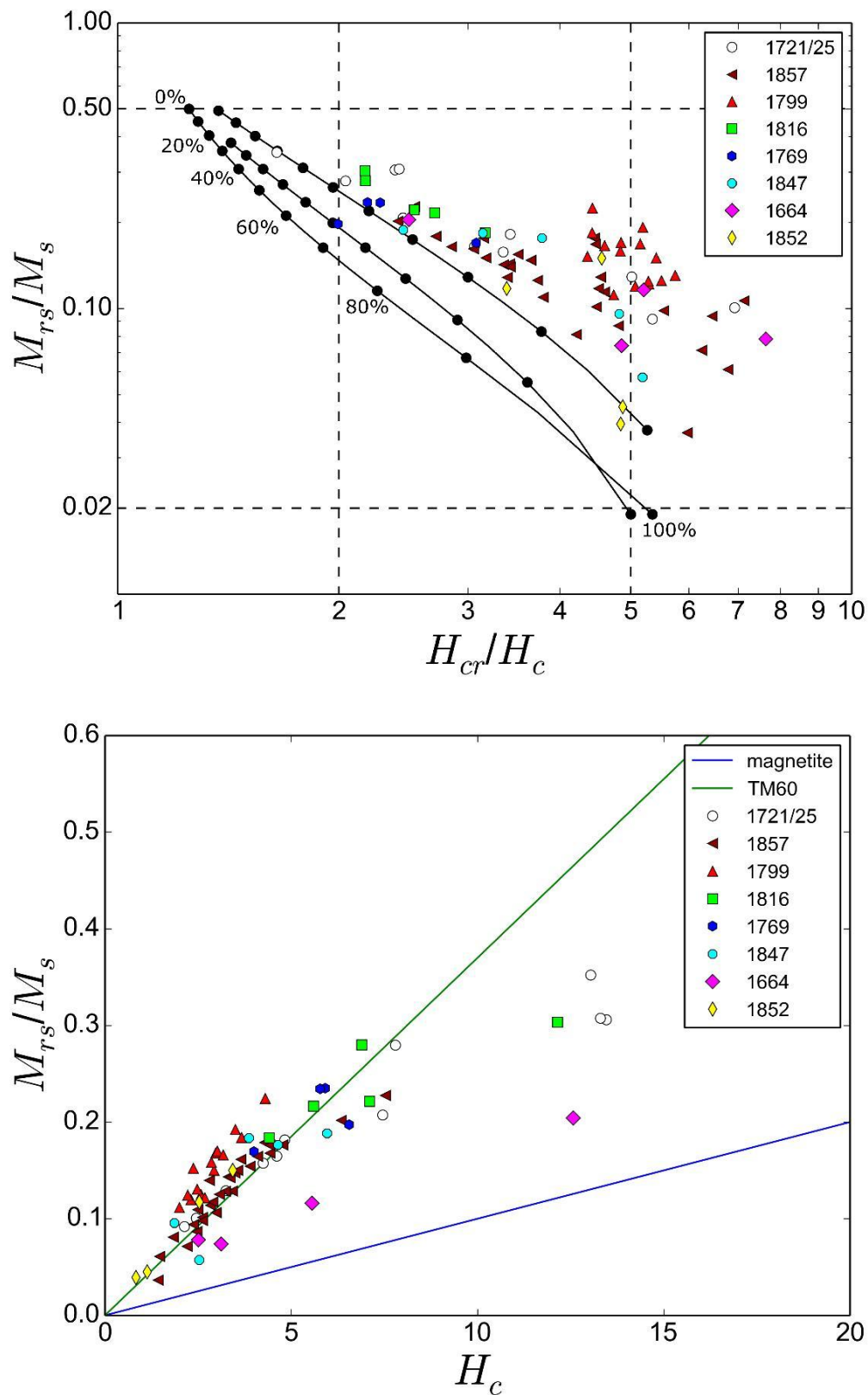
FIGURE 6.11: Upper panel: Dayplot of all 8 samples showing mostly pseudo-single-domain behaviour. The three solid lines are theoretical SD + MD mixing curves from pure magnetite defined by Dunlop [2002]. The 1799 and the 1857 flow plots mainly in the super paramagnetic range, which indicates very small magnetic grain sizes. Lower panel: Squareness plot of the same samples. The two lines are linear regression lines of Wang and van der Voo [2004]. Most specimen plot close to the TM60 line, but some have an even higher titanium content.
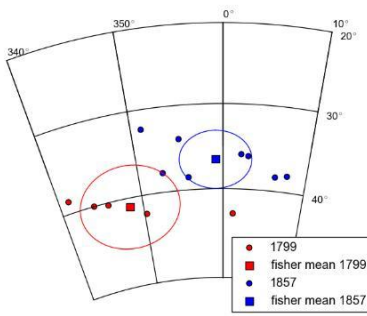
FIGURE 6.12: Stereographic plot of fisher mean directions.

flow	Declination	Inclination	N_C	N	k	α_{95}
Fogo 1799 TH	-10.5	42.5	4	5	209	4.8
Fogo 1799 AF	-10.9	40.4	5	5	131	5.5
Fogo 1799 all	-11.7	41.0	5	10	173	4.8
Fogo 1857 TH	-1.2	36.1	4	5	156	5.6
Fogo 1857 AF	-1.2	37.4	5	5	263	3.9
Fogo 1857 all	-0.8	36.6	8	10	214	3.4

TABLE 6.2: Paleodirection results for the oriented flows. AF is abbreviated for alternating field demagnetisation and TH for thermal demagnetisation. N is the number of specimens and N_C is the number of cores that was investigated.

uncertainties. Paleomagnetic mean directions were calculated using Fisher statistics (Fisher 1953) and are plotted in Fig. 6.12. The results (table 6.2) are in general very consistent except specimens of the 1799-01-01 core which show a strongly deviating declination in both thermal and AF demagnetisation from the other cores of around 15° (Fig. 6.14 top).

6.6.2 Paleomagnetic intensities

The microwave demagnetisation experiments that were done prior to the actual paleointensity experiments showed promising behaviour for 4 out of the 8 flows that had stable principle components and in general no strong magnetic overprint. These flows were 1664, 1769, 1816 and 1847. Microwave demagnetisation of flows 1721/25, 1799, 1852 and 1857 were noisy, multi-component or had an IRM overprint. In total 12 microwave demagnetisation experiments were done.

The Arai plots of the samples that seemed suitable have in general the following characteristics. The 1664 flow shows a "Zigg-Zagg" pattern which could suggest multi-domain magnetic grains. The 1769 and 1847 flow have slightly curved Arai plots, which could be due to multiple components or alteration at higher microwave powers. The Arai plots of the 1816 flow seem to have a noisy direction of the principle component for a few cases. Some Arai plot examples of this study are shown in figure 6.17.

To process the paleointensitiy data 3 approaches were used. First the acceptance criteria and their values were used of Cromwell et al. [2015] and applied to all Arai plot intervals from the individual specimens. Secondly a consistency test regardless of rigorous selection criteria was

done. Finally adapted values of the selection criteria from Cromwell et al. [2015] were applied to the Arai plots to achieve a higher success rate and make use of the overall consistency of the results.

1 To assess the quality of the Araiplots the acceptance criteria from the work of Cromwell et al. [2015] were chosen (summarized in table 6.3). This study is very recent and also deals with volcanic material. It uses the following set of criteria. The SCAT which quantifies if the scatter of the Arai plot points is in certain bounds that depend on the error of the best fit slope. This a necessary parameter to reject strong multi-domain samples or samples with a strong overprint. The FRAC is the fraction of the Arai plot that was used for the linear fit. Gap Max is the maximum gap between two consecutive points in the Arai plot. MAD and DANG are used to reject specimen results with either a very noisy direction of the principle component or the cases in which the direction doesn't seem go towards the origin in the Zijderveld plots, which could be caused by multi-domain behaviour, strong magnetic overprints or chemical alteration. An important reason to use the criteria of Cromwell et al. [2015] with the parameter $|k'|$ that addresses the curvature of the Arai plot. This allows for a rejection of strongly curved intervals of the Arai plot. Sets of selection criteria from other studies like SELCRIT2 Biggin et al. [2007] or PICRIT03 Kissel and Laj [2004] don't use this parameter of $|k'|$ which seems useful for this study because of the curved nature of some of the Arai plots. Applying the acceptance criteria of Cromwell et al. [2015]. with the exact values led to rejecting almost all specimen results. Only 2 result from 1664 and one result from 1769 were able to fulfill these criteria which gives a success rate of about 8 percent.

2 A consistency test was done with all paleointensity results in which only the SCAT criterion had to be fulfilled. This will ensure to remove results with strongly non linear Arai plots. These paleointensities are plotted as a histogram in figure 6.15. Even if the range of possible paleointensities is very big it is clear that some results are more preferable as others. 1664 and 1816 results show a clear peak in the histograms while 1769 and 1847 results seem to scatter in more bins. The biggest populated bin of 1664 lies around 27 μT and 1816 around 43 μT. 1847 peaks around $39\mu T$ which is also the value of the gufm1 model from Jackson et al. [2000]. 1769 shows the most inconsistent result with an approximate paleointensity of 45 μT. These estimates are associated with quality parameters of the Arai plots and can be used to look for parameter thresholds that create very consistent results. In figure 6.16 the parameters are plotted for all fits of the 1847 flow that result in a paleointensity

of $39 \pm 4\mu T$. For the criteria $|k'|$, MAD and DANG a significant drop in the number of paleointensities that agree with the estimated field value of gufm1 i.e. the peak in the histogram is visible. For the case of beta and Gap Max the threshold values of Cromwell at al. were used because the histogram was not conclusive i.e. no clear threshold can be seen in the histograms. Very important is the fact that even results with a very low FRAC agree well with the field value of gufm1, which allows for more specimens to pass the acceptance criteria. The same analysis can be done for the other flows and gives very similar thresholds. The new adapted criteria are shown in table 6.3.

3 Applying the adapted acceptance criteria to the data leads to a success rate of 60 percent which allows at least 5 specimen results per flow for the determination of the paleointensity. The final sample result is calculated by averaging over the specimen results. These were calculated in two different ways. The first way is also used by the Thellier GUI [Shaar and Tauxe, 2013] which selects the specimen results by standard deviation optimization i.e. choosing the combination of all specimen results which minimizes the standard deviation of the final paleointensity, denoted in table 6.4 as "STDEV-OPT". The second way to calculate the specimen result is by averaging over all acceptable values and not only choose one paleointensity (denoted as "Average"). This method should be more sensitive to big inconsistencies in the Arai plot interpretations.

The paleointensity results of the scheme described above are summarized in table 6.4. The paleointesities for the specimen results are determined by standard deviation optimization which means that out of all the different intervals of the Arai plot which fulfilled the acceptance criteria the results with the lowest standard deviation of the slope were chosen. The specimens that didn't give results with acceptable quality parameters are also shown with a remark of what criteria could not be fulfilled. An example of odd demagnetisation is shown in figure 6.13. Here some of the pTRM checks are failing and the demagnetisation behaviour in general is very inconsistent.

The two different ways to calculate the paleointensities for the whole flow give very similar results. That would suggest that even if the possible interval of paleointensities is large (can be seen from the values of the end members from the STDEV-OPT result) the average still tends to be a stable solution.

Parameter	[Cromwell et al., 2015]	Adapted values
SCAT	True	True
FRAC	≥ 0.78	≥ 0.1
Gap max	≤ 0.6	≤ 0.6
β	≤ 0.1	≤ 0.1
$|k'|$	≤ 0.164	≤ 0.3
DANG	≤ 10	≤ 20
MAD	≤ 5	≤ 10

TABLE 6.3: Acceptance criteria for the quality of Arai plots

Age [AD]	Specimen	$F_{anc}[\mu T]$	$\sigma_F[\mu T]$	Angle[°]	FRAC	$|k'|$	β	MAD[°]	DANG[°]	Gap Max	Remarks
1664	1664-01-01-A1	27.9	0.9	89	0.74	0.06	0.03	5.4	5.9	0.3	
1664	1664-01-03-A1	28.0	0.8	71	0.60	0.04	0.03	4.0	4.8	0.4	
1664	1664-01-03-A6	28.0	2.3	73	0.50	0.28	0.08	5.0	5.4	0.2	
1664	1664-01-02-B2	26.4	0.1	0	0.31	0.01	0.003	3.7	16.5	0.5	
1664	1664-01-03-A8	30.1	2.4	0	0.49	0.10	0.08	1.3	2.9	0.5	
1664	1664-01-02-B1	27.5	0.5	70	0.66	0.03	0.02	4.4	2.1	0.2	
1664	1664-01-03-A2	-	-	-	-	-	-	-	-	-	MAD fail
1664	1664-01-03-A3	-	-	-	-	-	-	-	-	-	odd demag.
1664	1664-01-03-A5	-	-	-	-	-	-	-	-	-	odd demag.
1664	1664-01-03-A7	-	-	-	-	-	-	-	-	-	odd demag.
1664	**STDEV-OPT**	**28.0**	**[23.2-34.9]**								
1664	**Average**	**28.3**	**2.3**								
1769	1769-02-01-B1	43.6	3.8	56	0.16	0.30	0.09	7.3	4.8	0.3	
1769	1769-02-02-B1	47.1	3.7	52	0.43	0.19	0.08	8.9	9.0	0.2	
1769	1769-02-02-B2	45.5	1.0	55	0.74	0.03	0.02	6.6	13.7	0.4	
1769	1769-02-02-A1	45.4	2.0	53	0.45	0.17	0.04	5.9	12.2	0.2	
1769	1769-02-02-A2	45.5	2.1	54	0.33	0.28	0.05	3.0	8.5	0.2	
1769	1769-01-01-A1	-	-	-	-	-	-	-	-	-	overprint
1769	1769-01-01-A2	-	-	-	-	-	-	-	-	-	MAD fail
1769	1769-01-03-A1	-	-	-	-	-	-	-	-	-	$|k'|$ fail
1769	1769-02-01-A1	-	-	-	-	-	-	-	-	-	overprint
1769	**STDEV-OPT**	**45.4**	**[29.2-54.2]**								
1769	**Average**	**45.0**	**3.0**								
1816	1816-01-01-B1	43.2	1.7	90	0.39	0.13	0.04	5.5	11.0	0.2	
1816	1816-01-03-B1	43.0	1.6	77	0.16	0.03	0.04	8.9	7.9	0.2	
1816	1816-01-01-A1	43.0	1.7	90	0.14	0.14	0.04	7.2	4.2	0.3	
1816	1816-01-04-A1	42.8	1.9	90	0.36	0.29	0.05	5.0	6.3	0.2	
1816	1816-01-02-B1	43.1	1.1	90	0.40	0.01	0.03	3.3	7.7	0.1	
1816	1816-01-04-B2	-	-	-	-	-	-	-	-	-	overprint
1816	**STDEV-OPT**	**43.0**	**[28.7-59,5]**								
1816	**Average**	**42.9**	**3.1**								
1847	1847-01-04-A1	38.9	1.7	75	0.42	0.16	0.04	6.0	14.6	0.2	
1847	1847-01-02-B1	38.8	3.2	75	0.32	0.19	0.08	5.7	7.2	0.3	
1847	1847-01-04-B1	39.5	1.6	80	0.26	0.15	0.04	8.8	12.4	0.4	
1847	1847-01-04-A2	39.0	1.7	89	0.34	0.29	0.04	6.4	9.5	0.2	
1847	1847-01-04-B3	39.4	1.7	68	0.27	0.22	0.04	7.0	19.4	0.3	
1847	1847-01-02-A1	-	-	-	-	-	-	-	-	-	$|k'|$ fail
1847	1847-01-02-C1	-	-	-	-	-	-	-	-	-	$|k'|$ fail
1847	1847-01-03-A1	-	-	-	-	-	-	-	-	-	overprint
1847	1847-01-04-B2	-	-	-	-	-	-	-	-	-	DANG fail
1847	1847-01-03-B1	-	-	-	-	-	-	-	-	-	overprint
1847	**STDEV-OPT**	**39.1**	**[33.1-43.8]**								
1847	**Average**	**39.0**	**2.6**								

TABLE 6.4: Paleomagnetic intensities with associated quality parameters. Site results are calculated by taking the average of the specimen results. Specimen results are calculated by standard deviation optimization (**STDEV-OPT**) or by taking the mean paleointensity of all accepted best fits (**Average**). Uncertainties are the end members of all possible results and for the Average its the standard deviation.
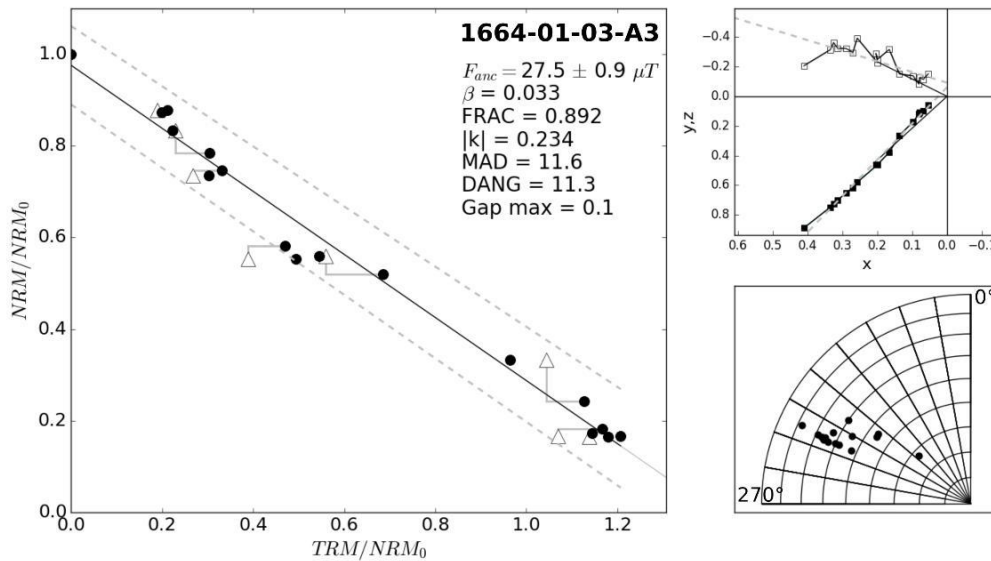
FIGURE 6.13: One example result for odd demagnetisation.

6.7 Discussion

6.7.1 Age estimation

Initial age estimations of the investigated flows were done based on a geological map of Torres [1997]. These estimations lead to volcanic flow ages of 1664, 1721-1725, 1769, 1799, 1816, 1847, 1852 and 1857. These ages were then corrected by comparison to Day et al. [2000].

Day suggested that the 1664 flow is definitely pre 1680 and the age should be finally 1663 ± 1. The 1721-25 flow is probably the 1785 flow. The 1769 is likely to be from 1769 but also could be from 1774 which leads to an estimated age from 1771.5 ± 2.5. The 1799 flow is probably part of the 1847 flow. According to Simon Day the 1816 flow is very unlikely to have happened in this year and occurred after the 1721-1725 eruption but before the 1785 Mt Losna eruption. This leads to an age estimation of 1755 ± 30. The ages of the 1847 and the 1852 flow are correct. The age of the 1857 flow is probably much older but of unknown age which leads to omitting the results of this flow.

Initial results were presented with the originally assumed ages earlier this chapter and are discussed in the following with newly estimated ages. Table 6.5 shows the results again but with adapted ages.
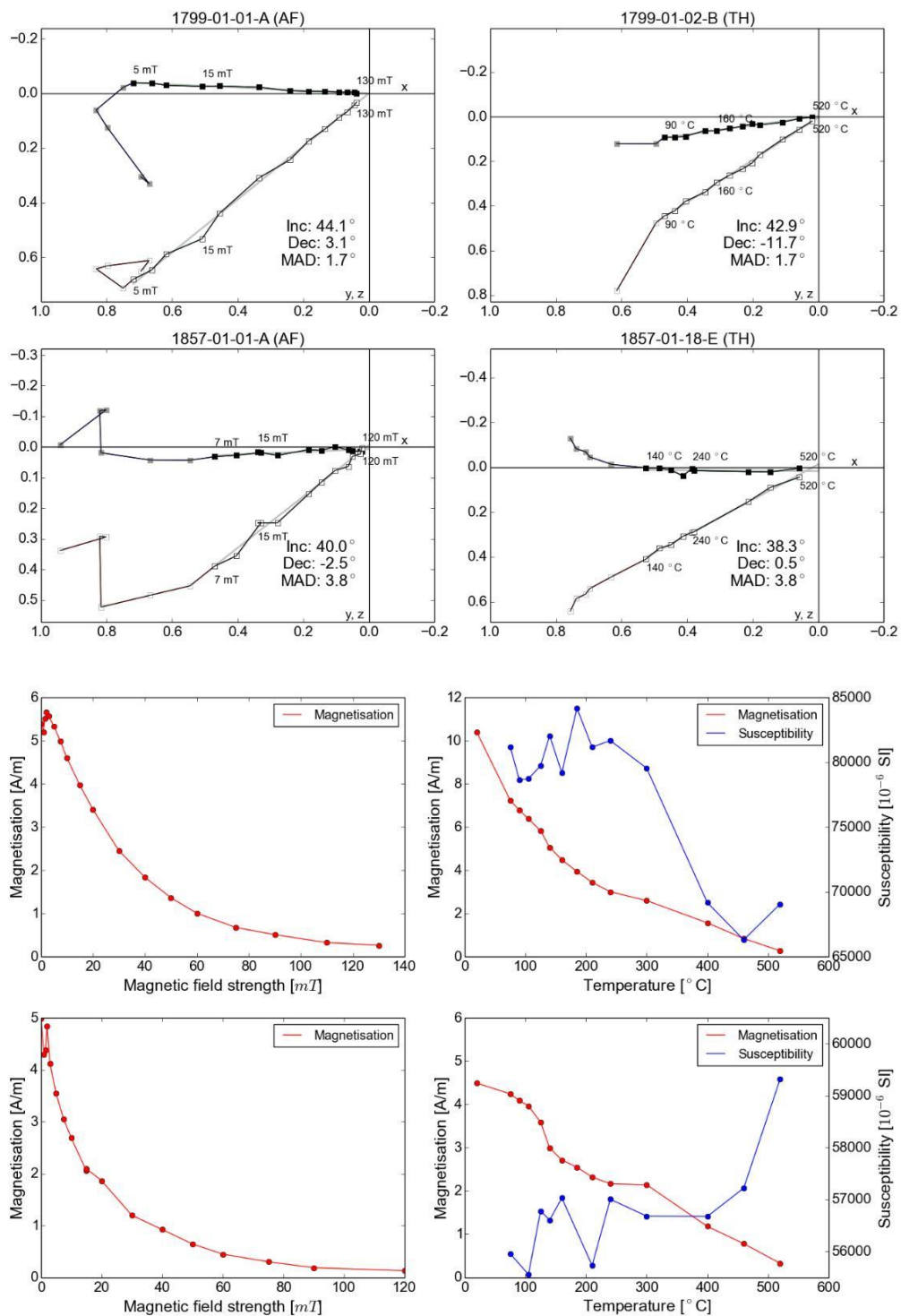
FIGURE 6.14: Upper panel: Zijderveld plot examples, 1799-01-01 specimen declinations deviate strongly from other 1799 cores. Lower panel: Demagnetisation/Susceptibility curves of the same specimens as in upper panel.
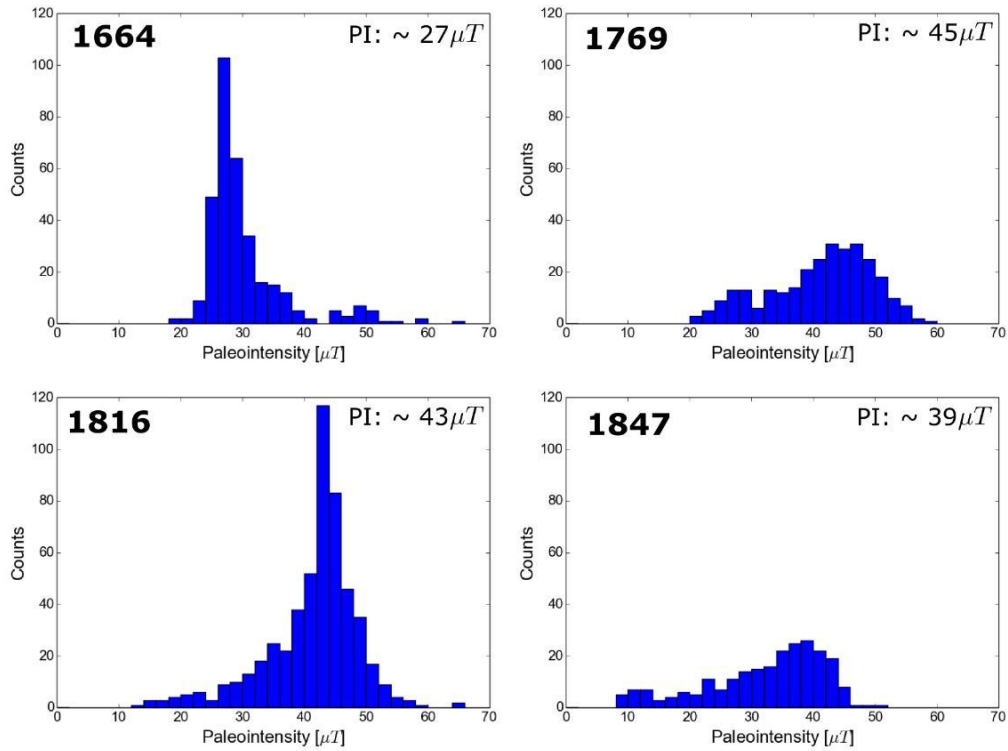
FIGURE 6.15: Histograms of paleointensities only constrained from the selection criteria SCAT. Paleointensities were estimated from most populated bins.
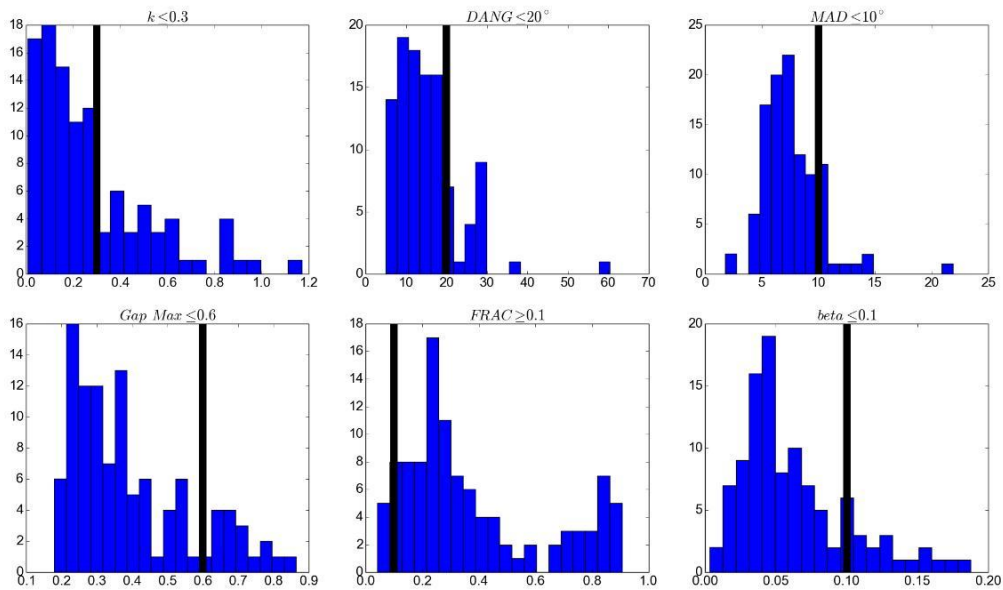
FIGURE 6.16: 1847 quality parameters of Arai plots that result in a paleointensity of 39 ± 4 μT
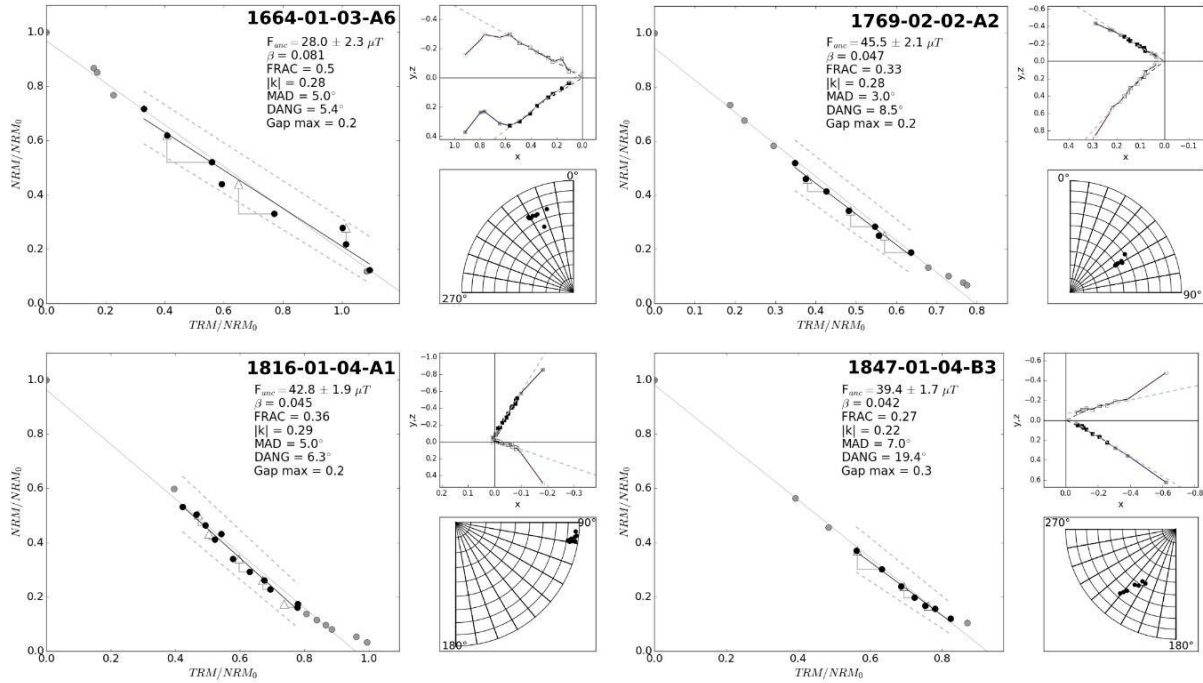
FIGURE 6.17: Examples of Arai plots from successful experiments: black points are chosen by standard deviation optimization for best line fit, dashed grey lines are the bounds for the SCAT criteria, solid grey lines are best fits of all Arai plot points, white arrows indicate the pTRM checks. Left side of Arai plot shows associated Zijderveld and stereographic plot of the direction: black points represent positive inclination and white points negative inclination.

Age flow[years AD]	$F_{anc}[\mu T]$	$\sigma_F[\mu T]$	dec [°]	inc [°]	α_{95}
1663 ± 1	28.3	2.3	-	-	-
1755 ± 30	42.9	3.1	-	-	-
1771.5 ± 2.5	45.0	3.0	-	-	-
1847	39.0	2.6	-11.7	41.0	4.8

TABLE 6.5: Averaged paleomagnetic results with adapted ages.

6.7.2 Comparison of the results to existing models and the 1000 year model

Figure 6.18 shows the paleomagnetic results of the lava flows compared to different models. All models fit the 1755, 1771.5 and the 1847 quite well. The exception is the 1663 flow, which shows a value that is around 10 μT smaller than the models suggest. Arch3k.1 and the 1000 year model fit this flow better than gufm1 which is probably due to intensity data at this time constraining these models. As previously already seen, volcanic data can be very inconsistent and spreads over a big range of values. A lot of paleomagnetic results are needed to make a more reliable estimate of ancient magnetic field values. Another problem is, as previously discussed, that the age of lava flows is not easy to determine and there might be still some inaccuracies.
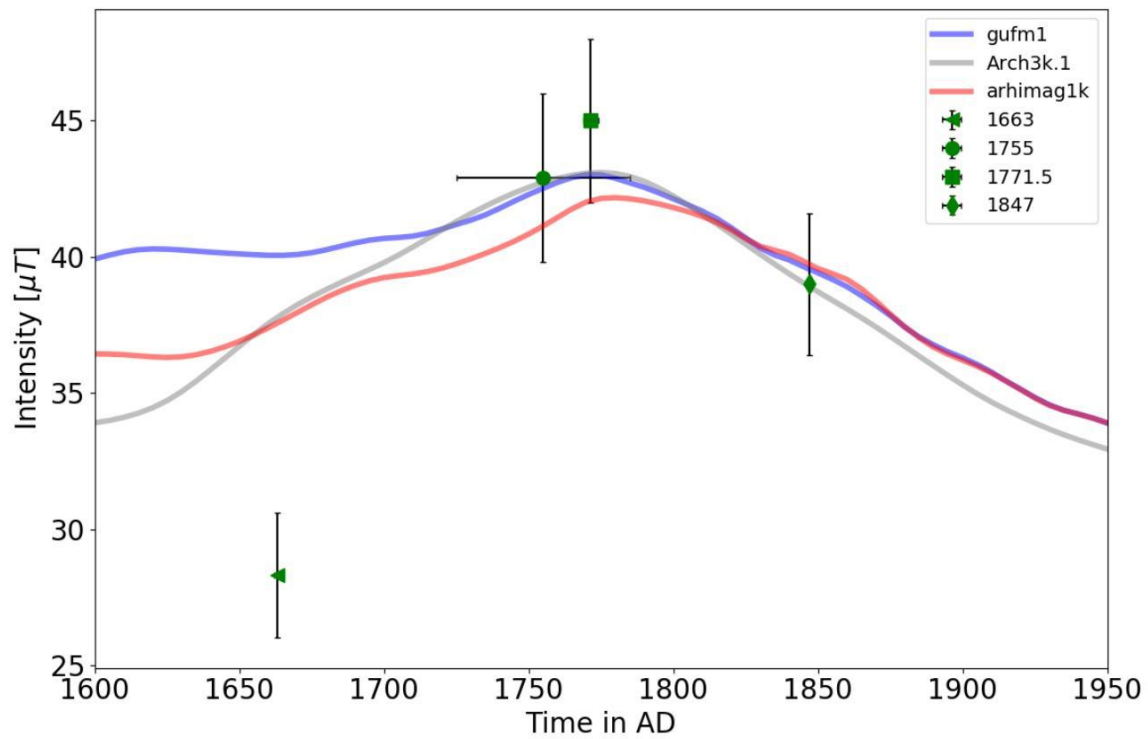
FIGURE 6.18: Paleomagnetic results of the lava flow compared to different models.

The magnetic field intensity snapshots of arhimag1k in chapter 5 showed that the SAA drifted between 1600 and 2000 AD from Africa to its current location. Cape Verde is approximately 700km west of Africa, which means that the SAA was much closer to Fogo around 1600 AD than it currently is. Hence it is expected that the field intensity at that time should be lower than 1800 AD.

Chapter 7

Summary and outlook

One of the challenges mentioned in chapter 1 was to investigate, how much information can reliably be drawn out of models based on purely archeo- and paleomagnetic data. In chapter 4 2000 geomagnetic models based on data associated with randomized uncertainties were calculated. Investigating the radial component of the magnetic field at the CMB revealed that large scale structure are generally very similar throughout the models. Further this means that estimation for the dipole moment as a global feature should be reliable apart from a constant offset, which originates from a very uneven data distribution. The average coefficient g_1^0 of all archeo-/paleomagnetic models showed a deviation from the linear extrapolation that gufm1 assumed before 1840 AD. The models show a constant evolution of g_1^0 from 1650 to 1800 AD instead.

The statistical analysis in chapter 4 also led to the data weightings used for the final model. The most important indicator for weighting the data was found to be the material of the archeo-/paleomagnetic samples. The uncertainties given by the authors lead to unrealistic models, which was solved by attributing more consistent uncertainties dependent on the materials. Volcanic material and tiles were given the highest uncertainties and backed clay, pottery or brick were given the lowest uncertainties. All other or undefined materials were given an intermediate uncertainty. All directional data was weighted the same.

The final model arhimag1k was calculated by combining historical data and archeo-/paleomagnetic data for the inversion. To address the big jump in data count between 1800 and 1900 a time dependent spatial damping is used, which leads to a controlled spatial complexity over time. The model fits different datasets well, especially the high quality data of [Gallet et al., 2005] and

[Genevey et al., 2009] is fitted better than for other models. Intensity snapshots of the model show the movement of the SAA from Africa to its current location in the South Atlantic area between 1600 AD to 2000 AD. Snapshots of the radial component of the magnetic field at the CMB show an early reverse flux patch between 1000 and 1200 AD in the South Atlantic area which disappears after. Another interesting feature is a high latitude flux patch over Greenland between 1200 and 1400 AD. The dipole moment evolution shows a deviating behaviour from gufm1 before 1840 AD. Contrary to the linear decrease it shows a constant evolution from 1600 to 1840 AD in agreement with Finlay [2008] and Gubbins [2006]. Finally longitude-time plots were made to research the drift magnetic field feature at the CMB. At the equator no clear drift is visible before 1600 AD. After 1600 a clear westward drift is appearing with a drift speeds around 0,3 $°/yr$ which is in agreement with other studies. At 30 $°$ N shows drifting before 1600 AD.

Chapter 6 presents 4 new paleointensities from 4 different flows of the island Fogo, which is part of Cape Verde. The data is fitted well by arhimag1k, Arch3k.1 and gufm1 with the exception of the value at 1663 of $28.3 \pm 2.3 \mu T$, which is approximately $10\mu T$ lower than the models suggest.

The model arhimag1k combines archeo-/paleomagnetic and historical data in one model over a time period of 1000 years. This model is far from perfect and has very low resolution in the southern hemisphere. More and reliable data is needed to get a more complete picture of the changes in the magnetic field to for example solve the question, where exactly the reverse flux patches are created and how they evolve.

For future works arhimag1k can be used for data assimilation as data input combined with a physical model of the core dynamics ([Kuang et al., 2008]). With the help of the radial component of the magnetic field at the CMB the fluid flow in the outer core can be estimated ([Bloxham and Jackson, 1991]). Also new archeo-/paleomagnetic data can be compared with arhimag1k to estimate or confirm their reliability or age.

Bibliography

A. C. Fraser-Smith. Centered and eccentric geomagnetic dipoles and their poles, 1600–1985. *Reviews of Geophysics*, 25(1):1, 1987. doi: 10.1029/rg025i001p00001. URL `https://doi.org/10.1029/rg025i001p00001`.

Niels Abrahamsen. On shape anisotropy, refraction error and possible refraction correction in paleomagnetism. *EOS, Trans. Am. geophys. Un*, 67:268, 1989.

J.M. Ade-Hall. Strong field magnetic properties of basalts from DSDP leg 26. In *Initial Reports of the Deep Sea Drilling Project*. International Ocean Discovery Program (IODP), dec 1974. doi: 10.2973/dsdp.proc.26.119.1974. URL `https://doi.org/10.2973/dsdp.proc.26.119.1974`.

Patrick Arneitz, Roman Leonhardt, Elisabeth Schnepp, Balázs Heilig, Franziska Mayrhofer, Peter Kovacs, Pavel Hejda, Fridrich Valach, Gergely Vadasz, Christa Hammerl, Ramon Egli, Karl Fabian, and Niko Kompein. The HISTMAG database: combining historical, archaeomagnetic and volcanic data. *Geophysical Journal International*, 210(3):1347–1359, jun 2017. doi: 10.1093/gji/ggx245. URL `https://doi.org/10.1093/gji/ggx245`.

Gautam D. Badhwar. Drift rate of the South Atlantic Anomaly. *Journal of Geophysical Research: Space Physics*, 102(A2):2343–2349, feb 1997. doi: 10.1029/96ja03494. URL `https://doi.org/10.1029/96ja03494`.

A. J. Biggin, B. Steinberger, J. Aubert, N. Suttie, R. Holme, T. H. Torsvik, D. G. van der Meer, and D. J. J. van Hinsbergen. Possible links between long-term geomagnetic variations and whole-mantle convection processes. *Nature Geoscience*, 5(8):526–533, jul 2012. doi: 10.1038/ngeo1521. URL `https://doi.org/10.1038/ngeo1521`.

Andrew J. Biggin, Mireille Perrin, and Mark J. Dekkers. A reliable absolute palaeointensity determination obtained from a non-ideal recorder. *Earth and Planetary Science Letters*, 257

(3-4):545–563, may 2007. doi: 10.1016/j.epsl.2007.03.017. URL `https://doi.org/10.1016/j.epsl.2007.03.017`.

Bleil and Petersen. *Magnetic properties of natural minerals.* Springer, New York, 1982.

J. Bloxham, D. Gubbins, and A. Jackson. Geomagnetic Secular Variation. *Philosophical Transactions of the Royal Society A: Mathematical, Physical and Engineering Sciences*, 329(1606): 415–502, nov 1989. doi: 10.1098/rsta.1989.0087. URL `https://doi.org/10.1098/rsta.1989.0087`.

Jeremy Bloxham and Andrew Jackson. Fluid flow near the surface of Earth's outer core. *Reviews of Geophysics*, 29(1):97, 1991. doi: 10.1029/90rg02470. URL `https://doi.org/10.1029/90rg02470`.

Jeremy Bloxham and Andrew Jackson. Time-dependent mapping of the magnetic field at the core-mantle boundary. *Journal of Geophysical Research*, 97(B13):19537, 1992. doi: 10.1029/92jb01591. URL `https://doi.org/10.1029/92jb01591`.

Julie A. Bowles, Mike J. Jackson, Thelma S. Berquó, Peter A. Sølheid, and Jeffrey S. Gee. Inferred time- and temperature-dependent cation ordering in natural titanomagnetites. *Nature Communications*, 4(1), may 2013. doi: 10.1038/ncomms2938. URL `https://doi.org/10.1038/ncomms2938`.

Maxwell C Brown, Fabio Donadini, Andreas Nilsson, Sanja Panovska, Ute Frank, Kimmo Korhonen, Maximilian Schuberth, Monika Korte, and Catherine G Constable. GEOMAGIA50.v3: 2. a new paleomagnetic database for lake and marine sediments. *Earth, Planets and Space*, 67(1), may 2015. doi: 10.1186/s40623-015-0233-z. URL `https://doi.org/10.1186/s40623-015-0233-z`.

Robert F. Butler. *Paleomagnetism: Magnetic Domains to Geologic Terranes.* Blackwell Science Inc, 1991. ISBN 086542070X. URL `https://www.amazon.com/Paleomagnetism-Magnetic-Domains-Geologic-Terranes/dp/086542070X?SubscriptionId=AKIAIOBINVZYXZQZ2U3A&tag=chimbori05-20&linkCode=xm2&camp=2025&creative=165953&creativeASIN=086542070X`.

C. F. Gauss. Die Intensität der erdmagnetischen Kraft, zurückgeführt auf absolutes Maass. *Annalen der Physik und Chemie*, 104(6):241–273, 1833. doi: 10.1002/andp.18331040602. URL `https://doi.org/10.1002/andp.18331040602`.

Coe. The determination of paleo-intensities of the Earth's magnetic field with emphasis on mechanisms which could cause non-ideal behavior in Thellier's method. *Journal of Geomagnetism and Geoelectricity*, 19(3):157–179, 1967.

R. S. Coe. The effect of shape anisotropy on TRM direction. *Geophysical Journal International*, 56(2):369–383, feb 1979. doi: 10.1111/j.1365-246x.1979.tb00170.x. URL `https://doi.org/10.1111/j.1365-246x.1979.tb00170.x`.

C. G. Constable, C. L. Johnson, and S. P. Lund. Global geomagnetic field models for the past 3000 years: transient or permanent flux lobes? *Philosophical Transactions of the Royal Society A: Mathematical, Physical and Engineering Sciences*, 358(1768):991–1008, mar 2000. doi: 10.1098/rsta.2000.0570. URL `https://doi.org/10.1098/rsta.2000.0570`.

Catherine Constable, Monika Korte, and Sanja Panovska. Persistent high paleosecular variation activity in southern hemisphere for at least 10 000 years. *Earth and Planetary Science Letters*, 453:78–86, nov 2016. doi: 10.1016/j.epsl.2016.08.015. URL `https://doi.org/10.1016/j.epsl.2016.08.015`.

G. Cromwell, L. Tauxe, and S. A. Halldórsson. New paleointensity results from rapidly cooled Icelandic lavas: Implications for Arctic geomagnetic field strength. *Journal of Geophysical Research: Solid Earth*, 120(5):2913–2934, may 2015. doi: 10.1002/2014jb011828. URL `https://doi.org/10.1002/2014jb011828`.

S. J. Day, J. C. Carracedo, H. Guillou, F. J. Pais Pais, E. Rodriguez Badiola, J. F. B. D. Fonseca, and S. I. N. Heleno. Comparison and cross-checking of historical, archaeological and geological evidence for the location and type of historical and sub-historical eruptions of multiple-vent oceanic island volcanoes. *Geological Society, London, Special Publications*, 171(1):281–306, 2000. doi: 10.1144/gsl.sp.2000.171.01.21. URL `https://doi.org/10.1144/gsl.sp.2000.171.01.21`.

Fabio Donadini, Kimmo Korhonen, Peter Riisager, and Lauri J. Pesonen. Database for Holocene geomagnetic intensity information. *Eos Transactions American Geophysical Union*, 87:137–143, 01 2006. doi: 10.1029/2006EO140002.

Mathieu Dumberry and Christopher C. Finlay. Eastward and westward drift of the Earth's magnetic field for the last three millennia. *Earth and Planetary Science Letters*, 254(1-2):146–157, feb 2007. doi: 10.1016/j.epsl.2006.11.026. URL `https://doi.org/10.1016/j.epsl.2006.11.026`.

David J. Dunlop. Theory and application of the Day plot (M_{rs}/M_s versus H_{cr}/H_c) 1. Theoretical curves and tests using titanomagnetite data. *Journal of Geophysical Research*, 107(B3), 2002. doi: 10.1029/2001jb000486. URL `https://doi.org/10.1029/2001jb000486`.

M. E. Evans and M. L. Wayman. An investigation of the role of ultra-fine titanomagnetite intergrowths in palaeomagnetism. *Geophysical Journal International*, 36(1):1–10, jan 1974. doi: 10.1111/j.1365-246x.1974.tb03621.x. URL `https://doi.org/10.1111/j.1365-246x.1974.tb03621.x`.

F. J. Lowes. Mean-square values on sphere of spherical harmonic vector fields. *Journal of Geophysical Research*, 71(8):2179–2179, apr 1966. doi: 10.1029/jz071i008p02179. URL `https://doi.org/10.1029/jz071i008p02179`.

K. Fabian, V. P. Shcherbakov, and S. A. McEnroe. Measuring the Curie temperature. *Geochemistry, Geophysics, Geosystems*, 14(4):947–961, apr 2013. doi: 10.1029/2012gc004440. URL `https://doi.org/10.1029/2012gc004440`.

C. C. Finlay. Equatorially Dominated Magnetic Field Change at the Surface of Earth's Core. *Science*, 300(5628):2084–2086, jun 2003. doi: 10.1126/science.1083324. URL `https://doi.org/10.1126/science.1083324`.

Christopher C. Finlay. Historical variation of the geomagnetic axial dipole. *Physics of the Earth and Planetary Interiors*, 170(1-2):1–14, sep 2008. doi: 10.1016/j.pepi.2008.06.029. URL `https://doi.org/10.1016/j.pepi.2008.06.029`.

Yves Gallet, Agnès Genevey, and Frédéric Fluteau. Does earth's magnetic field secular variation control centennial climate change? *Earth and Planetary Science Letters*, 236(1-2):339–347, jul 2005. doi: 10.1016/j.epsl.2005.04.045. URL `https://doi.org/10.1016/j.epsl.2005.04.045`.

K.P. Games and P.J. Davey. Archaeomagnitude determinations for Britain and south-west USA from 600 AD to 1700 AD and their implications for medieval pottery studies. *Medieval Ceramics*, 1985.

Gellibrand. *A Discourse Mathematical on the Variation of the Magneticall Needle*. London, 1635.

Agnês Genevey, Yves Gallet, Jean Rosen, and Maxime Le Goff. Evidence for rapid geomagnetic field intensity variations in Western Europe over the past 800 years from new French

archeointensity data. *Earth and Planetary Science Letters*, 284(1-2):132–143, jun 2009. doi: 10.1016/j.epsl.2009.04.024. URL `https://doi.org/10.1016/j.epsl.2009.04.024`.

Gary A. Glatzmaiers and Paul H. Roberts. A three-dimensional self-consistent computer simulation of a geomagnetic field reversal. *Nature*, 377(6546):203–209, sep 1995. doi: 10.1038/377203a0. URL `https://doi.org/10.1038/377203a0`.

D. Gubbins. Fall in Earth's Magnetic Field Is Erratic. *Science*, 312(5775):900–902, may 2006. doi: 10.1126/science.1124855. URL `https://doi.org/10.1126/science.1124855`.

Gustav Hellmann. *Neudrucke Von Schriften Und Karten Uber Meteorologie Und Erdmagnetismus (German Edition)*. Hansebooks, 2017.

Richard J. Harrison and Joshua M. Feinberg. FORCinel: An improved algorithm for calculating first-order reversal curve distributions using locally weighted regression smoothing. *Geochemistry, Geophysics, Geosystems*, 9(5), may 2008. doi: 10.1029/2008gc001987. URL `https://doi.org/10.1029/2008gc001987`.

Gelvam A. Hartmann and Igor G. Pacca. Time evolution of the South Atlantic Magnetic Anomaly. *Anais da Academia Brasileira de Ciências*, 81(2):243–255, jun 2009. doi: 10.1590/s0001-37652009000200010. URL `https://doi.org/10.1590/s0001-37652009000200010`.

Gelvam A. Hartmann, Agnès Genevey, Yves Gallet, Ricardo I.F. Trindade, Carlos Etchevarne, Maxime Le Goff, and Marisa C. Afonso. Archeointensity in Northeast Brazil over the past five centuries. *Earth and Planetary Science Letters*, 296(3-4):340–352, aug 2010. doi: 10.1016/j.epsl.2010.05.016. URL `https://doi.org/10.1016/j.epsl.2010.05.016`.

Gelvam A. Hartmann, Agnès Genevey, Yves Gallet, Ricardo I.F. Trindade, Maxime Le Goff, Rosana Najjar, Carlos Etchevarne, and Marisa C. Afonso. New historical archeointensity data from Brazil: Evidence for a large regional non-dipole field contribution over the past few centuries. *Earth and Planetary Science Letters*, 306(1-2):66–76, jun 2011. doi: 10.1016/j.epsl.2011.03.030. URL `https://doi.org/10.1016/j.epsl.2011.03.030`.

D. Heynderickx. Comparison between methods to compensate for the secular motion of the South Atlantic anomaly. *Radiation Measurements*, 26(3):369–373, may 1996. doi: 10.1016/1350-4487(96)00056-x. URL `https://doi.org/10.1016/1350-4487(96)00056-x`.

Gauthier Hulot, Céline Eymin, Benoît Langlais, Mioara Mandea, and Nils Olsen. Small-scale structure of the geodynamo inferred from Oersted and Magsat satellite data. *Nature*, 416 (6881):620–623, apr 2002. doi: 10.1038/416620a. URL `https://doi.org/10.1038/416620a`.

Kenneth A. Hutcheson and David Gubbins. Earth's magnetic field in the seventeenth century. *Journal of Geophysical Research*, 95(B7):10769, 1990. doi: 10.1029/jb095ib07p10769. URL `https://doi.org/10.1029/jb095ib07p10769`.

A. Jackson, A. R. T. Jonkers, and M. R. Walker. Four centuries of geomagnetic secular variation from historical records. *Philosophical Transactions of the Royal Society A: Mathematical, Physical and Engineering Sciences*, 358(1768):957–990, mar 2000. doi: 10.1098/rsta.2000. 0569. URL `https://doi.org/10.1098/rsta.2000.0569`.

Art R. T. Jonkers, Andrew Jackson, and Anne Murray. Four centuries of geomagnetic data from historical records. *Reviews of Geophysics*, 41(2), 2003. doi: 10.1029/2002rg000115. URL `https://doi.org/10.1029/2002rg000115`.

J. L. Kirschvink. The least-squares line and plane and the analysis of palaeomagnetic data. *Geophysical Journal International*, 62(3):699–718, sep 1980. doi: 10.1111/j.1365-246x.1980. tb02601.x. URL `https://doi.org/10.1111/j.1365-246x.1980.tb02601.x`.

Catherine Kissel and Carlo Laj. Improvements in procedure and paleointensity selection criteria (PICRIT-03) for Thellier and Thellier determinations: application to Hawaiian basaltic long cores. *Physics of the Earth and Planetary Interiors*, 147(2-3):155–169, nov 2004. doi: 10. 1016/j.pepi.2004.06.010. URL `https://doi.org/10.1016/j.pepi.2004.06.010`.

Mads Faurschou Knudsen, Bo Holm Jacobsen, and Niels Abrahamsen. Palaeomagnetic distortion modelling and possible recovery by inversion. *Physics of the Earth and Planetary Interiors*, 135(1):55–73, jan 2003. doi: 10.1016/s0031-9201(02)00203-0. URL `https://doi.org/10.1016/s0031-9201(02)00203-0`.

M. Korte and C. G. Constable. Continuous geomagnetic field models for the past 7 millennia: 2. CALS7K. *Geochemistry, Geophysics, Geosystems*, 6(2), feb 2005. doi: 10.1029/2004gc000801. URL `https://doi.org/10.1029/2004gc000801`.

M. Korte, F. Donadini, and C. G. Constable. Geomagnetic field for 0-3 ka: 2. a new series of time-varying global models. *Geochemistry, Geophysics, Geosystems*, 10(6):n/a–n/a, June 2009. doi: 10.1029/2008gc002297. URL `https://doi.org/10.1029/2008gc002297`.

Monika Korte and Catherine Constable. Continuous global geomagnetic field models for the past 3000 years. *Physics of the Earth and Planetary Interiors*, 140(1-3):73–89, nov 2003. doi: 10.1016/j.pepi.2003.07.013. URL `https://doi.org/10.1016/j.pepi.2003.07.013`.

Monika Korte and Catherine Constable. Improving geomagnetic field reconstructions for 0–3ka. *Physics of the Earth and Planetary Interiors*, 188(3-4):247–259, oct 2011. doi: 10.1016/j.pepi.2011.06.017. URL `https://doi.org/10.1016/j.pepi.2011.06.017`.

Monika Korte, Catherine Constable, Fabio Donadini, and Richard Holme. Reconstructing the Holocene geomagnetic field. *Earth and Planetary Science Letters*, 312(3-4):497–505, dec 2011. doi: 10.1016/j.epsl.2011.10.031. URL `https://doi.org/10.1016/j.epsl.2011.10.031`.

W Kuang, Andrew Tangborn, Weiyuan Jiang, Don Liu, Zicai Sun, Jeremy Bloxham, and Zigang Wei. Mosst-das: The first generation geomagnetic data assimilation framework. *Communications in Computational Physics*, 3:85–108, 01 2008.

Carlo Laj, Catherine Kissel, Vincent Scao, Juerg Beer, Donald M. Thomas, Hervé Guillou, Raimund Muscheler, and Gerhard Wagner. Geomagnetic intensity and inclination variations at Hawaii for the past 98kyr from core SOH-4 (Big Island): a new study and a comparison with existing contemporary data. *Physics of the Earth and Planetary Interiors*, 129(3-4): 205–243, feb 2002. doi: 10.1016/s0031-9201(01)00291-6. URL `https://doi.org/10.1016/s0031-9201(01)00291-6`.

Peter Olson and Hagay Amit. Changes in earth's dipole. *Naturwissenschaften*, 93(11): 519–542, aug 2006. doi: 10.1007/s00114-006-0138-6. URL `https://doi.org/10.1007/s00114-006-0138-6`.

Peter Olson and Hagay Amit. Mantle superplumes induce geomagnetic superchrons. *Frontiers in Earth Science*, 3, jul 2015. doi: 10.3389/feart.2015.00038. URL `https://doi.org/10.3389/feart.2015.00038`.

S. Panovska, M. Korte, C. C. Finlay, and C. G. Constable. Limitations in paleomagnetic data and modelling techniques and their impact on Holocene geomagnetic field models. *Geophysical Journal International*, 202(1):402–418, may 2015. doi: 10.1093/gji/ggv137. URL `https://doi.org/10.1093/gji/ggv137`.

F. J. Pavón-Carrasco, E. Tema, M. L. Osete, and R. Lanza. Statistical analysis of palaeomagnetic data from the last four centuries: Evidence of systematic inclination shallowing

in lava flow records. *Pure and Applied Geophysics*, 173(3):839–848, October 2014. doi: 10.1007/s00024-014-0946-0. URL https://doi.org/10.1007/s00024-014-0946-0.

Peter Mauersberger. Das Mittel der Energiedichte des geomagnetischen Hauptfelds an der Erdoberfläche und seine säkulare Änderung. *Gerlands Beitr. Geophys.*, 65:207–215, 1956.

Wilbor Poletti, Andrew J. Biggin, Ricardo I.F. Trindade, Gelvam A. Hartmann, and Filipe Terra-Nova. Continuous millennial decrease of the Earth's magnetic axial dipole. *Physics of the Earth and Planetary Interiors*, 274:72–86, jan 2018. doi: 10.1016/j.pepi.2017.11.005. URL https://doi.org/10.1016/j.pepi.2017.11.005.

R. Egli. VARIFORC: An optimized protocol for calculating non-regular first-order reversal curve (FORC) diagrams. *Global and Planetary Change*, 110:302–320, nov 2013. doi: 10.1016/j.gloplacha.2013.08.003. URL https://doi.org/10.1016/j.gloplacha.2013.08.003.

A. De Santis, E. Qamili, G. Spada, and P. Gasperini. Geomagnetic south atlantic anomaly and global sea level rise: A direct connection? *Journal of Atmospheric and Solar-Terrestrial Physics*, 74:129–135, jan 2012. doi: 10.1016/j.jastp.2011.10.015. URL https://doi.org/10.1016/j.jastp.2011.10.015.

G Schubert. *Treatise on Geophysics*. 01 2007. doi: 10.1016/C2009-1-28330-4.

Ron Shaar and Lisa Tauxe. Thellier GUI: An integrated tool for analyzing paleointensity data from thellier-type experiments. *Geochemistry, Geophysics, Geosystems*, 14(3):677–692, mar 2013. doi: 10.1002/ggge.20062. URL https://doi.org/10.1002/ggge.20062.

Robert S. Sternberg. Secular variation of archaeomagnetic direction in the American Southwest, A.D. 750–1425. *Journal of Geophysical Research*, 94(B1):527, 1989. doi: 10.1029/jb094ib01p00527. URL https://doi.org/10.1029/jb094ib01p00527.

Neil Suttie, Richard Holme, Mimi J. Hill, and John Shaw. Consistent treatment of errors in archaeointensity implies rapid decay of the dipole prior to 1840. *Earth and Planetary Science Letters*, 304(1-2):13–21, apr 2011. doi: 10.1016/j.epsl.2011.02.010. URL https://doi.org/10.1016/j.epsl.2011.02.010.

John A. Tarduno, Michael K. Watkeys, Thomas N. Huffman, Rory D. Cottrell, Eric G. Blackman, Anna Wendt, Cecilia A. Scribner, and Courtney L. Wagner. Antiquity of the south atlantic anomaly and evidence for top-down control on the geodynamo. *Nature Communications*, 6(1), jul 2015. doi: 10.1038/ncomms8865. URL https://doi.org/10.1038/ncomms8865.

Lisa Tauxe and Hubert Staudigel. Strength of the geomagnetic field in the cretaceous normal superchron: New data from submarine basaltic glass of the troodos ophiolite. *Geochemistry, Geophysics, Geosystems*, 5(2), feb 2004. doi: 10.1029/2003gc000635. URL `https://doi.org/10.1029/2003gc000635`.

Nicholas Teanby, Carlo Laj, David Gubbins, and Malcolm Pringle. A detailed palaeointensity and inclination record from drill core SOH1 on Hawaii. *Physics of the Earth and Planetary Interiors*, 131(2):101–140, jul 2002. doi: 10.1016/s0031-9201(02)00032-8. URL `https://doi.org/10.1016/s0031-9201(02)00032-8`.

Thellier and Thellier. Sur l'intensité du champ magnétiqueterrestre dans le passé historique et géologique. *Ann. Geophys.*, 15:285–376, 1959.

E. Thellier. Early research on the intensity of the ancient geomagnetic field. *Physics of the Earth and Planetary Interiors*, 13(4):241–244, jan 1977. doi: 10.1016/0031-9201(77)90106-6. URL `https://doi.org/10.1016/0031-9201(77)90106-6`.

P. C. Torres. Carta geologica da Ilha do Fogo-Erupcoes historicas e formacoes encaixantes. 1997.

A.M. Tulloch. A study of Recent secular variation of the geomagnetic field as recorded by lavas from Mount Vesuvius and the Canary Islands. 1992.

Alexander von Humboldt and Jean-Baptiste Biot. Sur les variations du magnétisme terrestre à différentes latitudes. *Journal de physique, de chimie, d'histoire naturelle et des arts*, pages 429–450, 1804.

Daming Wang and Rob van der Voo. The hysteresis properties of multidomain magnetite and titanomagnetite/titanomaghemite in mid-ocean ridge basalts. *Earth and Planetary Science Letters*, 220(1-2):175–184, mar 2004. doi: 10.1016/s0012-821x(04)00052-4. URL `https://doi.org/10.1016/s0012-821x(04)00052-4`.

Yuhji Yamamoto and Ryo Yamaoka. Paleointensity study on the holocene surface lavas on the island of hawaii using the tsunakawa–shaw method. *Frontiers in Earth Science*, 6, may 2018. doi: 10.3389/feart.2018.00048. URL `https://doi.org/10.3389/feart.2018.00048`.

J.D.A. Zijderveld. The natural remanent magnetizations of the exeter volcanic traps (permian, europe). *Tectonophysics*, 4(2):121–153, apr 1967. doi: 10.1016/0040-1951(67)90048-0. URL `https://doi.org/10.1016/0040-1951(67)90048-0`.